5-2018

The Influence of Biomass Burning Aerosols on Stratocumulus Clouds over the South-East Atlantic

Sampa Das
Purdue University

Recommended Citation

Das, Sampa, "The Influence of Biomass Burning Aerosols on Stratocumulus Clouds over the South-East Atlantic" (2018). *Open Access Dissertations*. 1863.
https://docs.lib.purdue.edu/open_access_dissertations/1863

THE INFLUENCE OF BIOMASS BURNING AEROSOLS ON STRATOCUMULUS CLOUDS OVER THE SOUTH-EAST ATLANTIC

by

Sampa Das

A Dissertation

Submitted to the Faculty of Purdue University
In Partial Fulfillment of the Requirements for the degree of

Doctor of Philosophy

Department of Earth, Atmospheric and Planetary Sciences
West Lafayette, Indiana
May 2018

THE PURDUE UNIVERSITY GRADUATE SCHOOL
STATEMENT OF COMMITTEE APPROVAL

Dr. Harshvardhan, Chair
    Department of Earth, Atmospheric and Planetary Sciences
Dr. Peter Colarco
    Atmospheric Chemistry and Dynamics Laboratory, NASA GSFC
Dr. Yutian Wu
    Lamont-Doherty Earth Observatory, Columbia University
Dr. Mike Baldwin
    Department of Earth, Atmospheric and Planetary Sciences
Dr. Greg Michalski
    Department of Earth, Atmospheric and Planetary Sciences

Approved by:
    Dr. Darryl Granger
        Head of the Graduate Program

To my Dad— the eternal optimist and the first PhD Graduate I have known.

ACKNOWLEDGMENTS

I express my sincere gratitude to my advisor, Prof. Harshvardhan, for his continued support and guidance in pursuing my PhD studies. Be it the initial days of my transitioning from a chemical engineering background to that of atmospheric sciences, or today, when I can finally synthesize my research into a dissertation, his mentoring and immense knowledge in the field has nurtured me to getting further intrigued to this research area. I also thank him for providing me the opportunity to collaborate with the eminent research scientists at NASA GSFC, especially Drs. Mian Chin, Peter Colarco and Huisheng Bian, who deserve a special acknowledgement.

I cannot thank Dr. Colarco enough for helping me in being acquainted with the GEOS-5 model, for providing me computing time on the NCCS cluster to continue my research pursuit and indeed for his patience in replying to my long emails filled with novice modeling questions. In the same vein, I would like to thank my other committee members as well, Professors Yutian Wu, Mike Baldwin and Greg Michalski, for their insightful comments and encouragement, but also for the questions they posed during our meetings that incentivized me to widen my research from various perspectives.

I am thankful to my friends and fellow PhD students here at Purdue for the stimulating discussions, for the sleepless nights we worked together before deadlines, and for all the fun we have had in the past years. Lastly, I would be remiss if I did not acknowledge the unconditional support of my parents and my sister in lending an empathetic ear whenever there was a struggle in my PhD or in life in general, despite being so far away across the globe.

TABLE OF CONTENTS

LIST OF TABLES vii
LIST OF FIGURES viii
ABSTRACT xiii
CHAPTER 1. INTRODUCTION 1
  1.1 Introduction to the Concept of Radiative Forcing 4
  1.2 Aerosol-Radiation and Aerosol-Cloud Interactions 6
  1.3 Aerosol Properties Relevant to REari Estimation 9
  1.4 Introduction to Marine Stratocumulus Clouds 12
  1.5 Thesis Organization 16
CHAPTER 2. MODEL AND OBSERVATIONS 17
  2.1 GEOS-5 Atmospheric General Circulation Model 17
    2.1.1 Biomass Burning Emissions 19
  2.2 CALIOP Lidar Observations 20
    2.2.1 Inherent Limitations and Algorithm Biases 22
CHAPTER 3. AEROSOL TRANSPORT AND VERTICAL DISTRIBUTION 24
  3.1 Background, Motivation and Objectives 24
  3.2 Approach and Methods 27
    3.2.1 Experimental Setup for GEOS-5 27
    3.2.2 CALIOP Data Processing 29
  3.3 Results and Discussion 30
    3.3.1 Horizontal Distribution of Smoke and Clouds 30
    3.3.2 Contrast Over Land and Ocean 34
      3.3.2.1 Sampling along CALIPSO Tracks 34
      3.3.2.2 Mean Extinction Profiles 38
CHAPTER 4. MULTI-MODEL EVALUATION OF AEROSOL TRANSPORT 41
  4.1 AeroCom Models 41
  4.2 Results and Discussion 45
    4.2.1 Aerosol Plume Transport 45
    4.2.2 CALIOP Measurement Biases 55

CHAPTER 5. TRANSPORT PROCESSES AFFECTING AEROSOL VERTICAL DISTRIBUTION ……………………………………………………………………………57
5.1 Aerosol Removal 59
5.2 Convective Transport 60
5.3 Other factors 63
CHAPTER 6. MODEL SENSITIVITY TO AEROSOL VERTICAL DISTRIBUTION 65
6.1 Introduction 65
6.2 Approach and Methods 67
6.2.1 CALIOP Data Processing 67
6.2.2 Aerosol Redistribution Methodology 70
6.2.3 Model Configuration and Experimental Setup 72
6.3 Results and Discussions 76
6.3.1 Model Cloud Responses to Changes in Aerosol Vertical Distribution 76
6.3.2 Explaining the Changes in Cloud Properties 79
6.3.3 Direct and Semi-Direct Effects of Aerosol on Radiative Forcing 88
CHAPTER 7. SUMMARY AND CONCLUSIONS 91
7.1 Aerosol Plume Transport Evaluation 91
7.2 Sensitivity to Aerosol Vertical Distribution 93
REFERENCES 95

LIST OF TABLES

Table 3.1 Mean smoke AOD from GEOS-5 model, CALIOP and a previous study. 33

Table 4.1 Models used in this study and general information about their configuration 43

Table 4.2 Mean aerosol optical depth between 2-4 km above sea level (AOD_{2-4}) from models and CALIOP averaged over three 10-degree longitude-by-latitude boxes in the direction of aerosol plume transport for each sub-region. 54

Table 6.1 Design of the Numerical Experiments 73

LIST OF FIGURES

Figure 1.1 Fire pixel counts retrieved from MODIS satellite instrument depicting the biomass burning (BB) areas over southern Africa. The fire counts are averaged for the peak BB months of August and September of 2008. 2

Figure 1.2 September mean climatology (2002-2012) of finemode aerosol optical depth and low-level cloud fraction from MODIS satellite instrument in colored and line contours respectively. 600-hPa wind vectors from ERA-Interim renanalysis dataset are overlayed to show the direction of wind transport. The inset, a 6°S–17°S latitude slice based on CALIOP Lidar data, highlights the subsiding aerosol layer and deepening cloudy boundary layer farther offshore, thus allowing opportunities for aerosol-cloud interactions. This figure is taken from Zuidema et al. (2016). 3

Figure 1.3 An illustration comparing (a) instantaneous RF, (b) RF, which allows stratospheric temperature to adjust, (c) flux change when the surface temperature is fixed over the whole Earth (a method of calculating ERF), (d) the ERF calculated allowing atmospheric and land temperature to adjust while ocean conditions are fixed and (e) the equilibrium response to the climate forcing agents. ΔT_o represents the land temperature response, while ΔT_s is the full surface temperature response . This figure is adapted from Chapter 8 of IPCC AR5, Myhre et al. (2013).................................6

Figure 1.4 Various ways in which aerosols affect radiation and clouds. These are depicted in the light of old and new terminologies followed in IPCC reports. The blue arrows depict solar radiation, the grey arrows terrestrial radiation and the brown arrow symbolizes the importance of couplings between the surface and the cloud layer for rapid adjustments. This figure is adapted from Boucher et al. (2013)................................7

Figure 1.5 Multiple semi-direct effects of absorbing aerosols (AA) on clouds based on Koch and Del Genio (2010). Red and blue color signifies positive and negative response to the aerosol radiative effects due to aerosol-radiation interactions. 9

Figure 1.6 Schematic showing key processes occurring in the stratocumulus-topped boundary layer, adapted from Wood (2012)...13

Figure 1.7 Ideal (dotted line) and measured (solid line) vertical profiles of vapor (q) and liquid water (q_l) mixing ratios, equivalent potential temperature (θ_e) and dry air temperature

(T) for a summertime shallow and quite well-mixed STBL over the North Sea. The figure is adapted from Nicholls (1984). 15

Figure 2.1 Input emissions of BC and OC (× 10^{-9} kg m^{-2} s^{-1}) from (a) QFED2 and (b) GFED3 biomass burning inventory averaged over August and September 2008. 19

Figure 3.1 The region of interest is divided into sub-regions A (30°-20°S, 35°E-15°W), B (20°-10°S, 35°E-15°W) and C (10°S-0°, 35°E-15°W) to distinguish between the different aerosol transport features within the domain...25

Figure 3.2 (a) Horizontal distribution of BB AOD (colored contours) from CALIOP gridded product (described in 3.2) and low-level cloud fractions (blue line contours) from MODIS Level 3 monthly global product (MOD08_M3) for August-September 2008, and (b) corresponding results from GEOS-5 simulations using QFED2 BB emissions. 32

Figure 3.3 Vertical distribution of smoke aerosol extinctions (km^{-1}) along (a) three distinct CALIPSO satellite tracks retrieved from (b) CALIOP at 532 nm and those simulated by GEOS5-GOCART at 550 nm (c) using GFED3 BB emissions and (d) using QFED2 BB emissions. CALIOP retrieved cloud top heights are depicted using black lines on both CALIOP and GEOS-5 panels for tracks over the ocean. CALIOP observed surface elevation is plotted (in purple) on CALIOP panel for the track over land. White region on CALIOP panels represents no detectable signals of smoke aerosol. 37

Figure 3.4 Comparisons of mean (Aug-Sep) smoke extinction profiles (km^{-1}) from CALIOP (in red) and GEOS5-GOCART (in green) over land (13°-35°E) and oceanic (13°E-15°W) parts of the three sub-regions, viz. A (30°-20°S), B (20°-10°S) and C (10°S-0°) of the domain. CALIOP-retrieved cloud extinction profiles (in blue) are plotted using the upper x-axis for profiles over the ocean to show relative altitudes of smoke and cloud layers. The mean surface elevations retrieved from CALIOP are shown using dashed lines for profiles over land...39

Figure 4.1 Meridional average of smoke aerosol extinction coefficients (km-1) over sub-region A (30°-20°S, 35°E-15°W) from CALIOP, GEOS5-GOCART and four AeroCom models (GEOS-CHEM, CAM5, ECHAM6-SALSA, HadGEM3). CALIOP-retrieved mean cloud top heights are overlaid (in blue solid line) on all the panels for the oceanic parts of the domain. The black solid line on the CALIOP panel depicts the mean surface elevation measured by the lidar signal. Note that all models used the GFED3 BB emission inventory and model averages are for Aug-Sep 2008, while CALIOP averages are for Aug-Sep 2007-2009..46

Figure 4.2 Same as Figure 4.1 but over sub-region B (20°-10°S, 35°E-15°W)..........................47

Figure 4.3 Same as Figure 4.1 but over sub-region C (10°S-0°, 35°E-15°W)............................50

Figure 4.4 Horizontal wind streamlines over the domain at significant pressure levels, retrieved from MERRA reanalysis data and averaged over Aug-Sep 2008. The streamlines are colored by the wind speeds in m/s. 52

Figure 4.5 Vertical pressure velocities (hPa/day) during Aug-Sep 2008 from MERRA (left) and ERA-Interim (right) reanalysis data over the three sub-regions of the domain. Warmer colors signify downward motion while cooler colors signify upward motion..........53

Figure 4.6 Comparison of CALIOP classified (left) smoke and (right) smoke plus polluted dust aerosol extinction coefficients (km^{-1}) at 1064 nm over sub-regions (a) B (20°S-10°S, 35°E-15°W) and (b) C (10°S-0°, 35°E-15°W). CALIOP retrieved mean cloud top heights are superimposed in white over the ocean...55

Figure 5.1 Meridional mean MERRAero smoke (BC+OC) aerosol mass concentrations ($\times 10^{-8}$ kg m^{-3}) averaged over Aug-Sep 2008 for the three sub-regions of the domain. CALIOP-retrieved mean cloud top heights are superimposed in blue over the ocean. 58

Figure 5.2 Contours of mean (left) smoke aerosol mass concentrations ($\times 10^{-8}$ kg m^{-3}) and (right) carbon monoxide (CO) mixing ratios (ppmv) simulated by GEOS5-GOCART during Aug-Sep 2008 over the three sub-regions of the domain. CALIOP-retrieved cloud top heights are overlaid (in blue solid line) on all the sub-plots...................................60

Figure 5.3 Comparison of convective mass flux (CMF, g m^{-2} s^{-1}) simulations by (left) GEOS-5 and (right) CAM5 during Aug-Sep 2008 over the three sub-regions of the domain. Note that the values are plotted on a log colorscale to account for the large difference in magnitudes of the simulated fluxes between the two models. 62

Figure 5.4 (Top) Vertical pressure velocities simulated by GEOS-5 over sub-region B, when run in a free-running GCM (left) and in the replay mode using MERRA Reanalysis data (right). The corresponding aerosol extinction contours for each of the runs are depicted in the bottom panels. Blue solid lines on the bottom panels represent the CALIOP retrieved cloud-top heights. 64

Figure 6.1 Aerosol climatology based on (left) CALIOP 532 nm retrievals of smoke aerosol, which in this study is combination of ‘elevated smoke’, ‘polluted dust’ and ‘polluted continental’ aerosol types. (Right) Aerosol climatology based on MERRAero. Top panels compare the horizontal distribution of smoke AOD, where the blue box depicts the extent of the domain chosen for aerosol redistribution. Bottom panels compare the vertical distribution of smoke aerosol from CALIOP and MERRAero using meridional cross-sections of aerosol extinctions averaged over the domain of interest (blue box)..69

Figure 6.2. Demonstration of the redistribution methodology for one sample model grid and for total and individual smoke aerosol species mass in the model................................72

Figure 6.3. Application of the redistribution method and design of the experiments. Meridional cross-sections of smoke aerosol (BC, OC, and SO4) mass in GEOS-5 averaged over the latitudes of interest (0-20S) for (a) default/MERRAero climatology (CTL), (b) after redistribution in vertical according to CALIOP (RED) and removing smoke aerosols over the ocean (NOA)..75

Figure 6.4. (Top-Left) Ensemble mean cloud area fraction for control (CTL) case. (Top-Right) Mean cloud area fraction retrieved from MODIS and averaged over August and September of 2008. (Bottom-Left) Changes in cloud fractions between Redistributed (RED) and control (CTL) simulations. (Bottom-Right) Changes in cloud fractions between Redistributed (RED) and no smoke aerosol (NOA) simulations. The black box in the bottom panels shows the domain over which aerosol aerosols were vertically redistributed. Black stippling on bottom panels indicates the significant (95% confidence) changes following the t-test..77

Figure 6.5 Changes in (a) in-cloud optical depth representative of cloud liquid water path and (b) MBL heights in between the experiments...78

Figure 6.6 (a) All-sky long wave (LW) and short wave (SW) heating rates and (b) vertical pressure velocities are averaged over the areas (12E-5W, 0-20S) that show most differences between the cloud amounts in RED and NOA case. This area also corresponds to the cloud increase region for RED compared to CTL. 80

Figure 6.7 (a) Liquid -water Potential temperature and (b) dry-air temperatures profiles averaged over the cloud-increase region for RED, CTL and NOA cases...............................82

Figure 6.8 Relating temperature and humidity profile changes to cloud fraction and liquid condensate amounts within the clouds. (a) Dry-air temperature, (b) Specific humidity, (c) cloud fractions and (d) liquid condensate amounts are averaged over the cloud-increase region. 84

Figure 6.9 Ensemble mean boundary layer and cloud properties for the cloud-decrease region.. 86

Figure 6.10 (Top) Changes in vertical pressure velocities over cloud-decrease region. (Bottom) Cloud-top heights from the three experiments are overlaid (dotted lines) on the aerosol mass concentration contours for the RED case. The model output of cloud-top pressures in infrared channel (540-980 cm^{-1}) were converted to geopotential heights to obtain the cloud-tops.. 87

Figure 6.11 Changes in instantaneous RF due to smoke aerosols calculated at (a) the TOA and (b) the surface for all-sky conditions and combining both SW and LW. 89

ABSTRACT

Author: Das, Sampa. PhD
Institution: Purdue University
Degree Received: May 2018
Title: The Influence of Biomass Burning Aerosols on Stratocumulus Clouds over the South-East Atlantic
Major Professor: Harshvardhan Harshvardhan

Optically thick smoke aerosol plumes originating from biomass burning (BB) in the southwestern African Savanna during the austral spring are transported westward by the free-tropospheric winds to primarily overlie the vast stretches of stratocumulus cloud decks in the South-East Atlantic. We evaluated the simulations of long-range transport of BB aerosol by the Goddard Earth Observing System (GEOS-5) and four other global aerosol models using Cloud-Aerosol Lidar with Orthogonal Polarization (CALIOP) observations over the complete South African-Atlantic region. Models in general captured the vertical distribution of aerosol over land but exhibited some common features after long-range transport of smoke plumes that were distinct from that of CALIOP. Most importantly, the model simulated BB aerosol plumes quickly descend to lower levels just off the western coast of the continent, while CALIOP data suggests that smoke plumes continue their horizontal transport at elevated levels above the marine boundary layer. The levels to which the aerosol plumes are subsided, and the steepness of their descent vary amongst the models as well as amongst the different sub-regions of the domain. Investigations into possible causes of differences between GEOS-5 and CALIOP aerosol transport over the ocean revealed a minimal role of aerosol removal processes in the model as opposed to model dynamics.

It has been well established that the cloud adjustments to aerosol-radiation interactions are strongly dependent on the relative location of the aerosol layer with respect to the clouds. Consequently, we evaluated the GEOS-5 sensitivity to changes in aerosol vertical distribution by constraining the model smoke aerosol vertical profiles using CALIOP observations. A climatology of CALIOP retrievals of smoke aerosol extinction profiles were obtained using ten years of data (2006-15). An aerosol redistribution methodology was then developed to vertically adjust the smoke aerosol mass in the model to resemble the CALIOP extinction profile, such that the column aerosol mass is conserved. Three sets of experiments, each containing five ensemble members were designed for GEOS-5 AGCM in free-running mode by prescribing aerosols at each model time-step using an aerosol climatology i.e. MERRAero (2003-14). First is the control case (CTL), where aerosol vertical distributions were based on the default MERRAero climatology. Second set used the redistributed aerosol climatology (RED) and for the third set, smoke aerosols were simply removed from the oceanic parts of the domain (NOA). There was an increase in cloud fraction by about 40% for RED compared to NOA at areas of high aerosol loading near the coast. Between RED and CTL, there was an increase in cloud fraction near the coast by ~35% with respect to RED and a decrease in cloud fractions by ~25% for areas away from the coast and warmer sea-surface temperatures. Overall, the absolute magnitudes of changes in cloud fractions are small, but the percentage changes are large because the model simulated cloud fractions for the CTL case are much smaller and spatially displaced compared to the cloud fractions retrieved from MODIS to begin with. Probable mechanisms for the observed changes in cloud amounts and MBL properties were investigated. Aerosol effects on TOA all-sky radiative forcing showed close resemblance to the pattern for cloud fraction change, wherein increase in cloud cover led to enhanced cooling and vice versa. Aerosol impacts on surface radiative forcing however, suggested a strong cooling of the ocean surface irrespective of where the aerosol layer is placed in the atmosphere.

CHAPTER 1. INTRODUCTION

The Sun's energy is the driving force for Earth's climate, but not all the energy that reaches the top of the Earth's atmosphere finds its way to the surface. Atmospheric aerosols, either naturally occurring or produced due to anthropogenic activities, scatter and absorb the incoming solar radiation to varying degrees depending on their physical properties. This scattering and absorption of radiation contributes to the "direct effects" of aerosols on Earth's climate [*Ramanathan et al.,* 2001]. Clouds are an important component of the Earth's radiation budget and aerosols can further affect Earth's climate by modifying the cloud properties. Aerosols interact with clouds as cloud condensation nuclei/ice nuclei to affect their microphysics, leading to the changes in cloud reflectivity and lifetime [*Charlson et al.,* 1992; *Chen et al.,* 2010]. These are called the "indirect effects" of aerosols. Furthermore, when the aerosols are significantly absorbing in nature, they perturb the temperature gradient of the atmosphere owing to their direct effects and therefore affect the atmospheric motions and cloud distributions. Absorbing aerosols suspended near clouds were initially thought to contribute to cloud evaporation, originally termed the "semi-direct effect" [*Hansen et al.,* 1997], but numerous studies over the past two decades have described additional mechanisms by which cloud cover or liquid water path (LWP) may increase or decrease depending on the relative location of the aerosol layer with respect to clouds [*Johnson et al.,* 2004; *Koch and Del Genio* 2010]. Thus, there can be multiple semi-direct effects when absorbing aerosols and clouds are simultaneously present.

Strongly absorbing aerosol species include black carbon (BC) and mineral dust, of which BC has been recognized as the second most important human emission responsible for climate change with an estimated global climate forcing potential of about 1.1 W m^{-2}, second only to that of carbon dioxide [*Bond et al.,* 2013]. Emission sources of BC include open biomass burning (BB) and combustion of fossil and bio-diesel fuels, of which BB being the larger contributor to the global BC budget [*Saleh et al.,* 2014]. Although BB occurs globally, there are different features associated with different types of vegetation and climate regimes. BC amounts are found to be particularly large during efficient flaming fires, common in the savanna and cerrado grassland of Africa and South America [*Hao et al.*, 1996]. BB aerosols originating from the seasonal burning (July-October) of agricultural residue and grasslands in the southwestern African Savanna (Fig 1.1) traverse large distances westward to primarily overlie the vast stretches of marine stratocumulus clouds residing over south-east (SE) Atlantic [Fig 1.2; *Zudeima et al.,* 2016].

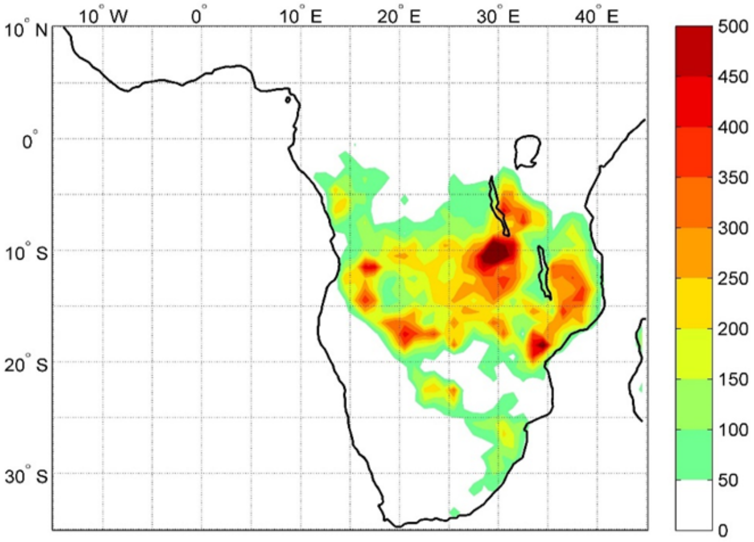

Figure 1.1 Fire pixel counts retrieved from MODIS satellite instrument depicting the biomass burning (BB) areas over southern Africa. The fire counts are averaged for the peak BB months of August and September of 2008.

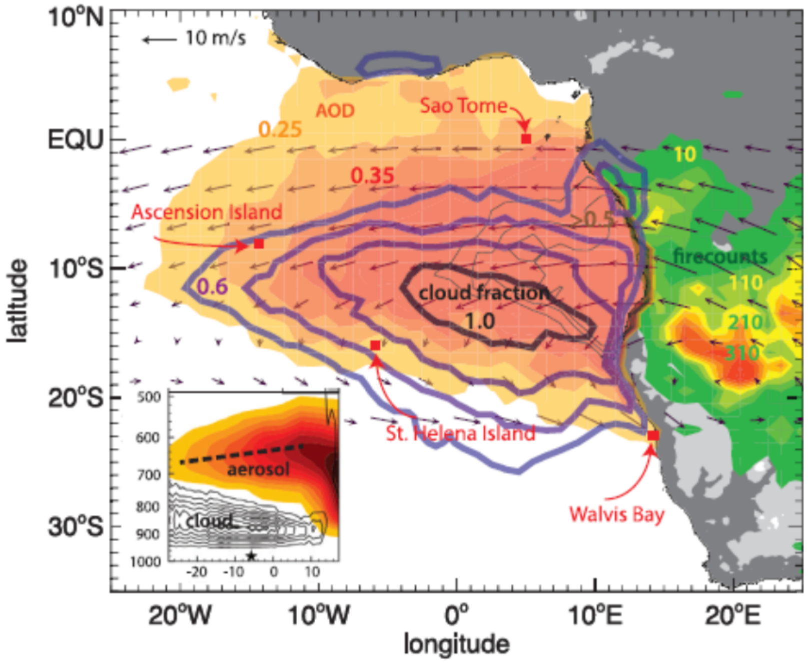

Figure 1.2 September mean climatology (2002-2012) of finemode aerosol optical depth and low-level cloud fraction from MODIS satellite instrument in colored and line contours respectively. 600-hPa wind vectors from ERA-Interim renanalysis dataset are overlayed to show the direction of wind transport. The inset, a 6°S–17°S latitude slice based on CALIOP Lidar data, highlights the subsiding aerosol layer and deepening cloudy boundary layer farther offshore, thus allowing opportunities for aerosol-cloud interactions. This figure is taken from Zuidema et al. (2016).

During its course of transport, the dense BB aerosol layer interacts directly with the incoming solar radiation and more importantly with the underlying clouds to affect the regional radiation budget via all the different ways outlined above (semi-direct and indirect effects). Therefore, SE Atlantic provides for an ideal test-bed to improve our understanding of aerosol-cloud-radiation interactions that have been recognized as the largest source of uncertainty in estimation of Earth's changing energy budget using global climate models [*Boucher et al.,* 2013]. Ironically, some of the largest inter-model differences have also persisted in the estimation of aerosol radiative effects over this region compared to the other parts of the globe [*Schulz et al.* 2006; *Stier et al.,* 2013]. This region has thus drawn attention of several national and international research agencies to schedule their field measurement campaigns (NASA's ORACLES, DOE's LASIC or UK's CLARIFY), which have either begun or are soon upcoming, see Zudeima et al. (2016) for more details. Towards this end, our study focuses on improving our understanding of the BB aerosol transport representation in global models. In addition, what processes affect this transport, and eventually, how do the model estimates of aerosol effects on clouds and regional energy balance change if modeled aerosol distributions are constrained using retrievals of aerosol properties from satellites instruments in space. Before delving into further details of our efforts in addressing these issues, this chapter summarizes some key concepts on aerosols, clouds, radiation and their combined interactions that will be relevant in understanding the outcomes of this study.

1.1 Introduction to the Concept of Radiative Forcing

The temperature of the Earth's atmosphere is determined by the balance between incoming shortwave (SW) radiation from the sun and outgoing longwave (LW) radiation from the Earth's surface. Radiative Forcing (RF) is a measure of the influence that an external agent such as greenhouse gases (GHGs) or aerosols can have on this energy balance. This perturbation to the energy budget contributes to the Earth's changing climate, which is why RF is also termed as climate forcing in some review studies [e.g. *Yu et al.,* 2006]. IPCC (Inter-governmental Panel for Climate Change) third-assessment report defined RF as 'the change in net (down minus up) irradiance (solar plus longwave; in W m^{-2}) at the tropopause after allowing for stratospheric temperatures to readjust to radiative equilibrium, but with surface and tropospheric temperatures and state held fixed at the unperturbed values' [*Ramaswamy et al.,* 2001]. Positive RF signifies an increase in the amount of energy retained within the Earth's surface-atmosphere system, leading to its warming. The negative RF by the same logic therefore, leads to cooling of the Earth system. This RF concept assumes that the surface-troposphere is one coupled system such that the changes in surface temperature is independent of the altitude at which the changes in radiative energy takes place. This assumption holds well for most of the forcing agents that are well-mixed within the atmosphere, such as GHGs, but not for aerosols whose concentrations are highly variable in space and time and their perturbation to the radiative fluxes might be widely different at top of the atmosphere (TOA) than at the surface [*Ramanathan et al.* 2001]. Thus, changes in radiation budget due to aerosols both at TOA and at the surface should be accounted for to better understand their effects on Earth's climate.

Furthering the quest for a better understanding and an indicator that is more inclusive of the various ways in which various forcing agents modify Earth's radiative balance, most recent assessment report of IPCC (AR5, 2013) introduced the concept of effective radiative forcing (ERF) apart from the original RF concept followed in their previous assessments. The major distinction between the two concepts is that while in the RF concept all surface and tropospheric conditions are kept fixed, the ERF calculations in AR5 allow all physical variables such as atmosphere temperatures, water vapor and clouds to respond to the perturbations caused by the forcing agents, except for the variables concerning the ocean and sea ice. ERF and RF values are significantly different for anthropogenic aerosols mostly owing to their influence on clouds via the indirect and semi-direct effects. Since these aerosol-induced changes to clouds do not operate through changes in global mean surface temperature, which are slowed by the massive heat capacity of the oceans, these are termed 'rapid adjustments'. Rapid adjustments occur at a much faster time scale compared to the ocean responses to forcing, usually within a few weeks. The inclusion of these adjustments, thus makes ERF a better indicator of the eventual temperature response of the Earth's climate than RF alone [*Myhre et al.* 2013]. Apart from these two definitions, several studies over the years have developed and used alternate definitions of RF, each with its own advantages and limitations. These are summarized in Chapter 8 of IPCC AR5 and presented here in Figure 1.3

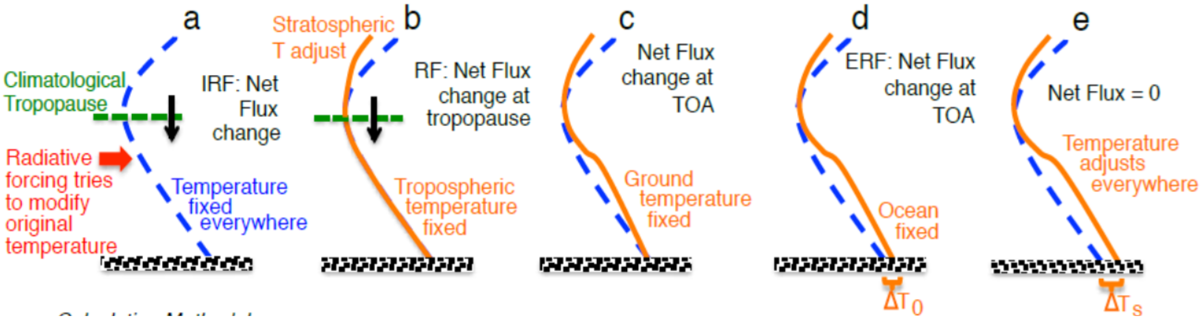

Figure 1.3 An illustration comparing (a) instantaneous RF, (b) RF, which allows stratospheric temperature to adjust, (c) flux change when the surface temperature is fixed over the whole Earth (a method of calculating ERF), (d) the ERF calculated allowing atmospheric and land temperature to adjust while ocean conditions are fixed and (e) the equilibrium response to the climate forcing agents. ΔT_o represents the land temperature response, while ΔT_s is the full surface temperature response . This figure is adapted from Chapter 8 of IPCC AR5, Myhre et al. (2013).

1.2 Aerosol-Radiation and Aerosol-Cloud Interactions

Since the original RF concept got de-emphasized in the favor of ERF in IPCC AR5 following the emerging consensus in recent literature on this topic, aerosol direct, semi-direct and indirect effects can now be perceived in slightly changed ways rather changed terminologies. Aerosol semi-direct effects can be considered as rapid adjustments to the direct effects of aerosol and the RF associated with them together is termed RF from aerosol-radiation interactions (RFari). This RF can now clearly be contrasted with RF from aerosol-cloud interactions (RFaci) that accounts for the aerosol indirect-effects and the adjustments associated with them. This concept is further illustrated in Figure 1.4 based on Chapter 7 of IPCC AR5 [*Boucher et al.,* 2013]. Since the eventual focus of our study will be RFari, this sub-section discusses more on the current state of understanding of aerosol-radiation interactions than the aerosol-cloud interactions.

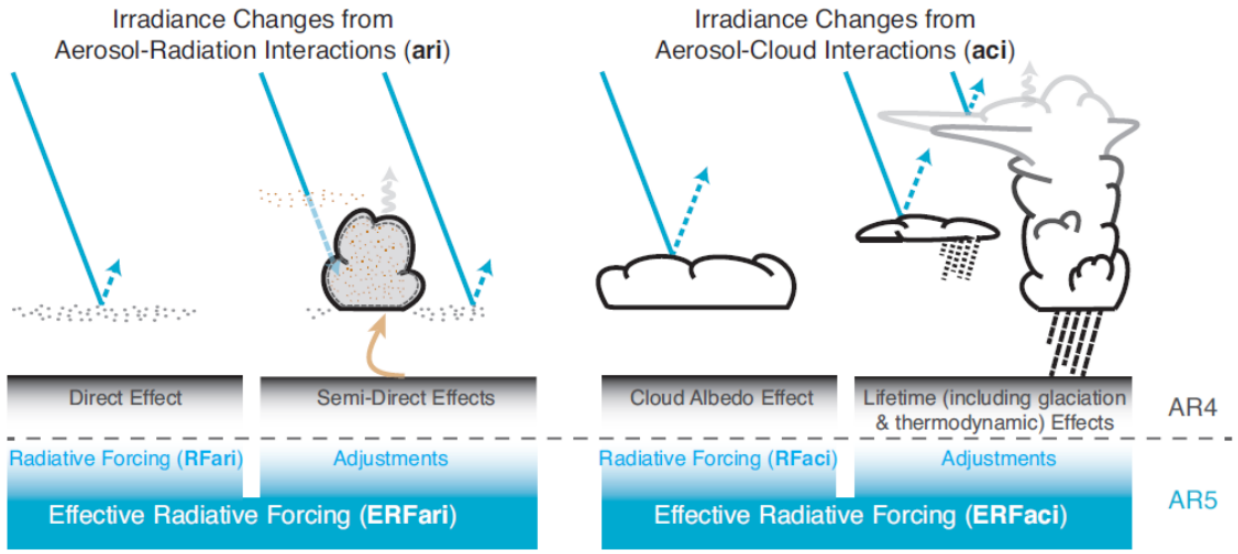

Figure 1.4 Various ways in which aerosols affect radiation and clouds. These are depicted in the light of old and new terminologies followed in IPCC reports. The blue arrows depict solar radiation, the grey arrows terrestrial radiation and the brown arrow symbolizes the importance of couplings between the surface and the cloud layer for rapid adjustments. This figure is adapted from Boucher et al. (2013).

In the solar spectrum and under cloud-free conditions, the radiative effect due to aerosol-radiation interactions (REari), also known as the aerosol direct effect, is negative (radiative cooling) at the TOA owing to the dominance of scattering properties of aerosol mixture on a global scale. Purely scattering aerosol species include sulfate and sea-salt. Observation-based estimates of SW REari at the TOA averaged over cloud-free oceans ranged from -4 to -6 W m^{-2} on a global scale, with regionally averaged REari values often exceeding tens of W m^{-2} [*Yu et al.,* 2006]. On a regional scale, therefore, negative REari at the TOA can weaken and even change to being positive (radiative warming) with increasing amounts of strongly absorbing aerosol species, such as BC and mineral dust, within the aerosol mixture [*Ramanathan and Carmichael*, 2008].

Under cloudy condition, magnitude of REari is usually weaker unless the cloud layer is thin or the bulk of the aerosol mixture resides above the cloud layer [e.g. Chand et al., 2009; Zhang et al., 2016]. Further, reflectivity of the underlying surface is a major determinant of the sign of REari at the TOA in tandem with the optical properties of the aerosol mixture [Chýlek and Coakley, 1974]. The REari at the surface is strictly negative irrespective of the scattering or absorbing properties of aerosol mixture. In fact, REari can be much stronger than that at the TOA, especially over regions where aerosols are mainly absorbing [*Li et al.,* 2010]. Tropospheric aerosols do not interact much in the LW spectrum, except for the coarse-mode aerosol species, such as sea spray and mineral dust, which generally exert a positive REari at the TOA [*Reddy et al.,* 2005].

Rapid adjustment to aerosol-radiation interactions cause the energy distribution within the atmospheric column, including the surface, to change. So, if clouds are simultaneously present in this column, their distribution and properties will change too owing to the changes in atmospheric motions caused by the temperature changes. These adjustments are most pronounced when strongly absorbing aerosol species, such as BC are present in significant amounts. Various mechanisms through which these cloud changes, also known as the aerosol semi-direct effects, can act depends on the cloud types and more importantly on the relative placement of the aerosol layer with respect to clouds. Koch and Del Genio (2010) have nicely summarized and provided a tentative framework based on the major findings from the studies on this topic. This framework is depicted here in Figure 1.5 as well. The detailed discussion on the individual mechanisms and the different plausible scenarios of aerosol and cloud presence is a topic for another time. The mechanism associated with absorbing aerosol layer above stratocumulus clouds that is relevant to our study is further discussed in Chapter 4 of this thesis.

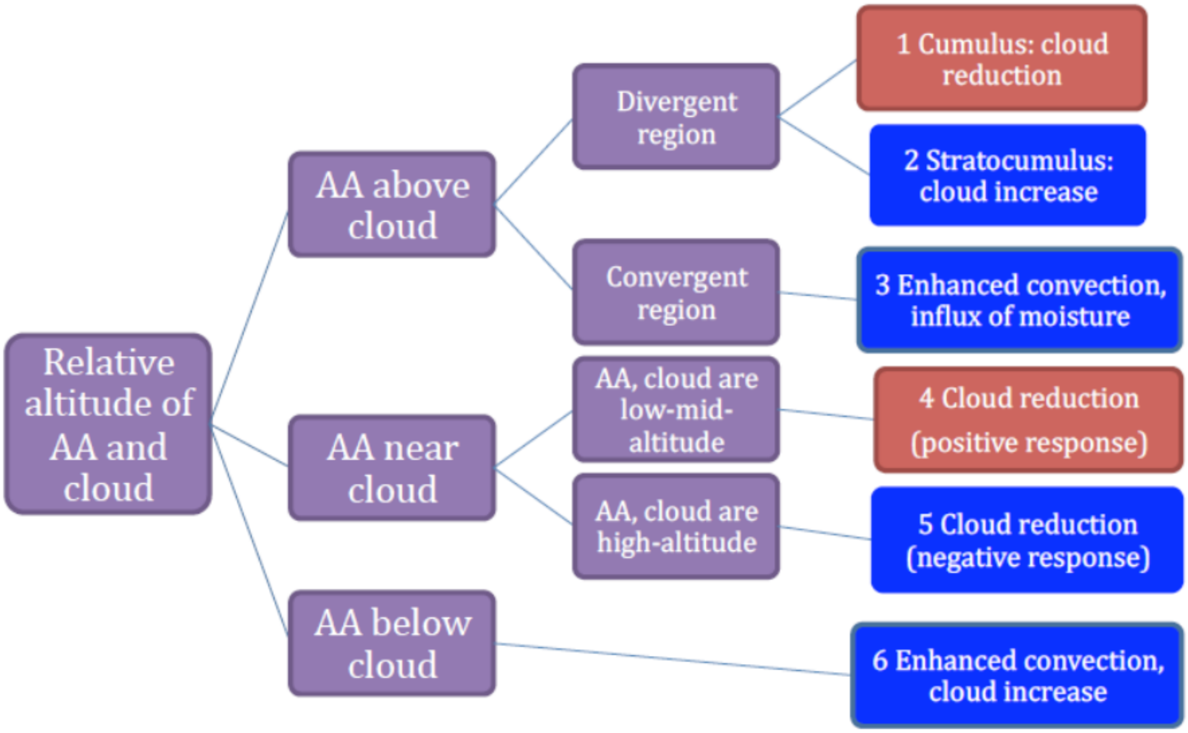

Figure 1.5 Multiple semi-direct effects of absorbing aerosols (AA) on clouds based on Koch and Del Genio (2010). Red and blue color signifies positive and negative response to the aerosol radiative effects due to aerosol-radiation interactions.

1.3 Aerosol Properties Relevant to REari Estimation

Extending from our previous discussion on estimations of REari using global climate models, a knowledge of a set of four quantities as a function of wavelength (λ) are required to first convert the aerosol mass into aerosol optical depths (AOD), and then into a radiative perturbation. These four quantities include the specific extinction co-efficient (κ_{ext}), its functional dependence on relative humidity *f*(RH), the single-scattering albedo (ω_o), and the asymmetry parameter (g_{asym}).

The aerosol properties amongst these are determined by the aerosol composition and size distribution at the most fundamental level.

κ_{ext} is the extinction cross-sectional area per unit mass ($m^2\,g^{-1}$) that depends on the particle size distribution, relative humidity through *f*(RH) and complex refractive index, which itself depends on the chemical composition of the aerosol mixture. Smaller particles have a larger cross-sectional area per unit mass, but the extinction efficiency rapidly increases with particle size until they become comparable to the size of the wavelength. [*Haywood and Shine*, 1995]. Therefore, the column aerosol optical depth (τ_a) is obtained by integrating the specific extinction coefficient and aerosol mass mixing ratio (q_a) over the entire atmospheric column. This determines the overall magnitude of aerosol direct effects on RF at the TOA, atmospheric heating rate and the change in the net flux at the surface. If z is the column height and ρ is the air density, τ_a is given by

$$\tau_a(z) = \int_0^z \rho \kappa_{ext} q_a \, dz \tag{1.1}$$

Single-scattering albedo (ω_o) is defined as the fraction of total extinction that is due to scattering of particles and is given by

$$\omega_o = \frac{\kappa_{sca}}{\kappa_{sca} + \kappa_{abs}} = \frac{\kappa_{sca}}{\kappa_{ext}} \tag{1.2}$$

Here, κ_{sca} and κ_{abs} are specific scattering and absorption coefficients respectively. Thus, ω_o is 1 for a purely scattering particle, while it would be 0 for a pure absorber. The departure of ω_o from 1, also known as the co-albedo ($1- \omega_o$), is a measure of the relative contribution of absorption in the aerosol mixture and hence is a key parameter in determining the sign of REari at the TOA and the heating rate in the atmosphere. Typical values of tropospheric aerosol mixture range between 0.80 and 1.0 at visible wavelengths [*Heintzenberg et al.,* 1997].

Phase function (*P*) is a measure of the intensity of radiation scattered in each direction by an aerosol particle. Most radiation schemes used in global models use the two-stream approximation in their radiation modules, which assumes that radiation travels either up or down. Thus, the directionality of scattering by particles can be simply represented using the asymmetry parameter (g_{asym}), which is calculated by integrating the phase function (*P*) over the forward and backward directions and is given by

$$g_{asym} = \frac{fwd-bck}{fwd+bck} \tag{1.3}$$

Here, *fwd* and *bck* represent the fraction of the radiation scattered in forward and backward direction relative to the incident radiation. These can be calculated by integrating *P*, the phase function, over the forward (backward) hemispheres as follows:

$$fwd = \int_0^{\pi/2} P(\theta)\cos(\theta)\,d\theta \tag{1.4}$$

$$bck = \int_{\pi/2}^{\pi} P(\theta)\cos(\theta)\,d\theta \tag{1.5}$$

Here, θ is the angle between incident radiation and scattering direction. The asymmetry parameter is important in determining the fraction of the radiation that is radiated to space by the aerosol mixture and hence in estimating REari as well. Sulphate aerosols that are predominantly scattering in nature have g_{asym} values ranging between 0.6 and 0.8. Another important property related to the dependence of τ_a on wavelength is Ångström exponent (α), which is often used as a measure of the particle size distribution of the aerosol mixture.

$$\frac{\tau_{\lambda_1}}{\tau_{\lambda_2}} = \left(\frac{\lambda_1}{\lambda_2}\right)^{-\alpha} \tag{1.6}$$

Here, τ_λ is the aerosol optical thickness (AOD) at a given wavelength (λ). Since α is inversely proportional to particle size, smaller particles like BC and sulphate aerosols have larger α values compared to other aerosol species. Overall, α for tropospheric aerosol mixtures varies between 1 and 2 in the 440-675 nm wavelength range [*Eck et al.,* 1999]. Finally, atmospheric heating rate (H) for the two-stream approximation in the radiation modules is given as follows.

$$H = -\frac{1}{\rho c_p}\frac{dF}{dz} \tag{1.7}$$

Here, F is the net (down minus up) radiative flux and c_p is the specific heat capacity of air at constant pressure i.e. 1004 J kg^{-1} K^{-1}.

1.4 Introduction to Marine Stratocumulus Clouds

Stratocumulus (Sc) clouds usually form under the conditions of large-scale subsidence and statically stable lower-troposphere [Klein and Hartmann 1993]. Cold parts of tropical and subtropical oceans provide for such conditions and thus are home to most of the Sc clouds observed over the Earth's surface [Warren et al., 1988]. Cloud formation begins when wind over the ocean surface mixes moist air upwards. As this air moves up, it expands and cools. The cooling causes the relative humidity (RH) to increase and once the RH reaches 100%, condensation occurs and clouds begin to form. The altitude at which condensation begins is called the Lifting Condensation Level (LCL). The depth through which the air mixes is termed the 'mixed layer', which also corresponds to the boundary layer depth in case of shallow marine boundary layers (MBL). Strong LW cooling at the top of the clouds and simultaneous warming associated with the large-scale subsidence forms and maintains the thermal inversion that acts to suppress the vertical extent of mixing as well as the cloud tops. Thus, marine Sc clouds are typically 200-400 m thick and occur at the top of the MBL below a thermal inversion.

LW cooling at cloud-tops is also the main driver of the turbulent eddies that maintain the Sc cloud layer by coupling it with the surface source of moisture. Latent heating due to condensation of water vapor within the upward rising air and evaporative cooling associated with the drying of the cloud water, provide an additional source of turbulent mixing that strengthens the convection. Another key process occurring in the Sc clouds is the entrainment of dry, warm air from the free troposphere into the cloud tops. Cloud-top entrainment occurs when the evaporation of cloud water into a thin layer immediately above the cloud tops cools the air parcels in the mixing region and makes them negatively buoyant enough to sink into the cloud layer. A schematic illustrating these key processes associated with the Sc topped boundary layer (STBL) are shown in Fig 1.6 that has been adapted from Wood (2012).

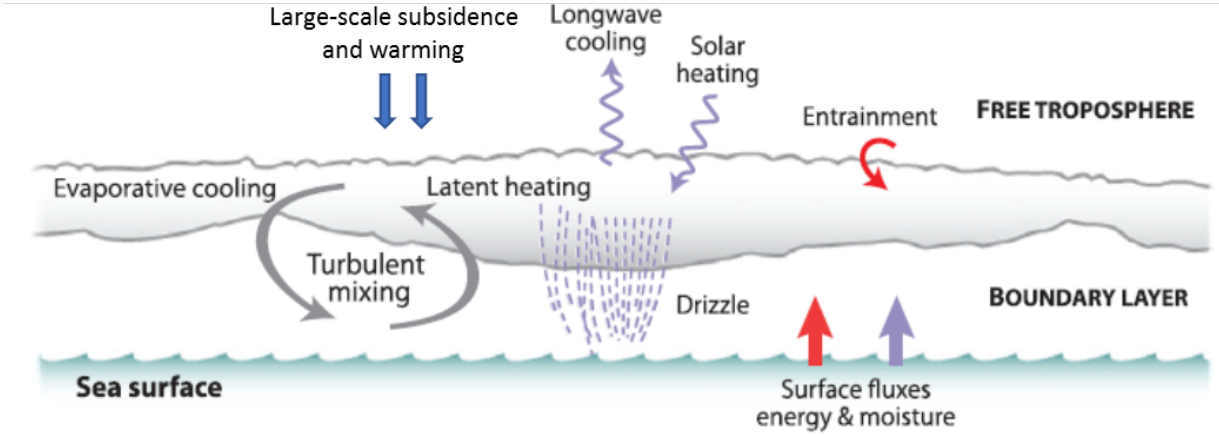

Figure 1.6 Schematic showing key processes occurring in the stratocumulus-topped boundary layer, adapted from Wood (2012).

For the reasons described above, the vertical and horizontal structure of marine Sc clouds are strongly tied to the vertical structure of the MBL in which they reside [*Lilly* 1968; *Wood and Hartmann* 2006]. For a well-mixed STBL with moderately shallow depths of about 0.5-1 km, the moist-conserved variables such as equivalent potential temperatures or total water content are nearly constant, a near-dry adiabatic lapse rate exists below the cloud base, a moist adiabatic lapse rate persists above the cloud base, and the capping inversion is quite strong. Fig 1.7 shows an example such a STBL and its vertical structure that closely resembles the MBLs occurring over SE Atlantic. Horizontal winds in such STBLs are approximately constant with height, other than at levels very close to ocean surface. A sharp jump in wind speeds and/or directions however, occurs across the inversion layer that also observes strong gradients in thermodynamic properties of humidity and cloud water (Fig. 1.7) along with the radiative cooling rates.

Although marine Sc clouds are typically only a few hundred meters thick, a compilation of their observed thickness from various field campaigns showed that the variability in this thickness range is quite limited [*Wood* 2012]. This can most likely be explained by a major regulating feedback termed the cloud–radiation–turbulent–entrainment feedback after Zhu et al. (2005). In short, the way this feedback works is as follows. For relatively shallow STBLs under a dry free troposphere, cloud-top entrainment decreases cloud thickness by incorporating warm, dry air that raises the cloud base faster than it lifts the STBL top [*Randall* 1984]. The cloud-top entrainment is strongly aided by evaporative cooling of cloud water and therefore the entrainment rate increases for thicker clouds that have greater condensate amounts. On the other hand, shallower clouds are associated with stronger inversion above cloud-tops. Thus, a lot more energy is required to bring in dry air from a higher potential to lower potential levels, thereby lowering the cloud-top entrainment rates. In summary, a thickening cloud drives stronger entrainment, resulting in cloud thinning, whereas a thinning cloud suppresses entrainment and thereby allows for the cloud to thicken. [*Wood* 2012].

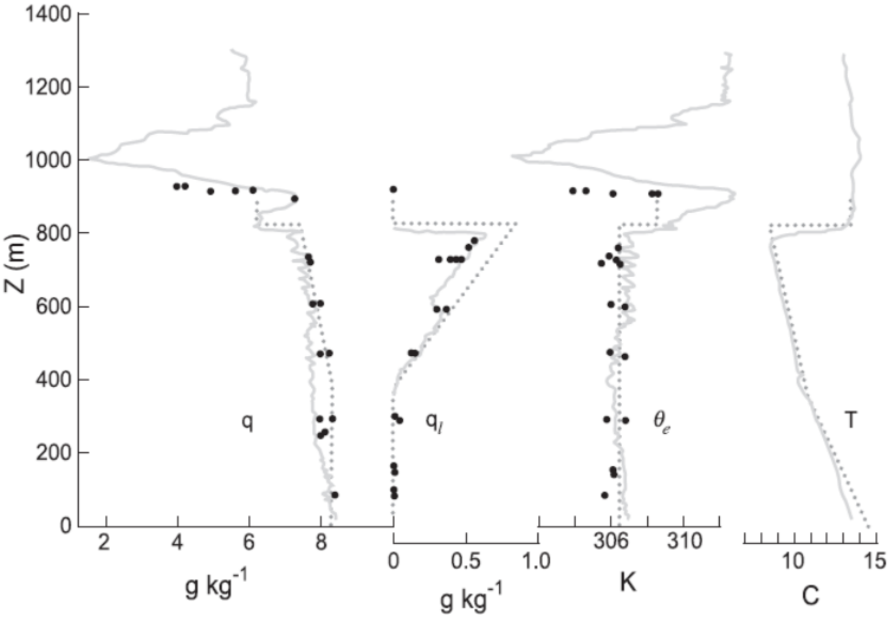

Figure 1.7 Ideal (dotted line) and measured (solid line) vertical profiles of vapor (q) and liquid water (q_l) mixing ratios, equivalent potential temperature (θ_e) and dry air temperature (T) for a summertime shallow and quite well-mixed STBL over the North Sea. The figure is adapted from Nicholls (1984).

The liquid water content of a cloud is a primary determinant of its optical properties [Stephens 1978a] and therefore is an important link between the cloud dynamics and radiative effects. Reflectivity (or albedo) of clouds strongly depends on the cloud optical thickness (τ_c). For Sc clouds, cloud droplets are much larger than the wavelengths of incoming solar radiation and τ_c is directly proportional to the vertical integral of the ratio of cloud liquid water content to the effective radius of the cloud droplets (r_e). Since q_l increases almost linearly with height (Fig. 1.7) and vertical stratification in cloud droplet concentration is very small [*Wood* 2005a], τ_c can thus be approximated as follows:

$$\tau_c = \frac{9L}{5\rho_w r_e(h)} \tag{1.8}$$

Here, ρ_w is the density of liquid water, ρ is air density and h is the cloud thickness and $L = \int_0^h \rho q_l \, dz$ is the liquid water path (LWP).

1.5 Thesis Organization

To address the objectives of this thesis study that were outlined earlier, we have focused on Goddard Earth Observing System, version 5 (GEOS-5) Atmospheric General Circulation Model (AGCM). The observational focus is on Cloud Aerosol Lidar with Orthogonal Polarization (CALIOP), which is a satellite remote sensing instrument that has been providing measurements of aerosol and cloud spatial distribution from space for over a decade now. Further details on the two tools are provided in Chapter 2. This thesis study is divided into three major parts. The first part deals with the evaluation of BB aerosol transport and vertical distribution in GEOS-5 over the complete South African-Atlantic region. This is covered in Chapter 3. The second part is aimed to explain the possible cause(s) of differences between modeled and observed aerosol transport over SE Atlantic. To this end, BB aerosol outputs from multiple global models were used to find common or distinguishing biases and the representation of various physical processes affecting the aerosol transport within GEOS-5 were investigated. The findings from these investigations are discussed in Chapter 4 and 5. Lastly, Chapter 6 details the findings of my ongoing work on testing the GEOS-5 model sensitivity to changes in aerosol vertical distribution with respect to the simulation of underlying cloud properties and radiation budget over SE Atlantic.

CHAPTER 2. MODEL AND OBSERVATIONS

2.1 GEOS-5 Atmospheric General Circulation Model

The GEOS-5 Earth System model is a weather-and-climate capable model consisting of components for atmospheric circulation and composition, oceanic circulation, land surface processes and data assimilation [*Rienecker et al.,* 2008]. The model can be operated in different modes viz. climate mode, data assimilation mode or replay mode. In the climate mode, the model behaves as a free-running Atmospheric General Circulation Model (AGCM) forced by climatological sea surface temperatures (SSTs) that requires just the initial conditions to make a forecast [e.g., *Randles et al.,* 2013]. In assimilation mode, the AGCM is integrated with the Gridpoint Statistical Interpolation (GSI) atmospheric analysis system that performs a meteorological analysis to adjust the dynamical state (winds, pressure, temperature, and/or humidity) of the AGCM every 3 or 6 hours [e.g., *Rienecker et al.,* 2011]. To avoid the computational cost of performing the analysis every time the model is operated in the replay mode, in which the model is forced using a previous analysis that was produced using an identical version of the current AGCM [e.g., *Bian et al.,* 2013]. The replay mode is closest to how most of the offline Chemical Transport Models (CTM) work.

The GEOS-5 AGCM combines the finite volume dynamical core of Lin (2004) with a column physics package that contains the following: turbulence is based on the Lock (2000) scheme, acting together with the Richardson-number based scheme of Louis and Geleyn (1982), relaxed Arakawa-Schubert (RAS) convection [*Moorthi and Suarez*,1992], and a large-scale cloud scheme based on Bacmeister et al. (2006). The catchment land-surface model is based on Koster et al. (2000) and the Radiative transfer module is based on the parameterization of Chou and Suarez

(1994, 2002) and Chou et al. (2003). Some of these physical parameterizations have been adjusted over time to allow for the model to simulate a climate closer to the global observations. The most important impacts were observed from the changes in moist processes and turbulent parameterizations, the details of which are provided in Molod et al. (2012, 2015).

A version of the Goddard Chemistry, Aerosol, Radiation, and Transport model [GOCART, *Chin et al.*, 2002; 2009] was added as an aerosol module in GEOS-5 [*Colarco et al.,* 2010] and is used to simulate the processes of sources, sinks, transport, and transformation for aerosols and tracers within the GEOS-5 system. The module simulates five tropospheric aerosol species: dust, sea salt, black carbon (BC), organic carbon (OC), and sulfate. The aerosol species in GEOS-5 are assumed to be external mixtures that do not interact with each other. The module simulates the following physical processes for aerosols: emission, advection, moist convection, boundary layer turbulent mixing, wet scavenging and dry deposition [*Chin et al.*, 2002]. The wet scavenging consists of both scavenging in convective updrafts and rainout/washout in large-scale precipitation. Dry deposition includes gravitational settling as a function of aerosol particle size and air viscosity and surface deposition as a function of surface type and meteorological conditions [*Chin et al.*, 2004].

Except for dust, the optical properties of the other aerosol species are primarily prescribed using the OPAC data set [*Hess et al.*, 1998]. Mineral dust optics, mainly refractive index (RI) and particle shape assumptions, were revised based on space-based remote sensing data [*Colarco et al.,* 2014]. Efforts to incorporate a more sophisticated aerosol microphysics scheme into GEOS-5 based on the Modal Aerosol Module (MAM) from Liu et al., (2012) are also underway such that a more realistic accounting for the mixing state and growth of aerosols can be accomplished. For this study although, we have concerned ourselves with the GOCART aerosol module only.

Therefore, we may often refer to GEOS-5 as GEOS5-GOCART as well, to highlight this AGCM-aerosol module combination and to avoid confusing it with GEOS-CHEM, which is a separate CTM and whose results we have used in our inter-model comparisons later.

2.1.1 Biomass Burning Emissions

One of the most commonly used BB emission inventories for global models across the world is Global Fire Emission Database version 3.1 (GFED3) [*Randerson et al.,* 2013; *van der Werf et al.,* 2006]. GEOS-5, however, allows its users to prescribe the model with BB emissions from a different set of estimates as well, called the Quick Fire Emission Dataset version 2.4 (QFED2) [*Darmenov and da Silva,* 2015]. The main difference between the two emission inventories lies in the methodology each of them uses to estimate the amounts of aerosols and carbon monoxide (CO) emitted during BB.

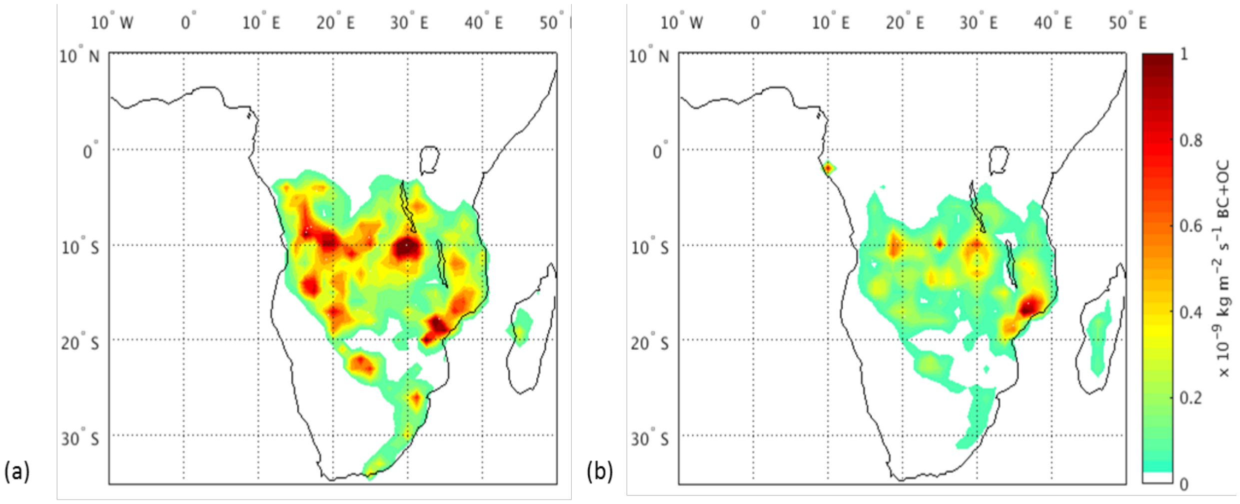

Figure 2.1 Input emissions of BC and OC (× 10^{-9} kg m^{-2} s^{-1}) from (a) QFED2 and (b) GFED3 biomass burning inventory averaged over August and September 2008.

QFED estimates are based on an empirical relation between MODIS retrieved fire radiative power and the total dry mass burned over the affected area (top-down approach), while GFED uses the properties of burning ecosystem along with the characteristics and extent of fires to estimate the amount of mass emitted for different aerosol species and trace gases during BB (bottom-up approach). The spatial distribution of combined BC and OC mass emitted over our domain from the two inventories are depicted in Figure 2.1. The regional average over the peak BB months amounts to 0.02×10^{-9} and 0.04×10^{-9} kg m^{-2} s^{-1} for GFED3 and QFED2 respectively, thus QFED emission estimates being twice that of GFED3. Further, GEOS5-GOCART treats emission injection heights by assuming BB emissions to be uniformly distributed throughout the planetary boundary layer (PBL) of the grid box containing fire emissions reflecting the effects of enormous heat generated during this burning [*Colarco et al.,* 2010].

2.2 **CALIOP Lidar Observations**

The CALIPSO (Cloud-Aerosol Lidar and Infrared Pathfinder Satellite Observations) satellite carrying the CALIOP lidar system was launched in April 2006 as part of the 'A-train' constellation of sun-synchronous satellites that cross the equator in the early afternoon around 1330 local solar time (LST) in ascending orbit and at 0130 LST in the descending node, with a 16-day repeat cycle. CALIOP measures the backscatter intensity and the orthogonally polarized components of the backscatter signal at two wavelengths, 532 nm and 1064 nm with a very fine vertical resolution of 30 m within the troposphere. The lidar system has a small footprint of only about 70 m and the laser pulse repetition frequency of 20.16 Hz produces footprints every 335 m along the ground [*Hunt et al.*, 2009; *Winker et al.*, 2009].

The attenuated backscatter measurements are made available in the Level 1 CALIOP products after geolocation and calibration and then converted to useful geophysical parameters, such as backscatter and extinction coefficients, and layer optical depths, using a series of data processing algorithms [*Winker et al.*, 2009; *Young and Vaughan*, 2009]. For the CALIOP Version 3.01 products, the identified aerosol layers during the processing algorithm are further classified into six aerosol types using a model-based scheme of Omar et al. (2009). These are polluted continental, biomass burning (or smoke), desert dust, polluted dust, clean continental, and marine. Several aerosol and cloud optical properties derived using the processing algorithms, aerosol classification information, spatial location of aerosol and cloud layers, along with the surrounding meteorological conditions (e.g., temperature, pressure or surface elevation) measured by the instrument are made available to users through the CALIOP Level 2 products.

The Level 2 data files also contain several quality control flags that can be used to screen out poor or highly uncertain data. The significance of these flags and the directions to use them are explained in *Winker et al.* [2013]. To briefly summarize, we have used cloud aerosol distinction (CAD) scores, extinction uncertainty values, atmospheric volume descriptors (AVD) and extinction quality control (QC) flags to filter our extinction data before averaging them or using them for any comparative analysis. CAD score is a measure of confidence in the classification of identified layers into aerosol or cloud, with negative values for aerosols and positive values for clouds [*Liu et al.*, 2009]. Therefore, observations with absolute CAD scores of only 20 or above were used. The extinction QC flags summarize the initial and final state of the extinction retrieval. During the execution of the algorithm to find a solution, the lidar ratio may be adjusted, but there is most confidence in extinction solutions when the lidar ratio is unchanged during the retrieval process (extinction QC = 0) or if the retrieval is constrained (extinction QC = 1) [*Young and Vaughan*, 2009]. Hence, we used observations that had QC flags of either 1 or 0. The retrieval process may also fail sometimes because the iterative process did not converge to a solution. Under such conditions, an extinction uncertainty of 99.99 is assigned to indicate an unreliable solution.

So, all observations with an uncertainty of 99.99 km^{-1} were also discarded. Additionally, all extinction observations with AVD indicating clean air were assumed to have zero extinction values (instead of fill values of -9999) while calculating the mean extinction profiles [*Ford and Heald*, 2012].

2.2.1 Inherent Limitations and Algorithm Biases

While CALIOP provides unmatched observations of aerosols and clouds across the globe that are vital for model evaluations, it is also important to note its limitations and biases to treat the data within some uncertainty limits. Firstly, to examine the long-range transport events that happen on timescales of several days, the limited spatial coverage of satellites with small footprints like CALIOP make it difficult to determine the broad characteristics of the plume transport. To overcome this limitation, studies often average the data at much larger scales of horizontal distance and time than the models. Additionally, the use of only the nighttime retrievals of CALIOP are suggested as opposed to the use of both day and nighttime retrievals [*Meyer et al., 2013*; *Winker et al.*, 2013]. This is because the smaller signal-to-noise ratio (SNR) during the daytime owing to the noise from background solar illumination decreases CALIOP's detection sensitivity towards tenuous aerosol layers, resulting in low-biased AOD values. Specific to our domain, the diurnal differences in CALIOP retrieved smoke aerosol extinctions are evident in Fig. 2.2

More importantly, assessment of the above-cloud aerosol optical depth (ACAOD) of biomass burning plumes retrieved from A-train sensors over the SE Atlantic found that CALIOP's operational 532 nm retrievals were underestimated by a factor of 5 or even more compared to those from passive sensors like MODIS, OMI (Ozone Monitoring Instrument) and POLDER (Polarization and Directionality of Earth Reflectances) [*Jethva et al., 2014; Torres et al., 2013*]. At the same time, CALIOP 1064 nm retrievals when converted to 500 nm using POLDER's

Ångstrom exponent (α) brought the lidar retrievals closer to other observations. More recent observations from CATS Lidar onboard the International Space Station (ISS) found that the average aerosol layer base heights are closer to cloud tops by about 0.5 km compared to what was previously known from CALIOP [*Rajapakshe et al.,* 2017]. This overestimation of aerosol base heights therefore, might be contributing to the underestimation of ACAOD from CALIOP. The possible reasons for this aerosol base-height estimation are discussed below. Nonetheless, since CATS has been operational for only a little over two years, available aerosol retrievals are not enough to produce a climatology of aerosol extinction profiles required for constraining a global model at its horizontal scales.

CALIOP lidar signal can undergo substantial attenuation owing to the optically thick aerosol layers existing above the burning sources. The signal can at times be completely attenuated at levels within the aerosol layer, leading to no further retrievals below those levels. At other times however, the reduction in SNR (signal-to-noise ratio) due to signal attenuation may lead to misclassification of aerosol type within the aerosol layers [*Kacenelenbogen et al.,* 2014] by the operational CALIOP aerosol classification algorithm [*Omar et al.,* 2009]. The situation is worsened for measurements above the bright surfaces like clouds, where the reflection of solar radiation from such surfaces contributes to the reduction in SNR ratio. In fact, when CALIOP observations were compared with those from High Spectral Resolution Lidar (HSRL-1) [*Burton et al.,* 2013] and AERONET [*Mielonen et al.,* 2009] in terms of aerosol sub-type classification over other regions of BB pollution, results showed poor agreement for smoke (only 13%) or fine absorbing aerosols (only 37%) relative to the other aerosol subtypes. Furthermore, polluted dust was found to be overused as an aerosol type by the CALIOP aerosol classification algorithm due to an attenuation-related depolarization bias [*Burton et al.,* 2013] in regions of heavy smoke.

CHAPTER 3. AEROSOL TRANSPORT AND VERTICAL DISTRIBUTION

3.1 Background, Motivation and Objectives

Open biomass burning (BB) is a major source of trace gases and carbonaceous aerosol particles in the atmosphere. The smoke aerosol from BB is comprised of strongly absorbing black carbon (BC) particles and fine organic carbon (OC) particles, whose proportions vary according to vegetation type, oxygen availability and combustion phase [*Andreae and Merlet*, 2001]. In the southwestern African Savanna, there is seasonal burning of grasslands and agricultural residue in the Austral spring (July-October) contributing to about one-third of the global BB emissions [*van der Werf et al.*, 2010]. The optically thick aerosol plumes produced by this burning are primarily transported westward for thousands of kilometers by the free tropospheric winds over the Atlantic Ocean [*Edwards et al.,* 2006]. However, unlike smoke from industrial activity and biofuels that intermingle with clouds in most regions [*Ramanathan et al.,* 2001; *Mechoso et al.,* 2013], smoke layers in the SE Atlantic have been observed to mainly overlie the vast stretches of marine stratocumulus clouds [*Chand et al.,* 2009; *Wilcox,* 2010; *Adebiyi et al.,* 2015].

Modeling studies over this region have found significant estimates of a negative top of the atmosphere semi-direct radiative effect (-2.6 W m^{-2}) associated with increased low cloud cover over the oceanic region, which is also capable of causing the ocean surface to cool by 1–2 K or more [*Sakaeda et al.,* 2011]. The changes in the atmospheric heating profile and surface temperature due to the presence of carbonaceous aerosols cause a thermally driven anomalous circulation from the western Atlantic toward the West African coast that favors the transport of moisture to the continent from the adjacent ocean. This results in the increase of clouds, water vapor, and eventually precipitation during the wet season [*Randles and Ramaswamy,* 2010; *Roeckner et al.,* 2006]. Thus, robust estimation of the aerosol direct and semi-direct effects by the model simulations is crucial in assessing the effects of aerosol on large-scale circulations and subsequently on regional and global climate. To this end, previous model-based studies on aerosol-cloud interactions [*Johnson et al.*, 2004; *Koch and Del Genio*, 2010; *McFarquhar and Wang*, 2006; *Penner et al.*, 2003] and on the direct radiative forcing of carbonaceous aerosol [*Abel et al.*, 2005; *Samset et al.*, 2013] have emphasized that a significant fraction of the uncertainty in the magnitude and sign of the modeled aerosol radiative effects comes from the diversity in the simulated vertical profiles of aerosol concentrations amongst the models. Thus, to be useful for any climate change studies, aerosol simulations must have the ability to reproduce the observed vertical distribution of aerosol, especially with respect to clouds, in addition to their optical thickness and absorbing properties.

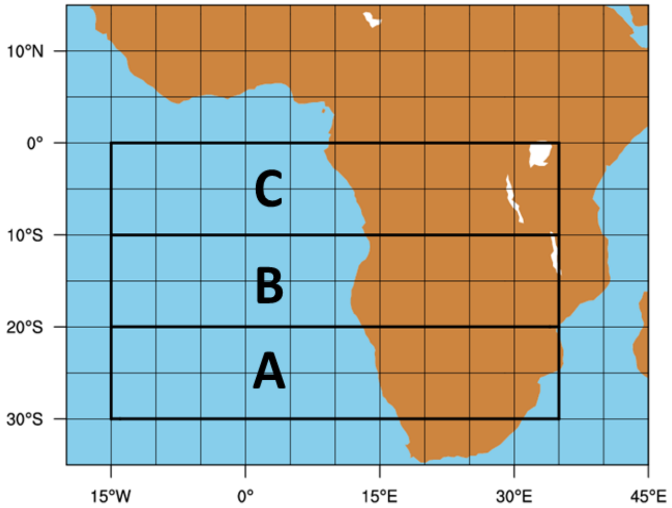

Figure 3.1 The region of interest is divided into sub-regions A (30°-20°S, 35°E-15°W), B (20°-10°S, 35°E-15°W) and C (10°S-0°, 35°E-15°W) to distinguish between the different aerosol transport features within the domain.

Specific to our domain of interest (Figure 3.1), simulations of aerosol vertical distributions by the Goddard Chemistry Aerosol Radiation Transport (GOCART) model have been evaluated previously using CALIOP observations explicitly [*Yu et al.,* 2010] and as part of the AeroCom (Aerosol Comparisons between Observations and Models) project [*Koffi et al.,* 2012; *Koffi et al.,* 2016] as well. These studies performed their evaluations only over the South African (SAF) burning source region of our domain but not over the South Atlantic region influenced by long-range transport. Koffi et al. (2012) found the shape of the mean aerosol extinction profiles simulated by GOCART and those derived using CALIOP version 3.01 data over SAF (over land) to be in reasonable agreement with each other, but the model underestimated the magnitude of extinctions at different levels within the lowest 4 km above the model surface causing an overall underestimation of model aerosol optical depth (AOD) compared to both MODIS (Moderate Resolution Imaging Spectroradiometer) and CALIOP retrievals.

GOCART was integrated within the Goddard Earth Observing System model (GEOS) as an aerosol module [*Colarco et al.,* 2010] for various applications. More recently, the latest version of GEOS (version 5), coupled to GOCART, was used to produce the Modern-Era Retrospective analysis for Research and Applications Aerosol Reanalysis (MERRAero) global data set [*Buchard et al.,* 2015] that included the assimilation of bias-corrected MODIS-derived aerosol optical depths (AODs) in addition to the assimilation of traditional meteorological parameters (winds, pressure, and temperature fields) [*Rienecker et al.,* 2008]. The assessment of MERRAero BB aerosol properties using independent observational data sets showed that MERRAero AOD estimates were highly correlated with MISR (Multiangle Imaging Spectroradiometer) and AERONET (Aerosol Robotic Network) AOD estimates over our domain. However, MERRAero BB aerosol vertical distribution after long-range transport into the southeast (SE) Atlantic also exhibited large differences with CALIOP measurements, as shown further in Chapter 5.

Extending from the findings of previous studies, our primary objective is to evaluate the simulation of long-range transport and vertical distribution of BB aerosol by GEOS5-GOCART over the complete South African-Atlantic region using CALIOP observations. We will also compare the GEOS-5 simulations with other global aerosol models participating in the AeroCom Phase III experiments to find any distinguishing or common model biases. This multi-model evaluation of aerosol transport in discussed in Chapter 4. Since the vertical distribution of BB aerosol in a model depends on a number of physical and chemical processes in addition to the emission source strength, namely, (1) the injection height (vertical distribution of aerosol emissions), (2) the convective transport, (3) dry and wet removal, and (4) physical aging [*Allen and Landuyt,* 2014], our study also aims to find the most relevant processes in our context that may be responsible for the discrepancies between the observed and GEOS-5-simulated BB aerosol vertical distribution. The results of this study will help us understand the differences between the models and observations, the possible cause(s) for these differences, and a direction for improvement in model performance in this important region of BB aerosol transport.

3.2 Approach and Methods

3.2.1 Experimental Setup for GEOS-5

GEOS-5 was run in the replay mode using Modern-Era Retrospective Analysis for Research and Applications (MERRA) meteorological analyses to adjust its dynamical state every 6 hours. The model was run at 1° (latitude) × 1.25° (longitude) horizontal resolution with 72 hybrid vertical sigma levels between the surface and 0.01 hPa (about 85 km) to provide 3-hourly outputs of aerosol-related properties.

For this study, we also utilized the carbon-monoxide (CO) simulating capability of GOCART, which was incorporated in the GEOS-5 model based on the study of Bian et al. [2007]. Simulations of CO using the same BB emission sources as aerosol were important to our study because CO is emitted simultaneously with carbonaceous aerosol during biomass burning but does not undergo the aerosol loss processes of dry and wet deposition [*Bian et al.,* 2010]. This makes CO a good tracer to evaluate the transport processes in the model. The details of how each of the aerosol species are treated in the GOCART module are discussed in Colarco et al. (2010) while CO chemistry and transport are discussed in Bian et al. (2010). Here, we will only summarize the BB emission sources and chemistry representation of carbonaceous aerosol and CO within the GOCART module.

BC is emitted as 80% hydrophobic and 20% hydrophilic, while OC is 50% hydrophobic and 50% hydrophilic [*Chin et al.,* 2002; *Cooke et al.,* 1999]. The aging process converts the hydrophobic part of the carbonaceous aerosols into hydrophilic phase with an e-folding time of 1.1 to 2.5 days [*Chin et al.,* 2002; *Maria et al.,* 2004]. The loss processes for these aerosols involve dry deposition for both hydrophobic and hydrophilic components and wet scavenging for only the hydrophilic aerosols. The chemical processes of loss and generation of CO are accounted by two chemical reactions in the module. CO is dissipated via reaction with the hydroxyl radicals (OH), while it is produced via oxidation of methane (CH4). However, the generation of CO from the oxidation of non-methane hydrocarbons is parameterized as a direct emission [*Bian et al.,* 2007]. Both OH and CH4 concentration fields are derived using the results from a global chemistry and transport model simulation, the Global Modeling Initiative (GMI) [*Bian et al.,* 2013].

3.2.2 CALIOP Data Processing

For this part of the study and the multi-model evaluation in the following chapter, we have used the CALIOP 1064 nm extinction retrievals for obtaining the mean smoke extinction profiles instead of the standard 532 nm product owing to the large differences in extinction magnitudes between the two that were discussed in the previous chapter. To convert the 1064 nm extinction retrievals to the model's output frequency of 550 nm, we calculated $\alpha = 1.8$ for the 440-1020 nm pair using Level 1.5 monthly mean AOD measurements from nine different AERONET sites (http://aeronet.gsfc.nasa.gov) over the BB source region of our domain. This is consistent with the Eck et al. (2013) study, where the values of α in the 440–870 nm ranged primarily from 1.7 to 2.0 with a mean of 1.85 over the same region.

To ensure a better representation of the regional climatology, we obtained a gridded product of CALIOP data by aggregating the smoke extinction profiles at 550 nm, converted from 1064 nm, for the peak biomass burning months of August and September from 2007-2009 onto global 2° × 2° latitude-longitude grids. The median of the total number of valid CALIOP 5-km profiles per grid cell was 565, with maximum and minimum values of 1047 and 397 respectively. Further, the variation in the number of valid CALIOP observations with decreasing altitude up to the cloud or surface levels was found to be negligible over most parts of the domain compared to the total number of valid retrievals made at each level. The use of multi-year averages of observational data instead of exactly matching satellite and model data seems a reasonable decision for our case because we found low inter-annual variability in the magnitudes and shape of the smoke extinction profiles over our domain for the time-period of averaging (see also *Koffi et al.* [2012]).

3.3 Results and Discussion

GOCART was run 'online' with GEOS-5 in replay mode for the complete year of 2008 using a model configuration described in the previous section. During the analysis and discussions in the subsequent sections, note that the mean of the model output quantities always represents an average over August and September 2008 while that for CALIOP represents an average over the same months but from 2007 through 2009. Since the temporal range of the CALIOP and model data do not overlap exactly, we do not intend to perform a detailed quantitative analysis of magnitudes of aerosol extinctions or optical depths, but rather compare the broad features of aerosol spatial distribution and transport simulated by the models relative to CALIOP retrievals. The GEOS-5 simulated smoke extinctions in our analysis refer to the sum of extinctions for BC and OC components in the model, assuming that the contribution of anthropogenic BC and OC towards the total BC and OC over our domain and study period is negligible [*Streets et al.* 2009].

3.3.1 Horizontal Distribution of Smoke and Clouds

Although the emphasis in this study is on the vertical distribution of BB aerosol, we begin with the examination of smoke aerosol optical depths and cloud fractions from satellite observations and model simulations to understand the general characteristics of smoke and cloud spatial distribution in the region. The mean smoke AOD from CALIOP (Fig. 3.2a) was derived by integrating the smoke extinction values from our gridded product (described in section 3.2) over all the CALIOP levels. The gridded AOD product was smoothed using a convolution filter for plotting purposes to facilitate the visualization of the spatial pattern of the underlying data. The low-level cloud fractions, depicted by the blue line contours in Fig. 3.2a, were obtained from Level-3 MODIS Atmosphere Monthly Global Product (MOD08_M3) at 1° spatial resolution for

Aug-Sep 2008. The corresponding cloud fractions and mean smoke AOD simulated by GEOS-5 (using QFED2 emissions) are shown in Fig. 3.2b.

In general, the gradual decrease in the magnitudes of smoke AOD starting from the burning source region to the west of the continent for both modeled and CALIOP data is consistent with our understanding of the directions of smoke outflow for the savannah fires. However, some noticeable differences in the horizontal distribution of modeled and observed smoke AOD over the continent are also evident. For example, there is an area of high AOD values observed by CALIOP between 10°-15°S and 25°-30°E, which seems to be missing (or misplaced) in GEOS-5 simulations. Interestingly, this area of high AOD values retrieved by CALIOP corresponds to the large fire pixel counts observed by MODIS (Fig. 1.1) and relatively high values of QFED2 estimated emissions (Fig. 2.1a) around the same region. One of the probable reasons of this discrepancy could be the quick outflow of smoke plumes from the intense burning source towards the north of the continent due to the occurrence of high wind speeds over this area in the model, along with the formation of a confluence north of this region. These high wind speeds and confluence at the surface levels are apparent from the horizontal wind streamlines of MERRA reanalysis data in Fig 4.4 of Chapter 4.

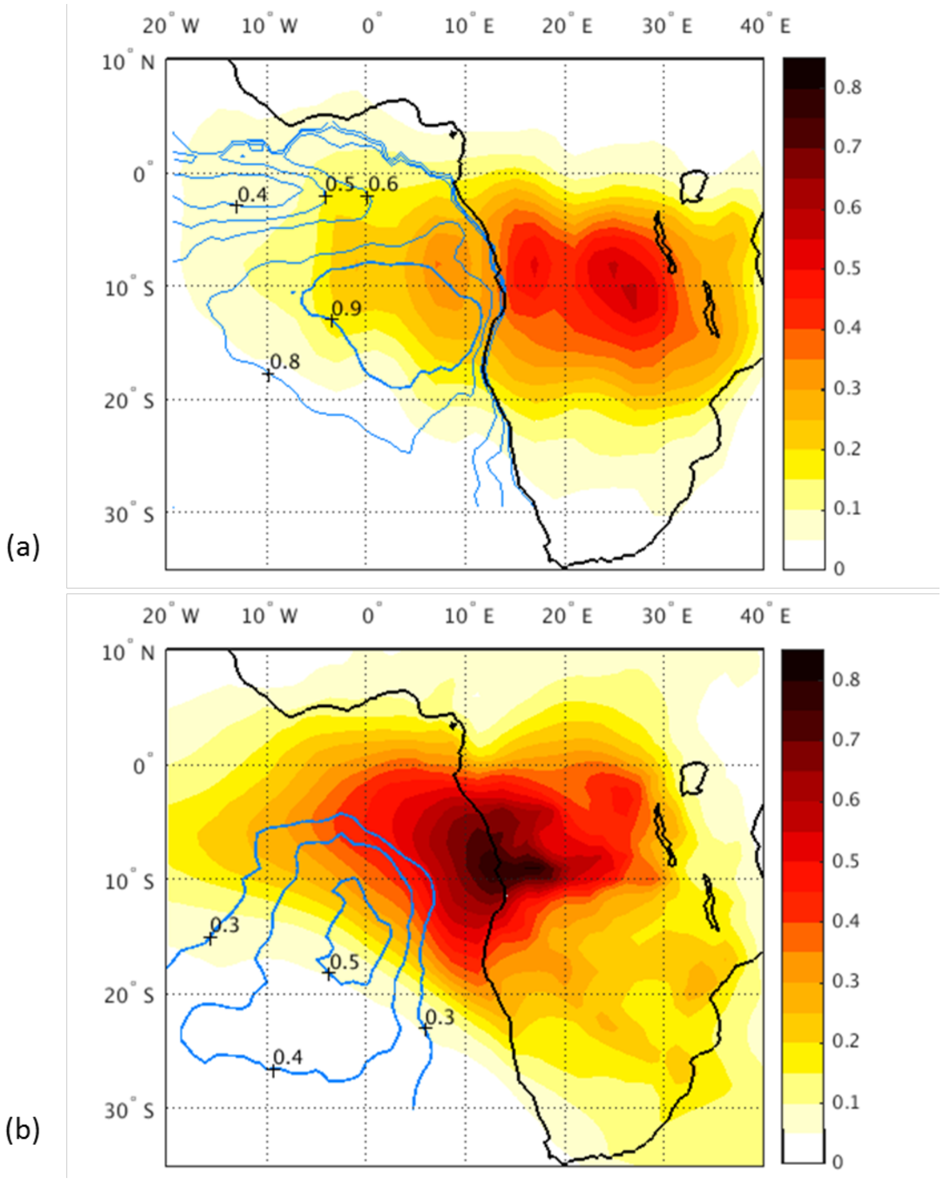

Figure 3.2 (a) Horizontal distribution of BB AOD (colored contours) from CALIOP gridded product (described in 3.2) and low-level cloud fractions (blue line contours) from MODIS Level 3 monthly global product (MOD08_M3) for August-September 2008, and (b) corresponding results from GEOS-5 simulations using QFED2 BB emissions.

The low-level cloud fractions from MODIS are also vastly different from those simulated by GEOS-5 in terms of both magnitudes and spatial distribution. The MODIS clouds appear to be hugging the western coast of the continent and extend into the deep ocean with cloud fractions greater than 0.9 between 5°S to 20°S. The GEOS-5 clouds, on the other hand, appear to be more southwards and further away from the coast compared to MODIS clouds, with maximum cloud fraction values of only about 0.5. Having knowledge of this discrepancy might be important because the spatial location of clouds is related to the convective activity occurring at these locations. This inability of reproducing realistic stratocumulus cloud decks off the western coasts of the continents has been found to be a common problem for most of the global models that have participated in previous AeroCom experiments too [*Stier et al.,* 2013].

Table 3.1 Mean smoke AOD from GEOS-5 model, CALIOP and a previous study.

Aerosol	**Land AOD**	**Ocean AOD**
GEOS-5 smoke (using QFED2 emissions)	0.30	0.28
GEOS-5 smoke (using GFED3 emissions)	0.15	0.12
CALIOP smoke	0.30	0.14
MODIS[a]	0.38[b]	0.16[c]
CAM3-Slab Ocean Model[a] (carbonaceous)	0.27	0.14

[a]climatological mean over July-October (2001-2008) from *Sakaeda* et al. [2011]. [b]MODIS total AOD. [c]MODIS fine-mode AOD.

To establish the reasonableness of the modeled and observational data used in our study, we compare the mean smoke AOD estimates from GEOS-5 and CALIOP with those from a previous study [*Sakaeda et al.,* 2011] that was based over the same region of interest as ours (Table 3.1). We calculated the mean AOD separately for the land (0-20°S, 13°E-40°E) and the oceanic (0-20°S, 13°E-20°W) parts of the domain to allow for a fair comparison with the previous study. However, it should be noted that the observational and model estimates from Sakaeda et al. (2011)

are climatological means from 2000-2008 for the entire dry season of July-October. Table 3.1 shows that the mean smoke AOD derived using our CALIOP gridded product falls within ~20% of mean MODIS total AOD over land and within ~10% of mean MODIS fine-mode AOD over the ocean. MODIS fine-mode AOD over land was intentionally not included in our comparisons because the use of this product for evaluation studies is not recommended [*Levy et al.,* 2010]. The close agreement of CALIOP and MODIS AOD estimates re-emphasizes that retrievals of CALIOP extinctions or AOD at 1064 nm are more suitable for evaluation of model simulations instead of the standard AOD retrievals at 532 nm, which have been found to be underestimates by about a factor of 5 or more over this region [*Jethva et al.,* 2014].

Although all the estimates of mean smoke AOD over land in Table 3.1 fall within 20% of GEOS-5 simulated AOD (using QFED2), the AOD gradient from land to ocean for GEOS-5 is quite low (~10 % decrease) compared to the other estimates in the table. The reduction in AOD from land to ocean is ~50% for CALIOP and the CAM3-Slab Ocean Model. The former might be an overestimate because CALIOP cannot retrieve the smoke aerosol lying below the clouds over the ocean. Between the models (GEOS-5 and CAM3) however, the differences in AOD gradients can be partly attributed to the use of different BB emissions for each of the models. In fact, QFED2 BB emissions show the presence of heavy fires concentrated along the western coastline of the continent (Fig. 2.1a), which in conjunction with the prevailing high winds in the model, contribute to the high AODs over the ocean as well as land for GEOS-5.

3.3.2 Contrast Over Land and Ocean

3.3.2.1 Sampling along CALIPSO Tracks

We compared smoke extinctions at 532 nm retrieved from the standard CALIOP layer product with GEOS5-GOCART simulated smoke extinction-coefficients at 550 nm along nighttime CALIPSO satellite tracks to evaluate the vertical distribution of smoke aerosol in the model at different stages of the plume transport. There were typically 2-3 nighttime CALIPSO tracks every 24 hours that passed over our domain. We also used these comparisons to examine the sensitivity of the model-simulated extinctions towards the use of different BB emissions. The matching of the model and CALIOP data was done by choosing the instantaneous extinction values from the 3-hourly generated model output file that was closest to the time of CALIPSO overpass. Figure 3.3 shows three such satellite tracks that cut across the primary direction of plume transport and are representative of the typical scenarios we observed during most of the days of the BB months. The first track (from left) runs along the BB source region; the second is just off the western coast, where the plume transitions from land to the ocean; and the third track is further offshore, where the plume comfortably resides above the stratocumulus cloud deck.

The variations in the smoke layer top altitudes (~ 3.5 to 4.5 km above ground) along satellite tracks on land are in general captured by the model (Fig. 3.3 left panels). However, for the CALIPSO tracks passing along the coast and further into the ocean (Fig. 3.3 middle and right panels), some remarkable differences between the vertical distribution of the model simulated and CALIOP retrieved smoke layers exist. CALIOP observes smoke layer top heights over the ocean at ~ 4 to 5.5 km above sea level (ASL) and the layer base heights are detected mostly above 2.5 km ASL. In contrast, the bulk of the model-simulated smoke layers appear to be residing at lower altitudes than CALIOP. The difference between CALIOP and model simulated layer top heights are between 1-1.5 km in the areas adjacent to the coast (Fig 3.3 middle panels), but this difference can increase up to ~ 2 km for satellite tracks far away from the coast and between 0-10°S (Fig. 3.3 right panels). The occurrence of smoke aerosol layers at elevated altitudes above the MBL, mostly between 2 and 6 km ASL, was also observed during the Southern African Regional Science

Initiative (SAFARI 2000) [*Haywood et al.,* 2004] and other in situ aircraft measurements over the ocean in this region [*Anderson et al.,* 1996; *Kaufman et al.,* 2003].

The relative locations of the CALIOP smoke extinctions (color-filled) and cloud top heights (black line) over the ocean (Fig. 3.3 middle and right panels) suggest that CALIOP smoke layers reside well above the cloud levels with a persistent 'clear air' gap (in white) between the base of the CALIOP smoke layers and top of the cloud decks. The CALIOP estimates of this gap however can be biased at times due to the overestimation of the aerosol layer base heights by the standard feature detection algorithm of CALIOP [*Liu et al.,* 2015; *Painemal et al.,* 2014]. This bias can occur in CALIOP measurements when the backscatter intensities fall below the detection thresholds [*Vaughan et al.,* 2009] or CALIOP signal is substantially attenuated in areas of optically thick aerosol layers. Nonetheless, since the magnitudes of aerosol extinction decrease as the smoke plumes move away from the burning sources (Fig. 3.2), we can expect the effects of strong signal attenuation over the ocean to be most prevalent for the smoke layers adjacent to BB sources along the coast and up to about 0°. Therefore, for other parts of the ocean, the clear gap between the smoke and cloud layer might possibly be true or at most reflects the presence of weakly scattering aerosols within this gap. In fact, observations of aerosol and cloud vertical distributions along the flight tracks off the coasts of Namibia and Angola and around Ascension Island (~ 2500 km away from the west coast) also during SAFARI-2000 also suggested that the cloud tops were mostly separated from the overlying BB smoke layers by 'clean air slots' (*Haywood et al.,* (2004) and the references therein).

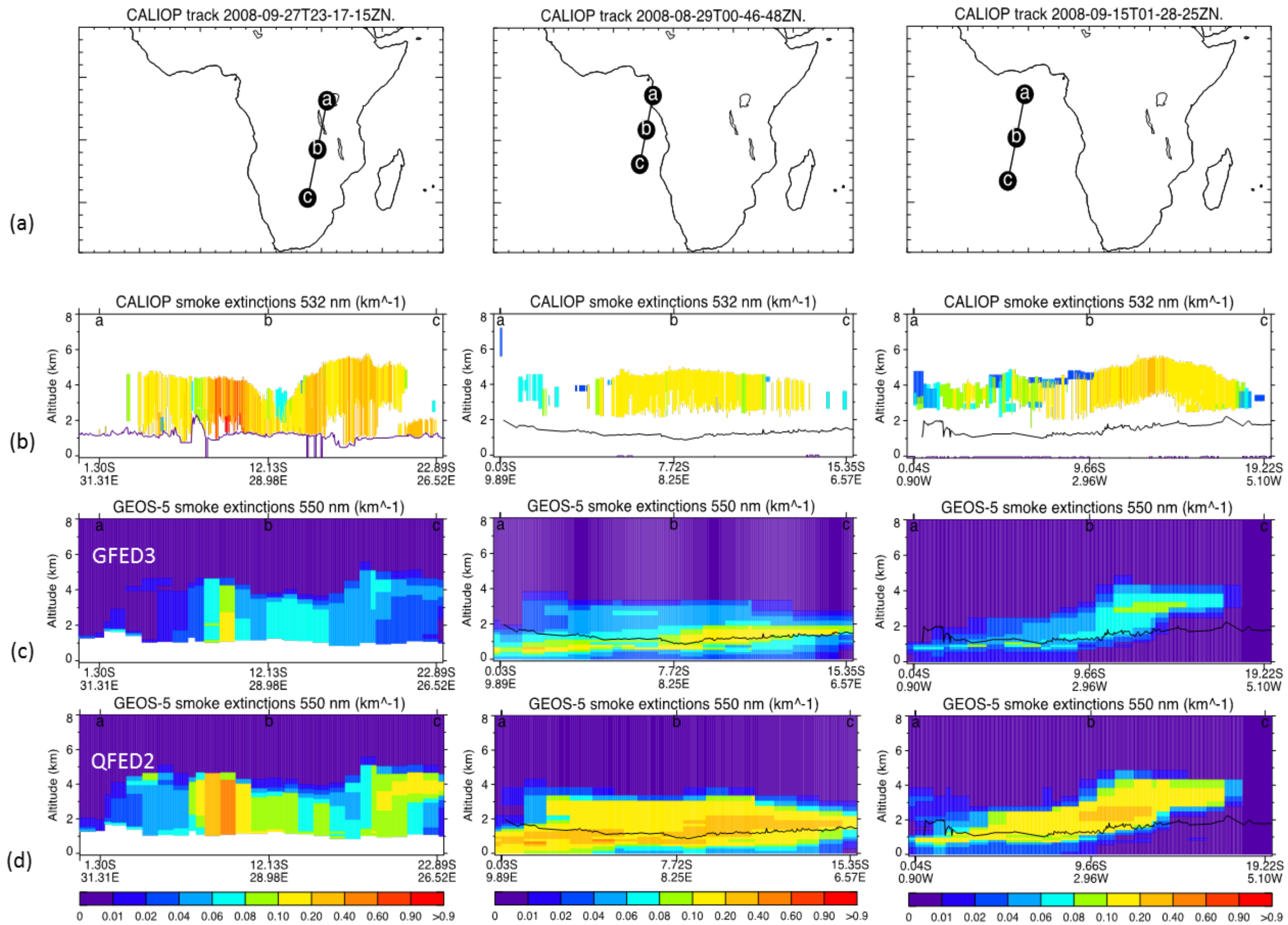

Figure 3.3 Vertical distribution of smoke aerosol extinctions (km^{-1}) along (a) three distinct CALIPSO satellite tracks retrieved from (b) CALIOP at 532 nm and those simulated by GEOS5-GOCART at 550 nm (c) using GFED3 BB emissions and (d) using QFED2 BB emissions. CALIOP retrieved cloud top heights are depicted using black lines on both CALIOP and GEOS-5 panels for tracks over the ocean. CALIOP observed surface elevation is plotted (in purple) on CALIOP panel for the track over land. White region on CALIOP panels represents no detectable signals of smoke aerosol.

Furthermore, the comparisons along satellite tracks and mean smoke AOD estimates from Table 3.1 show that by using different BB emission inventories (QFED2 and GFED3), the GEOS-5 AOD values can be changed by about a factor of 2 and the model simulated extinction or AOD values are closer to those from CALIOP when QFED2 emissions are used. However, the horizontal and vertical locations of the smoke aerosol in the model is unaffected using either of the emission inventories. Thus, for the discussions hereafter, GEOS-5 model output represents results from the QFED2 simulations unless otherwise specified.

3.3.2.2 Mean Extinction Profiles

The contrast in the GEOS-5 performance in simulating aerosol vertical distribution over the burning source region versus the smoke outflow region is further examined by comparing the mean smoke extinction profiles from GEOS-5 and CALIOP separately for the land and oceanic part of the domain (Fig. 3.4). The mean cloud extinction profiles retrieved from CALIOP are also plotted along with the smoke extinction profiles for the sub-plots over the oceanic region to visualize the vertical location of the smoke layer relative to that of the stratocumulus cloud deck. It should be noted here that we have replaced the "clean air" retrievals of CALIOP with zero extinction values, which are also accounted for while evaluating the mean aerosol or cloud extinctions at each CALIOP vertical level. Thus, the mean extinction value at a particular level for either aerosol or cloud is a resultant of both the frequency of occurrence and the magnitude of extinctions observed at that level. To avoid averaging out the distinct patterns of aerosol transport or vertical distribution that could possibly exist for different regions within the domain, we make the comparisons here and during all subsequent analysis for three sub-regions (Fig. 3.1) of equal width (10 degrees of latitude) extending from 35°E to 15°W.

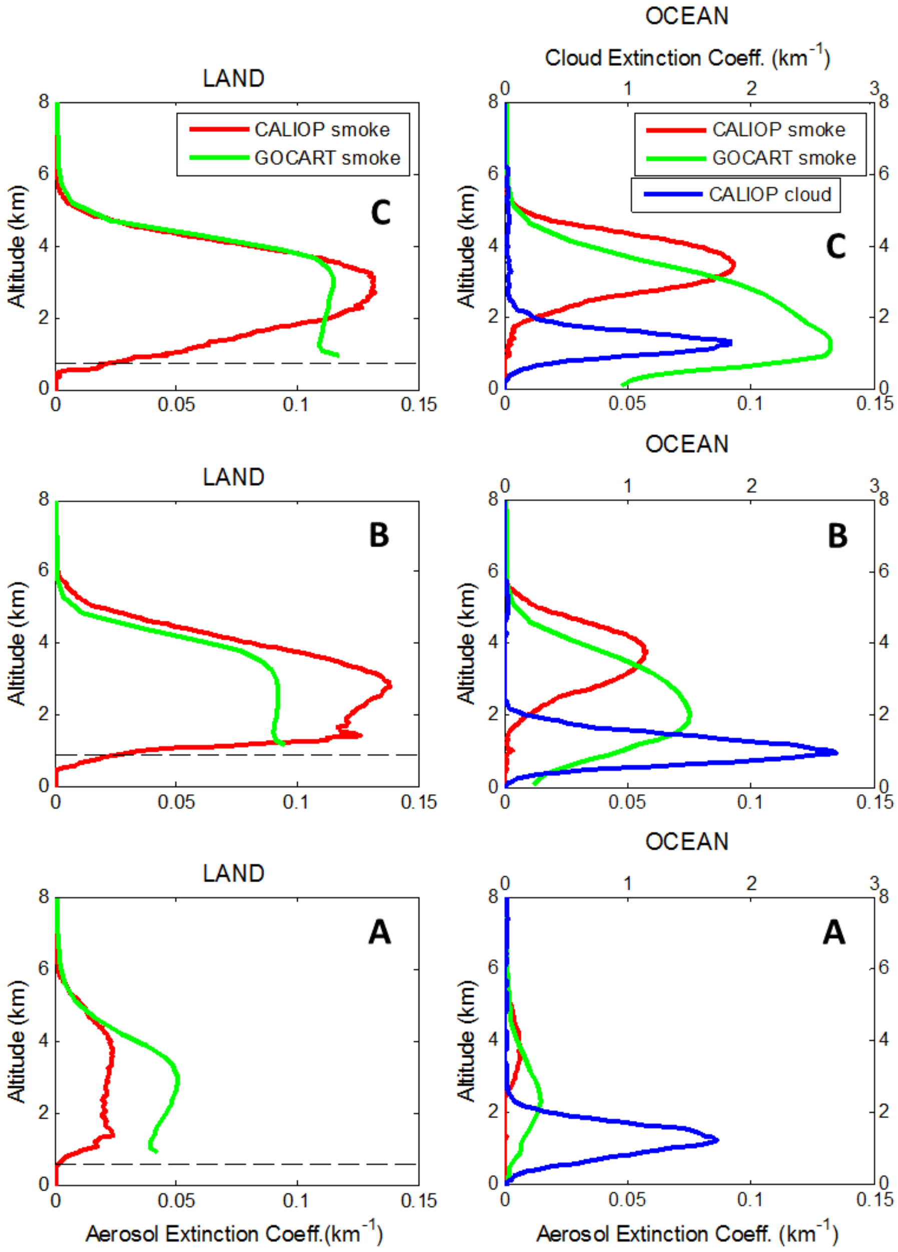

Figure 3.4 Comparisons of mean (Aug-Sep) smoke extinction profiles (km^{-1}) from CALIOP (in red) and GEOS5-GOCART (in green) over land (13°-35°E) and oceanic (13°E-15°W) parts of the three sub-regions, viz. A (30°-20°S), B (20°-10°S) and C (10°S-0°) of the domain. CALIOP-retrieved cloud extinction profiles (in blue) are plotted using the upper x-axis for profiles over the ocean to show relative altitudes of smoke and cloud layers. The mean surface elevations retrieved from CALIOP are shown using dashed lines for profiles over land.

Over land, the model and CALIOP mean extinction profiles are in reasonable agreement with each other with respect to the shape of the profiles. The magnitudes of GEOS-5 extinctions however, are underestimated for sub-region B (up to about 40%) and overestimated for sub-region A (up to about 70%) compared to CALIOP extinctions. Over ocean, the area under the extinction curve, which can be considered as a proxy for shape and altitude of peak extinction (2.5 km for GEOS-5 versus 3.5 km for CALIOP), although the magnitudes of extinctions are lowest for this sub-region compared to the entire domain. The peak of the model simulated smoke aerosol extinction profiles occurs at levels 1-2 km lower compared to the peak of the CALIOP retrieved smoke extinction profiles for all the three sub-regions. For sub-region C, the peak of the model smoke extinction profile is most displaced from that of CALIOP (at ~ 3.5 km) and interestingly coincides with the peak of the CALIOP cloud extinction profile (at ~ 1.5 km). However, it is also important to note that high relative humidity (RH) at cloud levels in the model can also contribute to an increase in aerosol extinction values at these levels. Thus, the increase in modeled aerosol extinctions at these levels does not necessarily imply a proportionate increase in the amount of aerosol at these levels, but surely depicts some amount of mixing of aerosols within the clouds.

CHAPTER 4. MULTI-MODEL EVALUATION OF AEROSOL TRANSPORT

We compared the aerosol transport features simulated by GEOS-5 over this region with other global models from the AeroCom (Aerosol Comparisons between Observations and Models) Phase-III experiments and evaluated them together using CALIOP observations. The motivation behind this was to find any common or distinguishing biases among the models in this important region of BB. GEOS-5 was run with the same configuration as Chapter 3, but the BB emissions input from GFED3 inventory instead of QFED2 to facilitate fair comparisons with other models. For the AeroCom models, since outputs of aerosol extinction coefficient were not available separately for BC and OC, the corresponding smoke extinctions were obtained as a difference between aerosol extinctions from two sets of similar simulations, one with the BB emissions and the other without them.

4.1 AeroCom Models

The AeroCom project was created in 2003 to assemble outputs from various global aerosol models at a common platform to facilitate inter-model comparisons and model evaluations using observational data sets. The modelers are requested to follow a common data-protocol and provide details about their respective model configurations depending on the objective of the proposed experiment for which they submit the results. Several studies have used outputs from AeroCom Phase I [*Kinne et al.*, 2006; *Koffi et al.*, 2012; *Schulz et al.*, 2006; *Textor et al.*, 2006] and Phase II experiments [*Koffi et al.,* 2016; *Myhre et al.*, 2013; *Samset et al.*, 2013] to evaluate the representation of aerosol emissions, lifecycle, optical properties, vertical distributions or radiative forcing in the participating models. Further details of the individual experiments and their respective objectives can be found at the main AeroCom website (aerocom.met.no).

We used the outputs from four state-of-the-art global aerosol models participating in the BB emissions experiment proposed under the AeroCom Phase-III project (https://wiki.met.no/aerocom/phase3-experiments). Although the original objectives of the BB experiment are different from our study, the results from Stage I of the experiment are relevant to us, as it required the models to simulate the aerosol extinctions using the same BB emissions (GFED3). A similarity in emission inputs amongst the models makes the interpretations of model diversity in simulating vertical distributions of aerosols solely dependent on aerosol processing and transport. All the models were run for the complete year of 2008, of which we have used the data for only the peak BB months of August and September [*Abel et al.*, 2005]. The models considered in our study (Table 4.1) include atmospheric GCMs that used either MERRA (GEOS5-GOCART) or ERA-Interim reanalysis dataset (CAM5, HadGEM3, ECHAM6-SALSA) to replay or constrain the model simulated meteorological fields, and an offline CTM (GEOS-CHEM) that was driven using assimilated meteorological fields from GEOS-5 (GEOS5-GMAO). Different emission injection height assumptions and moist convection schemes were used for different models, which are mentioned in Table 4.1. The table also lists other useful information about the configurations that models used to generate the simulations used in our study. The representation of aerosol dry and wet removal processes across the models is quite varied. The details about how each model treats these processes can be found in the references listed in Table 4.1 for the respective models.

Table 4.1 Models used in this study and general information about their configuration

Model	**CAM5**	**HadGEM3**	**ECHAM6-SALSA**	**GEOS-CHEM**	**GEOS5-GOCART**
Operating Institution	PNNL/UWyo	Met Office, UK	Finnish Met. Institute	Univ. of L'Aquila, Italy; University of Athens, Greece	NASA GSFC
Type	Atmospheric GCM	Atmospheric GCM	Atmospheric GCM	Offline CTM	Atmospheric GCM
Horizontal Res. (Lat × Lon)	1.9 × 2.5	1.25 × 1.875	1.9 × 1.9	4 × 5	1 × 1.25
Vertical Levels	30 (to 3.6 hPa)	85 (to 0.01 hPa)	31 (to 10 hPa)	72 (to 0.01 hPa)	72 (to 0.01 hPa)
Meteorological Fields	ERA-Interim	ERA-Interim	ERA-Interim	GEOS5-GMAO	MERRA
Injection Heights for BB emissions	Uniformly mixed within 1 km above surface	Evenly distributed within 0-3 km	Between 0-6 km [a]	Uniformly mixed within model calculated PBL	Uniformly mixed within model calculated PBL

Table 4.1 continued

Moist Convection Scheme		Shallow: *Park and Bretherton* [2009] Deep: *Zhang and McFarlane* [1995]	*Gregory and Rowntree* [1990]; *Darbyshire et al.* [2011]	*Tiedtke* [1989] - *Nordeng* [1994]	RAS [*Moorthi and Suarez*, 1992]	RAS [*Moorthi and Suarez*, 1992]
Aerosol mixing state		Internally mixed [b]	Internally mixed [c]	Externally mixed	Externally mixed	Externally mixed
BB aerosol refractive index (550 nm)	BC	1.95+0.79i	1.75+0.44i	1.85+0.71i	1.75+0.45i	1.75+0.44i
	OC	1.53+0.006i	1.5+0i	1.53+0.006i	1.53+0.006i	1.53+0.006i
Basic Reference		*Liu et al.* [2012]	*Johnson et al.* [2016]	*Stevens et al*. [2013]	*Bey et al.* [2001]	*Colarco et al.* [2010]

[a] BB emissions are distributed in 6 layers extending from the surface to 6 km following *Dentener et al.* [2006]. [b] Internal mixing for particles within the same size mode and external mixing for particles across the modes (Aitken, accumulation, coarse); carbonaceous aerosols are all in the accumulation mode. [c] Internal mixing within 5 size modes (nucleation, Aitken insoluble, Aitken soluble, accumulation soluble, coarse soluble).

4.2 Results and Discussion

4.2.1 Aerosol Plume Transport

Contours of meridional mean smoke aerosol extinctions along the longitude height cross-sections (Fig. 4.1-3) illustrate the transport and transformation of the aerosol plume from land to the ocean. The GEOS-5 simulated extinctions here are based on GFED3 BB emissions, same as that for other models to make the inter-model comparisons equitable. The CALIOP retrieved mean cloud top heights (in blue) are superimposed over the filled contours of aerosol extinctions to understand the variations in relative altitude of cloud tops with respect to smoke layers. The figures 4.1-3 are accompanied by Table 4.2 that contains the mean AOD between 2-4 km ASL (AOD_{2-4}) from CALIOP and the models averaged over three 10-degree longitude-by-latitude boxes, wherein each box represents a different stage of smoke plume in the direction of its transport. The first latitude-longitude row (or box) for each sub-region refers to the land region adjacent to the ocean (20°-10°E). The second row refers to the oceanic region adjacent to the continent (10°E-0°) and the third row refers to the oceanic region farther off-shore (0°-10°W). Vertical levels in between 2-4 km were chosen for calculating the mean AOD because CALIOP cannot measure aerosol below cloud levels and maximum cloud top heights occur at ~2 km over the ocean. Since most models considered in this study used MERRA and ERA-Interim wind fields, the horizontal wind streamlines (Fig. 4.4) and vertical pressure velocities (Fig. 4.5) from the two datasets were obtained to understand the observed similarities or differences in the horizontal and vertical transport of aerosol plumes amongst the models due to large-scale motion. Since CALIOP data in our study is the mean over 2007-2009 and the model results are for 2008 only, we also compared the MERRA data for each of the three years to assess the representativeness of the year 2008 in terms of the transport pattern over our domain. The results (not shown here) showed very low inter-annual variability in the directions of wind streamlines and magnitudes of wind speeds and vertical pressure velocities. In addition, the horizontal wind fields from MERRA and ERA-Interim were quite similar, so only the MERRA wind streamlines are depicted in Figure 4.4 to avoid redundancy.

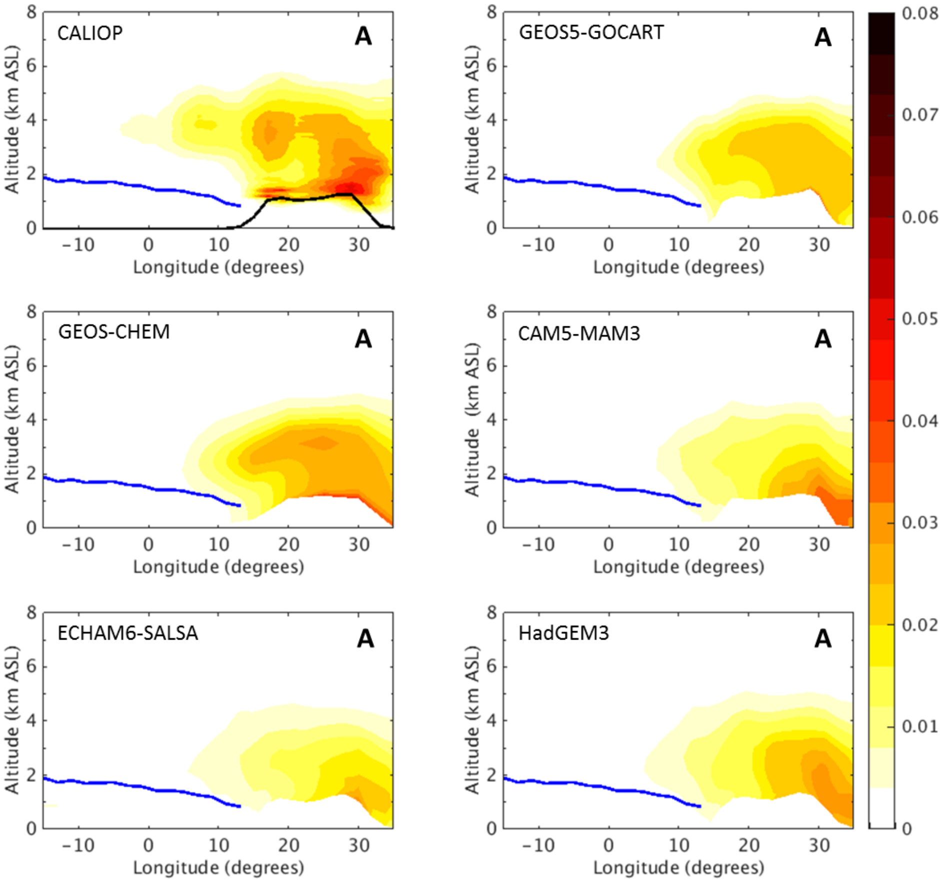

Figure 4.1 Meridional average of smoke aerosol extinction coefficients (km-1) over sub-region A (30°-20°S, 35°E-15°W) from CALIOP, GEOS5-GOCART and four AeroCom models (GEOS-CHEM, CAM5, ECHAM6-SALSA, HadGEM3). CALIOP-retrieved mean cloud top heights are overlaid (in blue solid line) on all the panels for the oceanic parts of the domain. The black solid line on the CALIOP panel depicts the mean surface elevation measured by the lidar signal. Note that all models used the GFED3 BB emission inventory and model averages are for Aug-Sep 2008, while CALIOP averages are for Aug-Sep 2007-2009.

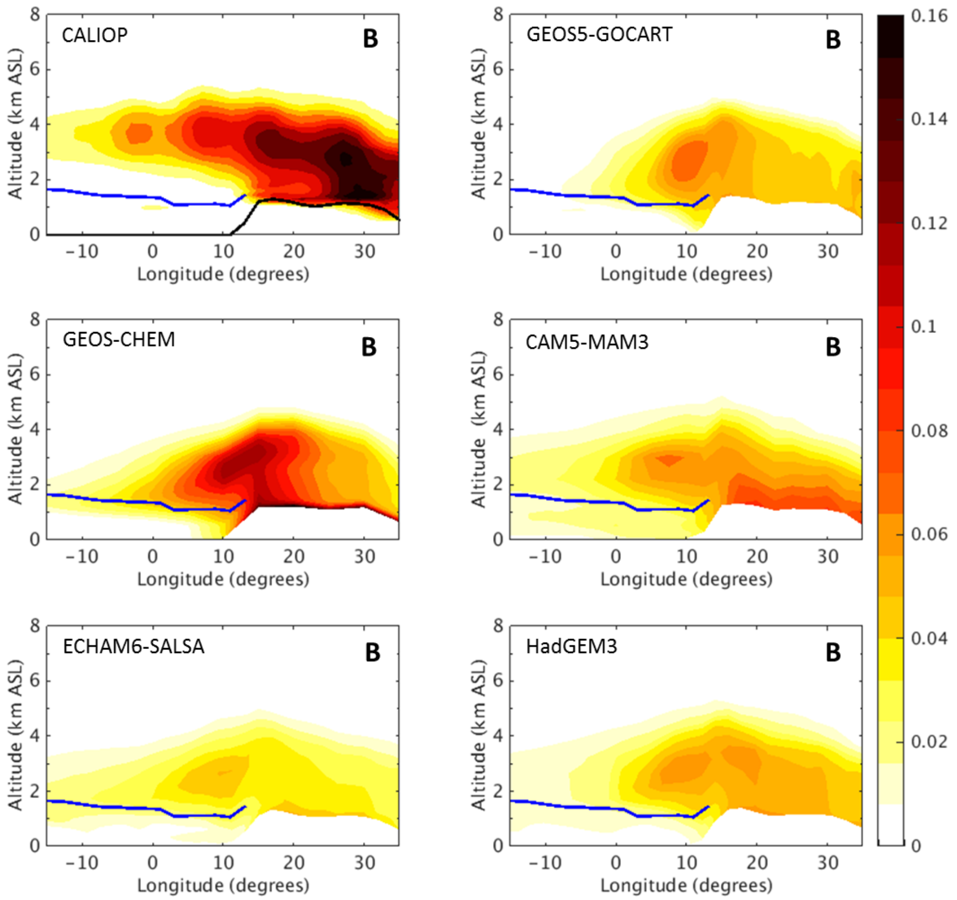

Figure 4.2 Same as Figure 4.1 but over sub-region B (20°-10°S, 35°E-15°W).

Some transport features are common to all the three sub-regions of the domain. For example, the maximum heights up to which the smoke aerosol plumes get lofted over land (~ 3.5 to 4.5 km above ground elevation) are well captured by all the models when compared to CALIOP observations (Fig 4.1-3), irrespective of the differences in emission injection heights assumptions amongst them (Table 4.1). This may be attributed to the strong uplifting over land surfaces (Fig. 4.5) in the models. More importantly, CALIOP observed smoke aerosol plumes transition from land to the ocean only at elevated levels above the MBL and maintain the peak of the smoke extinction profiles in between 3 to 4 km ASL throughout their course of transport over the ocean. This behavior of CALIOP aerosol plumes can be correlated with the directions and magnitudes of the horizontal winds in the region (Fig. 4.4). The easterlies directed from the polluted air mass over land prevail at altitudes greater than or equal to 2 km (~ 800 hPa). At levels below 2 km, the winds over the ocean are directed from the southeast, where clean maritime air masses reside. Also, strong wind speeds across the land-ocean boundary seem to exist between 700 to 600 hPa (3-4 km ASL), with wind speed maxima of ~ 7-8 m/s occurring around 650 hPa. In contrast to CALIOP observations, model simulated aerosol plumes rapidly descend to lower levels over the ocean relative to the heights up to which they were lofted over land. This may be attributed to the strong downward motion over the ocean in the models (Fig. 4.5), causing the aerosol plumes to experience a sudden subsidence as they transition from land to the ocean. However, the levels to which the aerosol plumes get subsided and the steepness of this aerosol descent vary amongst the models and amongst the different sub-regions in the domain as well.

In sub-region A (Fig. 4.1), high extinction values near the land surface occurring between 30°-35°E in all the model and CALIOP sub-plots represent BB sources along the east coast of the continent (Fig. 1.1, 2.1b). However, only a small fraction of the smoke aerosols originating from this source makes it to the west coast across the Namib Desert and further into the Atlantic Ocean, also depicted by the near-zero values in the third row of Table 4.2 for sub-region A. This is because the horizontal winds in this region deflect the westward travelling smoke plumes towards the southeast direction (Fig. 4.4c and d). For the aerosol particles that do reach the Atlantic though, their descent to the lower levels across the land-ocean boundary is not very drastic in the models and aerosol plumes manage to stay well above the observed cloud levels during their further transport.

Over land in sub-region B (Fig. 4.2), discrepancies in the spatial locations of the intense burning sources between the model simulations and CALIOP observations are evident. The locations of intense burning sources can be recognized in the contour plots when very high smoke extinction values compared to its neighboring regions occur at levels near the land surfaces and continue up to the levels to which smoke plumes are lofted. For example, it can be clearly seen that plumes start from a band between 30°-20°E in CALIOP observations, while in all the models, except CAM5, the elevated plumes are visible only near 20°E. Recall our previous discussion in section 3.3.1 about the missing area of very high AOD values in GEOS-5 around the same locations. One of the probable reasons could be weak uplifting in the models near 30°E (Fig. 4.5), but strong horizontal winds directed northwards just above the land surface (800 and 850 hPa in Fig. 4.4) in this area. The weak uplifting in CAM5 though, may partly be compensated by the strong convective mass fluxes occurring around the same region, shown in Fig. 5.3 in Chapter 5.

Over the ocean in sub-region B, simulated aerosol transport in GEOS-5 and GEOS-CHEM is characterized by a sharp descent of aerosol plumes from ~4-5 km ASL down to the levels near the observed cloud tops, noticeably between 12°-0°E (Fig. 4.2). However, for models using ERA-Interim wind fields (CAM5, ECHAM6 and HadGEM3), the slope of this descent is not so steep. This is also reflected in the AOD2-4 gradient between the first and second row of Table 4.2 (~ 50% decrease for GEOS-5 and GEOS-CHEM as opposed to only ~10-15% decrease for the other models). During further transport of smoke plumes from the coast to the deeper parts of the ocean, CAM5 stands out compared to the other models with respect to maintaining the peak of smoke extinctions at 2-3 km ASL (compared to 3-4 km ASL for CALIOP smoke) and having the highest AOD2-4 between 0-10°W compared to the other models (Table 4.2). Another characteristic difference between CALIOP retrievals and the model simulations in this sub-region lies in the estimation of magnitudes of aerosol extinctions. Simulated smoke extinctions by all the models except GEOS-CHEM, are lower by a factor of 2 or more compared to CALIOP extinctions, even though all the models used the same BB emissions input from GFED3 (see the first row for sub-region B in Table 4.2 and Fig. 4.2). This anomalous behavior of GEOS-CHEM could possibly be a resultant effect of the following factors. GEOS-CHEM has a much coarser horizontal resolution compared to other models (Table 4.1), which can affect its simulation of vertical processes [Protonotariou et al., 2010]. Differences in assumptions of aerosol optical properties and size distributions can also cause substantial differences in estimation of aerosol extinctions [Curci et al., 2014]. Further investigation into the relative contribution of each of these factors in causing this strikingly different extinction magnitudes simulated by GEOS-CHEM is beyond the scope of this study.

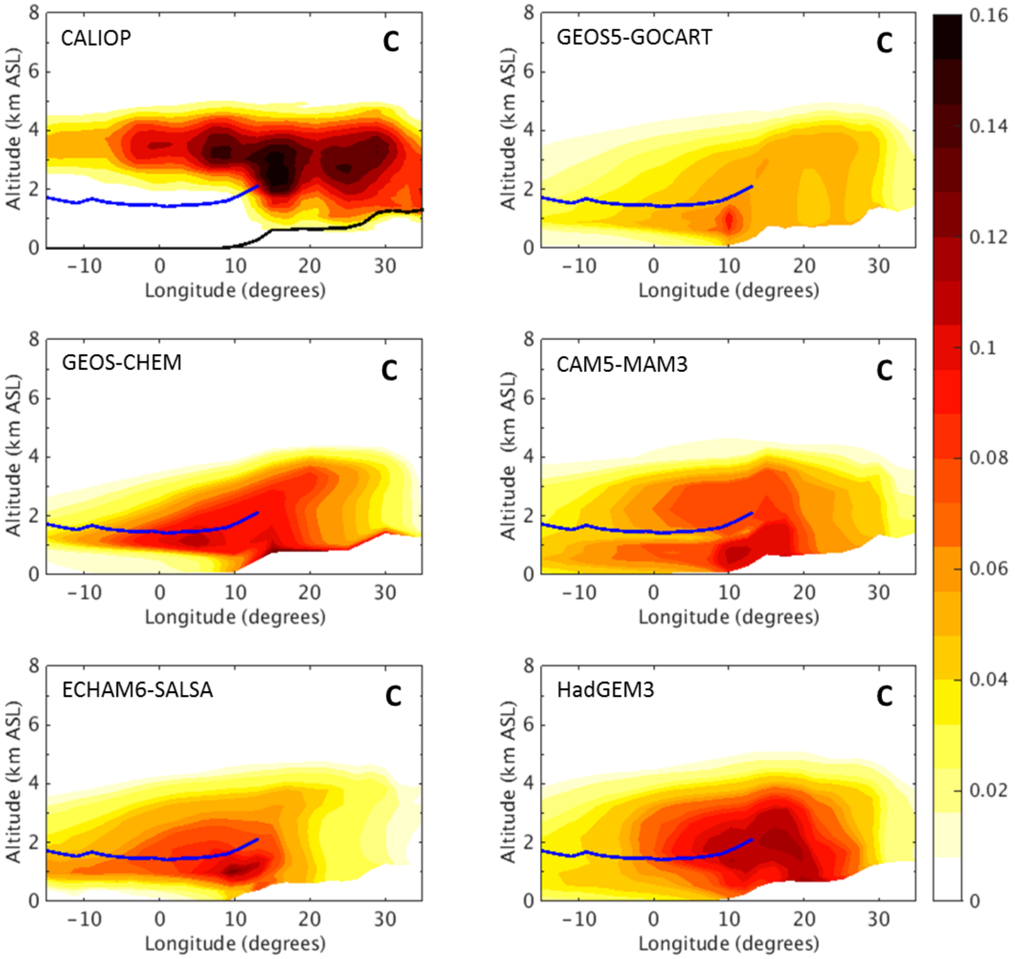

Figure 4.3 Same as Figure 4.1 but over sub-region C (10°S-0°, 35°E-15°W).

In sub-region C (Fig. 4.3), the plume transport features are quite varied amongst the models. The surface elevation at the coasts (~ 0.5 km ASL) here are much lower than the layer top heights of the clouds (~ 2 km ASL) residing along the coasts. So, there is a high possibility that smoke aerosol originating from the burning areas near the coast get advected into or below the clouds. Since CALIOP cannot detect aerosol below the cloud layers, it is not possible to estimate the fraction of smoke aerosol occurring below the cloud levels compared to the fraction of smoke aerosols occurring above the clouds. Previous studies [*Costantino and Bréon,* 2013; *Painemal et al.,* 2014] have also found evidence of large microphysical changes in the clouds over this sub-region (mainly north of 5°S) owing to the presence of aerosols within the clouds. CALIOP observes a thick smoke layer above the clouds with a narrower 'clean air' gap between the smoke and cloud layers compared to the other parts of the domain, but with the peak smoke extinctions still occurring between 3-4 km ASL. Amongst models, the ones using ERA-Interim meteorological fields (CAM5, ECHAM6 and HadGEM3) are able to keep a substantial amount of aerosol above the observed cloud tops over the ocean, resulting in simulated AOD_{2-4} values to be ~65-85% of CALIOP observed AOD_{2-4} values for both near and farther off-shore areas (Fig. 4.3 and Table 4.2). For GEOS-5 and GEOS-CHEM however, the bulk of the aerosol layer over the ocean stays much lower compared to CALIOP, especially farther off-shore between 0-10°W, where AOD_{2-4} for both the models is merely ~30% of the CALIOP observed AOD_{2-4} value of 0.12 (Table 4.2). This may be partly attributed to the differences in vertical velocities between MERRA and ERA-Interim for this sub-region. The subsidence over the ocean in MERRA is much stronger (~30-40 hPa/day) than that of ERA-Interim (~10-20 hPa/day) here (Fig. 4.5).

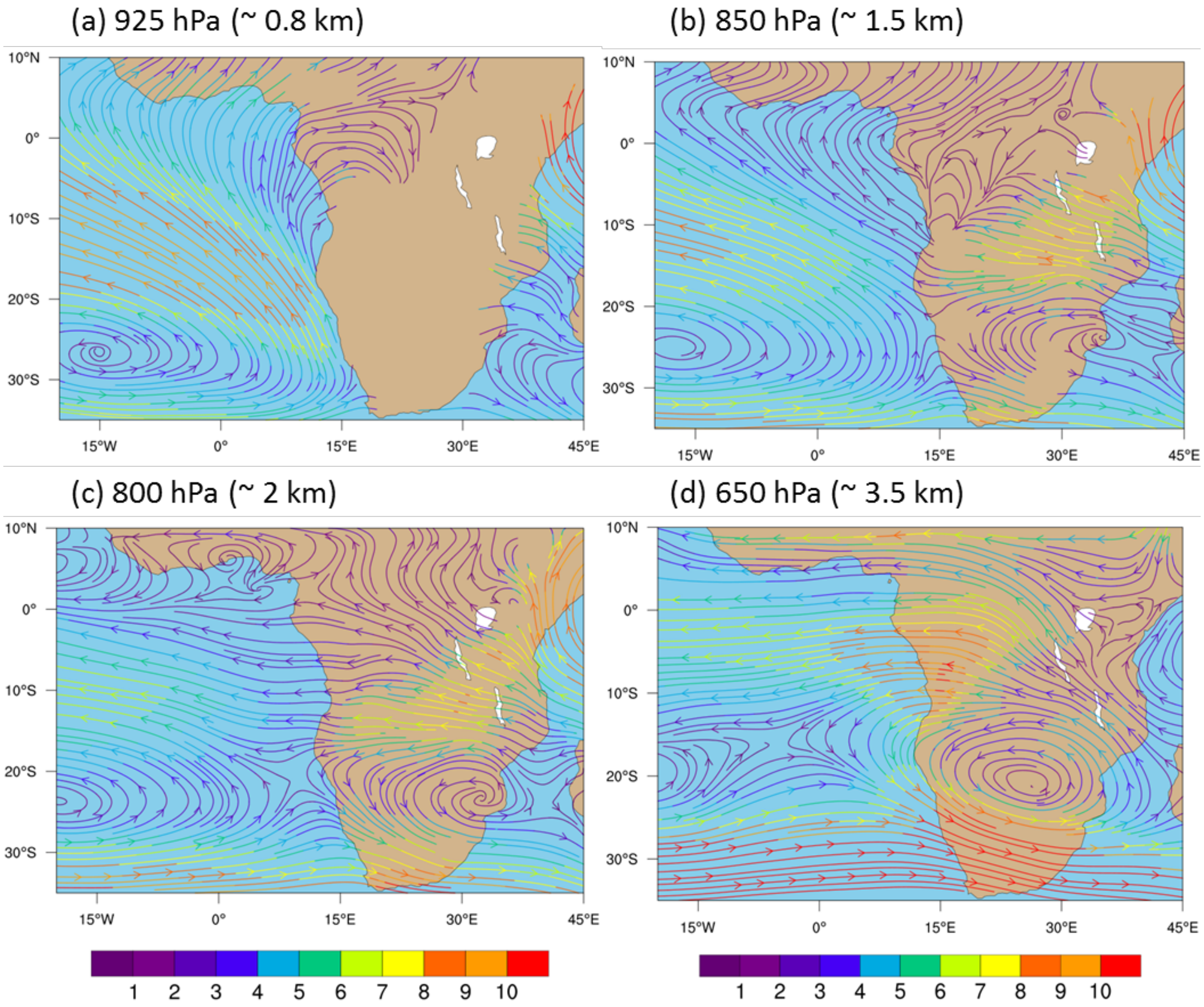

(a) 925 hPa (~ 0.8 km)

(b) 850 hPa (~ 1.5 km)

(c) 800 hPa (~ 2 km)

(d) 650 hPa (~ 3.5 km)

Figure 4.4 Horizontal wind streamlines over the domain at significant pressure levels, retrieved from MERRA reanalysis data and averaged over Aug-Sep 2008. The streamlines are colored by the wind speeds in m/s.

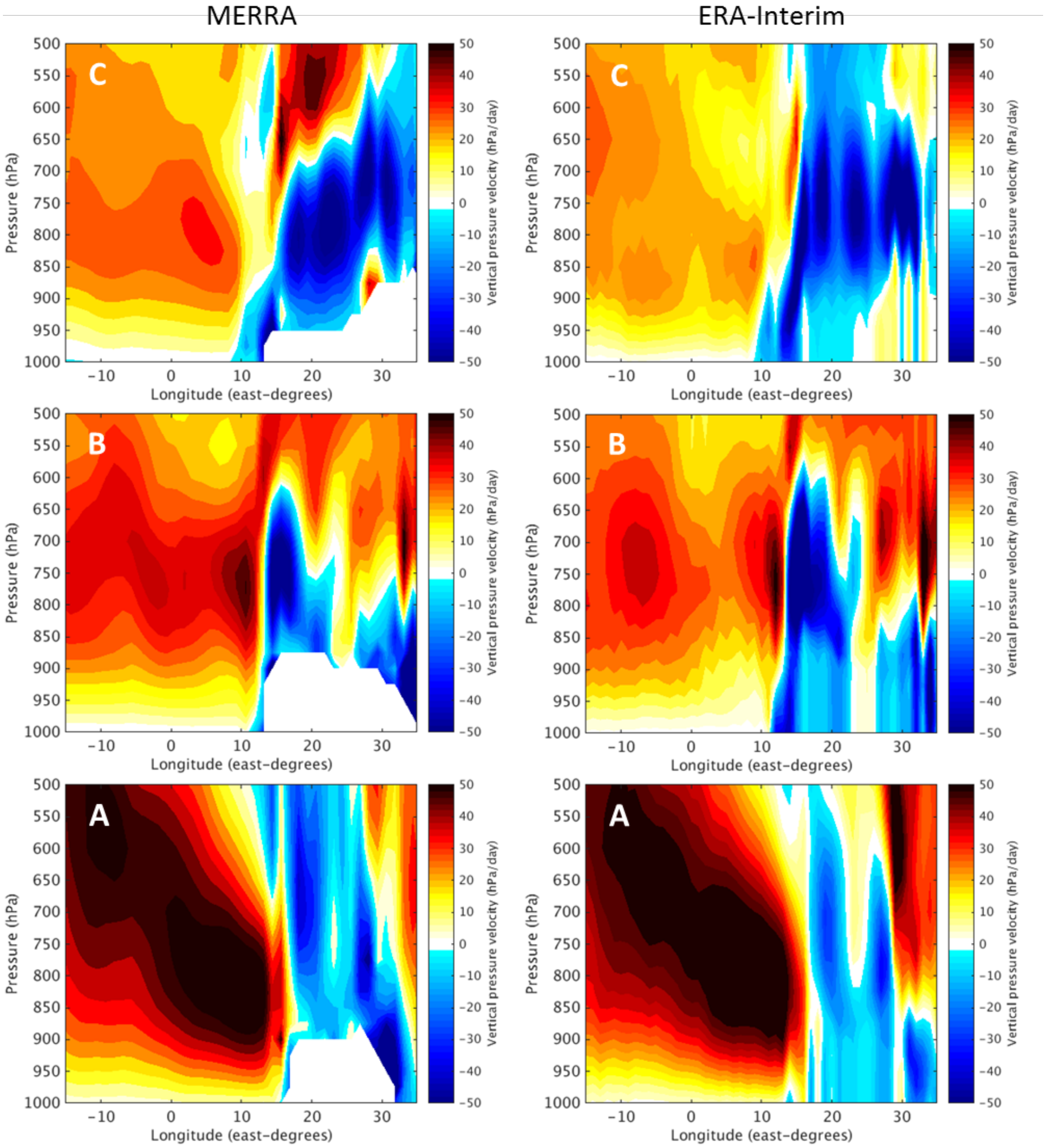

Figure 4.5 Vertical pressure velocities (hPa/day) during Aug-Sep 2008 from MERRA (left) and ERA-Interim (right) reanalysis data over the three sub-regions of the domain. Warmer colors signify downward motion while cooler colors signify upward motion.

Table 4.2 Mean aerosol optical depth between 2-4 km above sea level (AOD_{2-4}) from models and CALIOP averaged over three 10-degree longitude-by-latitude boxes in the direction of aerosol plume transport for each sub-region.

Sub-regions		**CALIOP**	**GEOS-5**	**GEOS-CHEM**	**CAM5**	**ECHAM6**	**HadGEM3**
A (30°-20°S)	(20°E-10°E)	0.04	0.04	0.04	0.02	0.02	0.02
	(10°E-0°)	0.02	0.01	0.01	0.01	0.01	0.01
	(0°-10°W)	0.01	0.00	0.00	0.00	0.00	0.00
B (20°-10°S)	(20°E-10°E)	0.22	0.12	0.20	0.11	0.08	0.11
	(10°E-0°)	0.13	0.06	0.10	0.10	0.07	0.09
	(0°-10°W)	0.08	0.02	0.03	0.05	0.03	0.04
C (10°-0°S)	(20°E-10°E)	0.27	0.10	0.14	0.14	0.11	0.19
	(10°E-0°)	0.19	0.07	0.08	0.12	0.12	0.16
	(0°-10°W)	0.12	0.04	0.04	0.08	0.08	0.10

4.2.2 CALIOP Measurement Biases

Although we compared the model simulations with CALIOP observations to evaluate the smoke plume transport in the models, we are also aware of the algorithm biases of CALIOP (see Chapter 2) that should be discussed in the context of our region of interest to explain some of the discrepancies in the spatial locations of aerosol between the model simulations and CALIOP observations. For example, large extinction values due to intense burning sources near the coasts around 20°E (Fig. 1.1, 2.1a) in sub-region B are captured by all the models in Figure 4.1-3, but is less prominent in CALIOP observations. This shortcoming of CALIOP retrievals can be attributed to substantial attenuation of the lidar signal by optically thick aerosol layers existing above the burning sources.

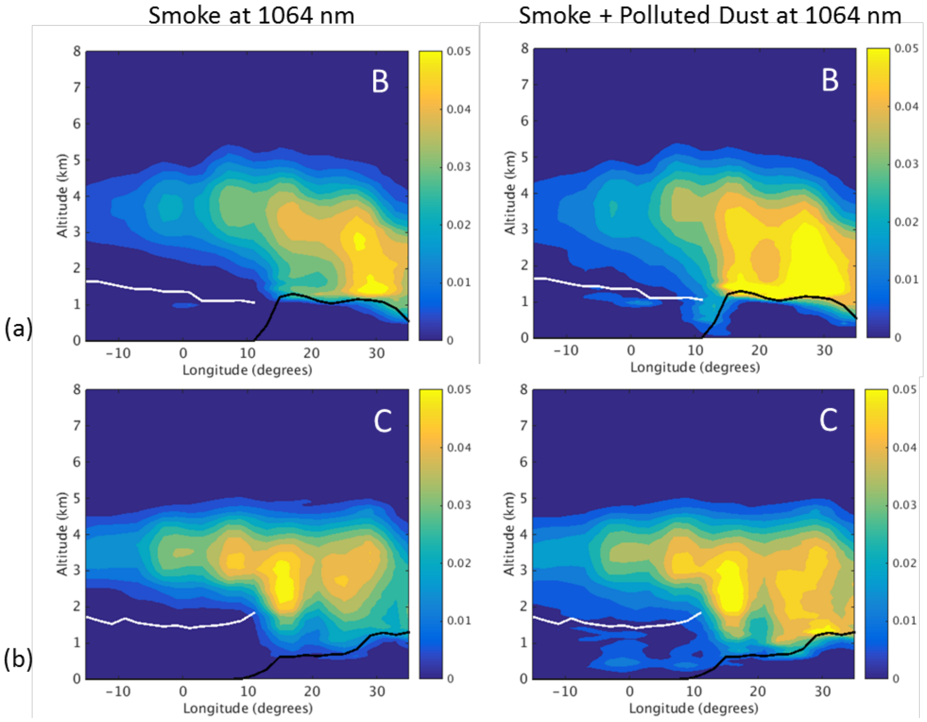

Figure 4.6 Comparison of CALIOP classified (left) smoke and (right) smoke plus polluted dust aerosol extinction coefficients (km^{-1}) at 1064 nm over sub-regions (a) B (20°S-10°S, 35°E-15°W) and (b) C (10°S-0°, 35°E-15°W). CALIOP retrieved mean cloud top heights are superimposed in white over the ocean.

To further examine the extent of aerosol type misclassification by CALIOP specific to our domain, we compared the CALIOP retrieved aerosol extinctions at 1064 nm for two cases: (i) extinction measurements with only the smoke aerosol flag and (ii) extinction measurements with both smoke and polluted dust aerosol flags. The results are shown for sub-regions B and C (Fig. 4.6), where the majority of BB occurs. For sub-region B (Fig. 4.6a), the intense burning sources around 20°E (as discussed earlier) are now apparent in CALIOP extinction contours for combined smoke and polluted dust case. For sub-region C however, low surface elevations near the coast cause the lidar signal to get completely attenuated before reaching the bottom of the optically thick smoke plumes. Thus, high extinction values around 15°E (Fig. 4.6b) end abruptly a few hundred meters above the ground even after considering smoke and polluted dust together. Over the ocean for both sub-regions B and C, the thickness of the aerosol above cloud layer is enhanced towards the bottom of the aerosol layers when smoke and polluted dust extinctions are combined as opposed to only smoke. This again appears to be a consequence of signal attenuation because even though southern Africa has a large area of arid terrain, dust from these sources do not get readily mobilized by the typical meteorology of the area [*Liu et al.,* 2015; *Washington et al.,* 2003]. However, it is interesting to note that the highest extinction values over the ocean in CALIOP still occur at levels between 3-4 km irrespective of the inclusion or exclusion of polluted dust type with smoke.

CHAPTER 5. TRANSPORT PROCESSES AFFECTING AEROSOL VERTICAL DISTRIBUTION

It is clear from the previous discussions that the major differences between GEOS-5 and CALIOP smoke aerosol vertical distribution during the long-range transport of smoke plumes occur over the oceanic parts of the domain. To assess whether this model behavior persists in the aerosol reanalysis product of GEOS-5, MERRAero [*Buchard et al.,* 2015], we obtained the BB aerosol mass concentrations available from sources listed at https://gmao.gsfc.nasa.gov/reanalysis/merra/MERRAero/data/ for the time-period and domain of our study. We found that the tendency of GEOS-5 smoke aerosol to rapidly descend towards the cloud tops off the coast and up to ~0°W persists in the MERRAero simulations as well (Fig. 5.1). This indicates that assimilation of observed column AOD into the model is unable to resolve the inconsistencies between GEOS-5 and CALIOP observed aerosol vertical structure in this context. Out of the several aerosol-related processes listed in section 1 of Chapter 3 that could influence the vertical distribution of aerosol in a model, we may rule out the emission injection height treatment in GEOS-5 as a probable cause of observed differences because the simulated plume heights over land in all the models matched well with those from CALIOP. Similarly, inaccuracies in representation of emission source strength and physical aging of carbonaceous aerosol might alter the magnitudes of extinction profiles but cannot possibly explain the displacement of the peaks in the model extinction profiles to lower levels relative to CALIOP during the smoke plume transport over the ocean. Thus, investigations into the model representation of aerosol removal processes and convective transport are more relevant to the context of this study.

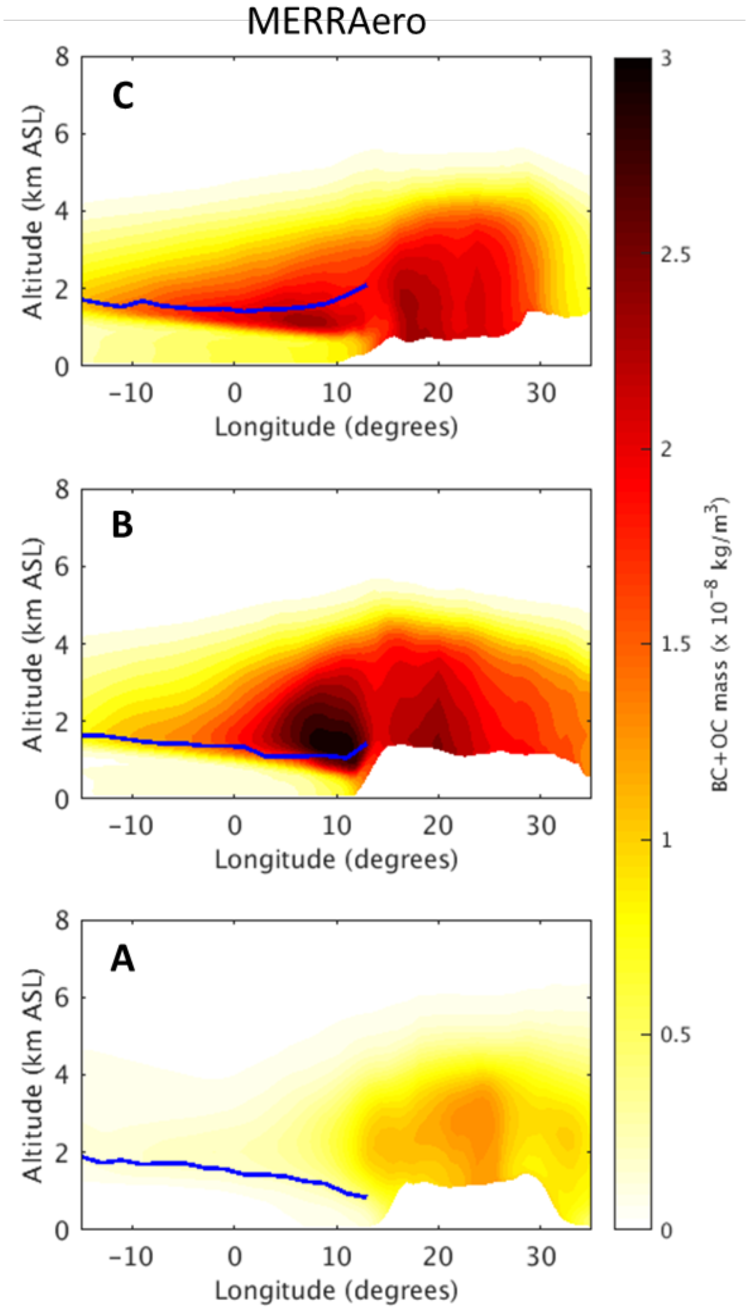

Figure 5.1 Meridional mean MERRAero smoke (BC+OC) aerosol mass concentrations (× 10^{-8} kg m^{-3}) averaged over Aug-Sep 2008 for the three sub-regions of the domain. CALIOP-retrieved mean cloud top heights are superimposed in blue over the ocean.

5.1 Aerosol Removal

Excessive removal of aerosol particles via gravitational settling or dry and wet depositions at levels of their predominant occurrence can cause a shift in the peak of extinction profiles during the transport of aerosol plumes. As discussed previously in Chapter 3, CO can be a good tracer to test this hypothesis because CO and carbonaceous aerosol both have the same emission sources but unlike aerosol, CO does not get subjected to dry and wet depositions. In fact, Keil and Haywood, (2003) observed the similarity in shape of the CO and aerosol vertical profiles retrieved from in-situ measurements over the oceanic areas off the Namibian and Angolan coast during the SAFARI-2000 campaign. Towards this end, we compare the simulations of aerosol and CO transport from GEOS-5 using contours of smoke aerosol mass concentrations and CO mixing ratios respectively (Fig. 5.2). The BB emissions for both aerosol and CO here are based on the QFED2 inventory. There is profound similarity in the transport pattern of simulated smoke aerosol and CO plumes for most parts of the domain, suggesting a minimal role of aerosol removal processes in the observed discrepancies between the model and satellite measurements. The differences in the extents (both vertically and horizontally) to which CO gets transported compared to aerosols can be attributed to the longer lifetimes of CO (in the order of months) relative to the aerosols (~ a week) [*Bian et al.,* 2013; *Ford and Heald,* 2012].

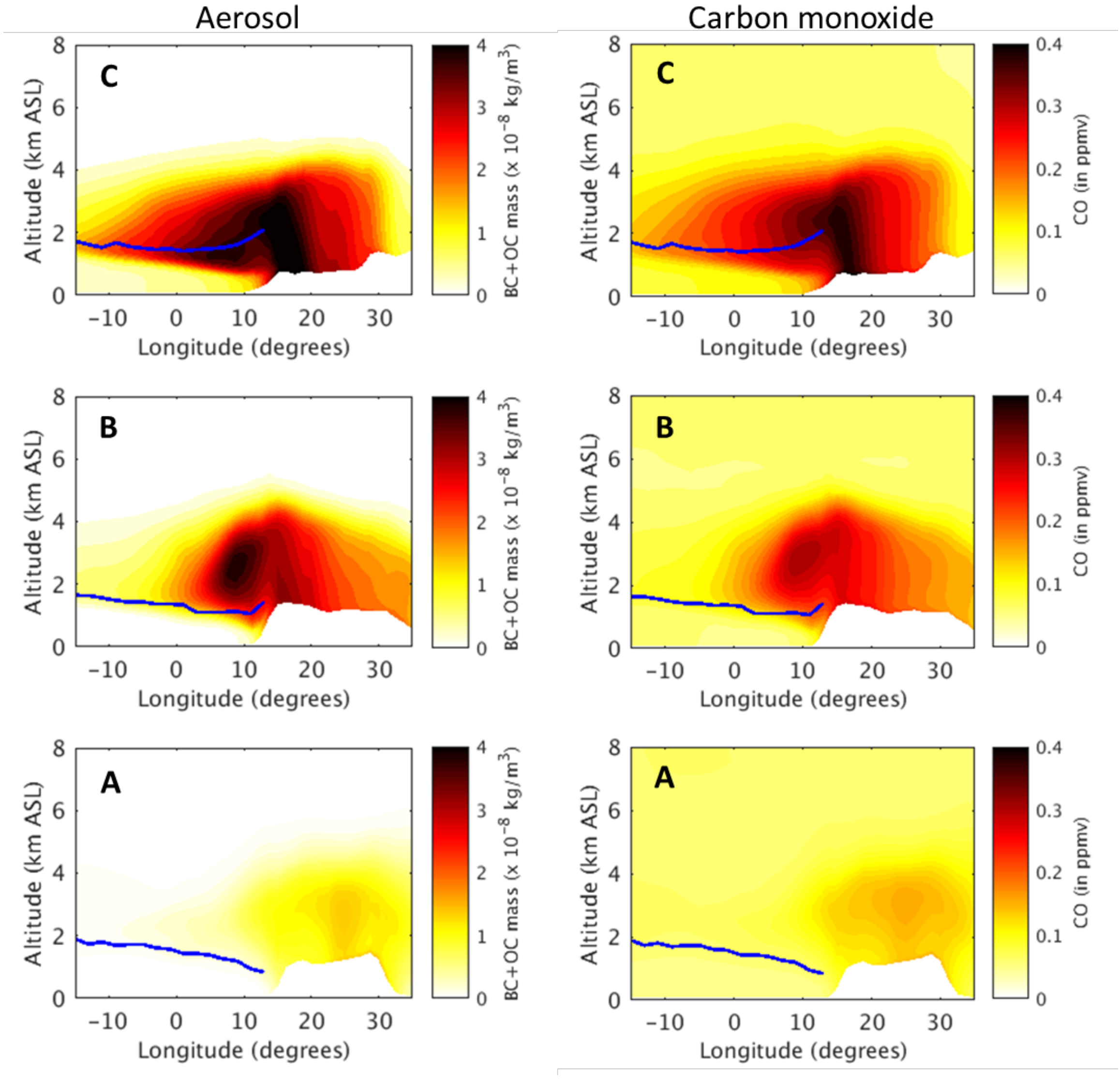

Figure 5.2 Contours of mean (left) smoke aerosol mass concentrations (× 10^{-8} kg m^{-3}) and (right) carbon monoxide (CO) mixing ratios (ppmv) simulated by GEOS5-GOCART during Aug-Sep 2008 over the three sub-regions of the domain. CALIOP-retrieved cloud top heights are overlaid (in blue solid line) on all the sub-plots.

5.2 Convective Transport

Convection plays an important role in vertical transport and hence in the vertical distribution of aerosols and tracers in global models [*Allen and Landuyt*, 2014]. Convection occurs at a smaller spatial scale relative to the synoptic-scale processes and the typical resolution of global model grids [*Belikov et al.,* 2013]. Hence, shallow convection cannot be explicitly resolved, but is instead parameterized in such models using different schemes or algorithms (Table 4.1). Discussions in the results section of Chapter 4 suggested that the descending motion of smoke aerosols off the west coast was less rapid in CAM5 relative to GEOS-5 and other models in this study. Since the large-scale vertical motion seemed similar for both GEOS-5 and CAM5 over most parts of the domain except sub-region C (Fig. 4.5), we compared the amounts and locations of the upward convective motion within the models by considering the convective mass fluxes (CMFs) simulated by the two models (Fig. 5.3). The GEOS-5 simulated CMFs over the ocean are up to about an order of magnitude lower than CAM5 simulated CMFs. Further, strong CMFs over the ocean in CAM5 simulations extend up to the areas adjacent to the coast (5-10°E), while in GEOS-5, the strength of CMFs gradually diminish eastwards and are almost negligible beyond 5°E, especially for sub-regions B and C. The vertical extent of CMFs is also higher for CAM5 compared to GEOS-5. These contrasts in magnitudes and distribution of CMFs cause the difference in intensity of convective lofting of aerosol plumes and hence correspond to the differences in vertical location of the smoke aerosol layer between CAM5 and GEOS-5 over the ocean. However, magnitudes of simulated shallow CMFs over the ocean are most pronounced only up to ~850-800 hPa (~ 1.5-2 km), inferring that convective lofting in the models cannot counter the strong subsidence experienced by the aerosol layers in the models above these levels.

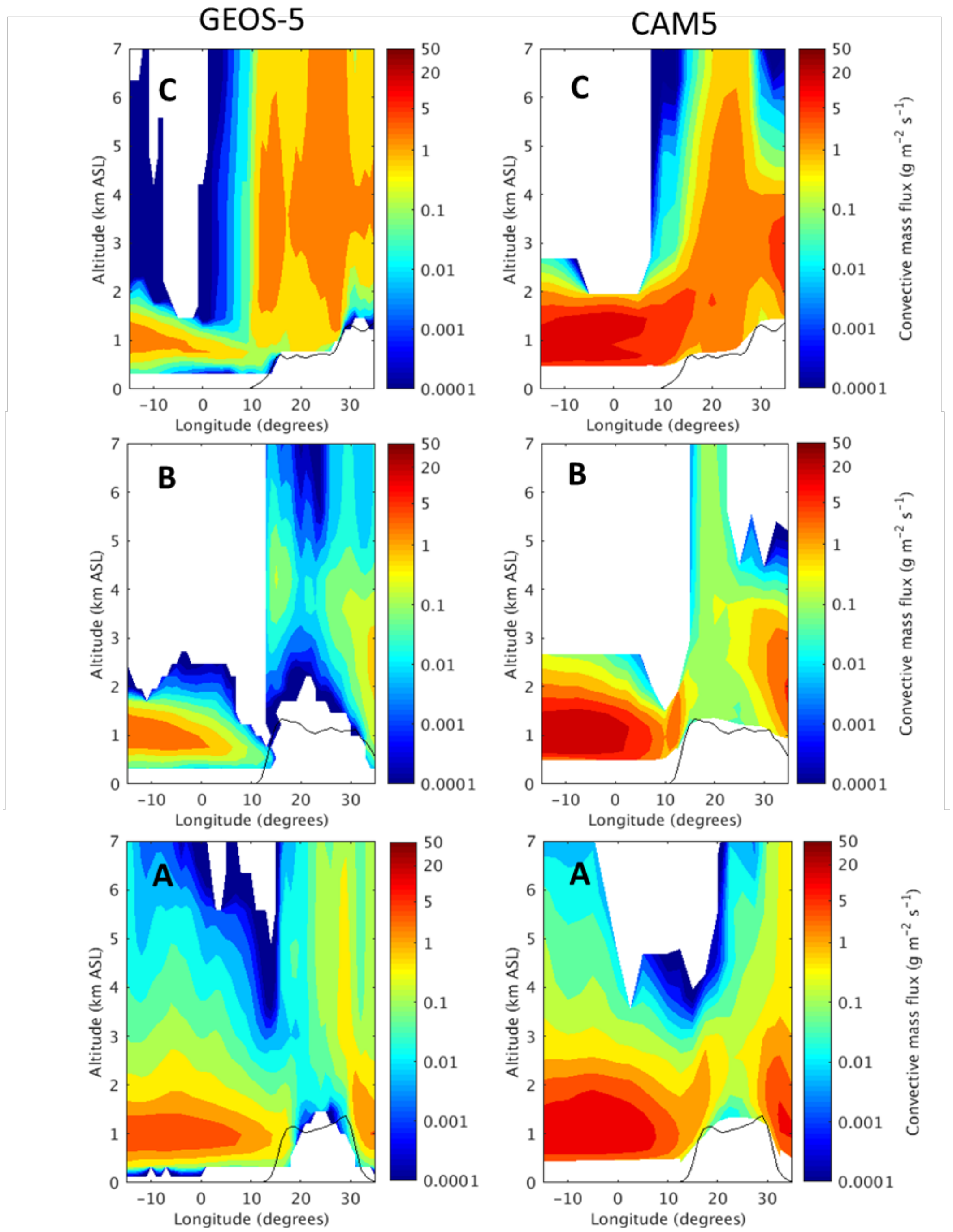

Figure 5.3 Comparison of convective mass flux (CMF, g m^{-2} s^{-1}) simulations by (left) GEOS-5 and (right) CAM5 during Aug-Sep 2008 over the three sub-regions of the domain. Note that the values are plotted on a log color scale to account for the large difference in magnitudes of the simulated fluxes between the two models.

5.3 Other factors

Previous studies over the SE Atlantic, like Sakaeda et al. (2011), have found that substantial changes (~20-30%) in model simulated large-scale vertical velocities can occur due to absorption of radiation at the levels of high BB aerosol loading, leading to a decrease in the model estimation of subsidence over the ocean. Similarly, Colarco et al. (2014) have found that stronger dust absorption in GEOS-5 can cause an increase in lofting of dust particles to higher altitudes during the transport of Saharan dust over the North Atlantic in the summer season. These examples indicate that inaccurate representation of aerosol absorption, which is very sensitive to the assumed single scattering albedo (ω_o), can also impact the simulation of large-scale vertical velocities and hence the vertical transport of aerosol in the model, owing to the aerosol-radiation feedback on the model atmosphere. The aerosol refractive index (at 550 nm) assumptions for models in Table 4.1 show that BC in CAM5 and ECHAM6 is very strongly absorbing relative to BC in other models. However, it is beyond the scope of our study to relate these differences in aerosol absorption amongst the models to the vertical transport of aerosol in the region. Thus, sensitivity studies to quantify the impact of aerosol absorption assumptions on the model simulated vertical velocities over the SE Atlantic are suggested.

Another evidence that supports the larger influence of the large-scale velocities in the model to cause the sharper descent of aerosol plumes across the land-ocean boundary is shown in Figure 5.4 below. GEOS-5 was run in two different modes over the same time-period of August and September 2008. One as a free-running GCM and second time in the replay mode, when wind and temperature fields in the model are adjusted every 6 hours using MERRA Reanalysis data.

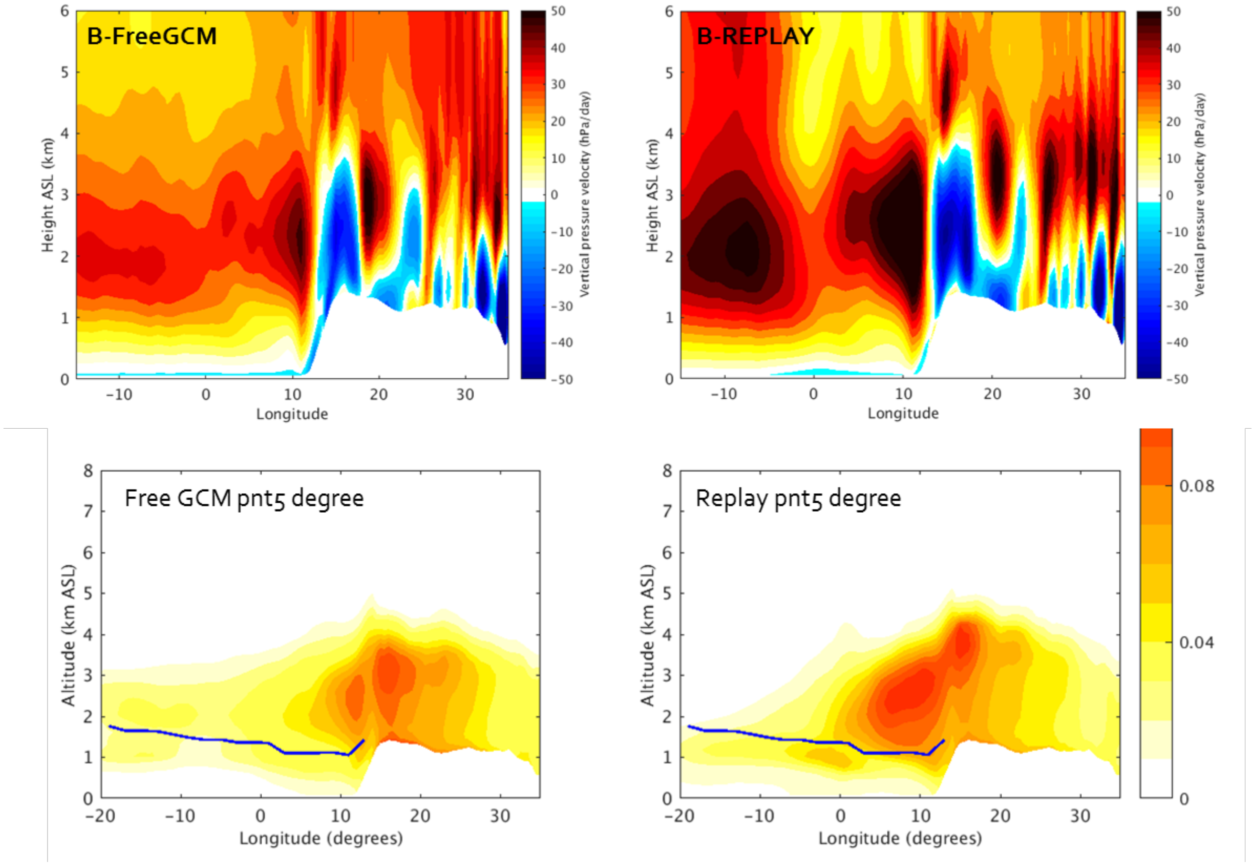

Figure 5.4 (Top) Vertical pressure velocities simulated by GEOS5-GOCART over sub-region B, when run in a free-running GCM mode (left) and in the replay mode using MERRA Reanalysis data (right). The corresponding aerosol extinction contours for each of the runs are depicted in the bottom panels. Blue solid lines on the bottom panels represent the CALIOP retrieved cloud-top heights.

Figure 5.4 above clearly shows that the large-scale subsidence just off the African west coast in the model is stronger in replay mode compared to when the model was run as a free-running GCM. This change appears to show effect on the aerosol plume transport as well because the descent of the aerosol plumes during their transition to ocean from the continent is steeper in in the replay mode compared to when the model was run as a free-running GCM using the same resolution, time-period and initial conditions.

CHAPTER 6. MODEL SENSITIVITY TO AEROSOL VERTICAL DISTRIBUTION

6.1 Introduction

When the smoke plumes emitted from the open BB in the southwestern African Savannah get transported over the south-east (SE) Atlantic during July to October every year, they disrupt the energy budget of the region via direct, indirect and semi-direct effects. These aerosol effects have been discussed in detail in Chapter 1. Observation-based estimates of direct radiative effects (DRE) of aerosol over SE Atlantic found that at the top of the atmosphere (TOA), DRE of BB aerosols for a given set of aerosol optical properties can be positive (radiative warming) or negative (radiative cooling), depending on the albedo and coverage of the underlying clouds [*Keil and Haywood*, 2003; *Chand et al.,* 2009; *Wilcox* 2012; *Zhang et al.,* 2016]. Chand et al. (2009) further quantified this theory by deriving a critical cloud area fraction of 40%, above which the warming effect of BB aerosols overpowers the cooling effect of the underlying clouds at TOA. For the modeling studies however, there is no consensus towards the sign or magnitude of the direct aerosol forcing over this region [*Schulz et al.,* 2006; *Myhre et al.,* 2013]. This is in part because of the differences in representation of stratocumulus clouds across models, which not only varies owing to their respective cloud schemes but are in general poorly simulated by the global models over this region [*Stier et al.,* 2013].

Studies on aerosol semi-direct effects over SE Atlantic found a negative radiative effect (cooling) at TOA in the presence of an aerosol layer above the cloud-topped marine boundary layer (MBL). The cooling effect is associated with an increase in low-level clouds [*Johnson et al.,* 2004; *Wilcox* 2010; *Sakaeda et al.* 2011]. The common mechanism used to explain the model cloud responses in these studies indicate that the increase in potential temperatures above the MBL due to aerosol SW heating at these levels leads to stabilization of the lower troposphere and strengthening of the inversion above cloud-tops. This further leads to a reduction in entrainment of dry air through the cloud-tops that acts to preserve greater amounts of moisture within the boundary layer. While Large-Eddy simulations (LES) of Johnson et al. (2004) found this mechanism to result in a shallower boundary layer with a substantial increase in cloud LWP by 5-10 g m^{-2}, Sakaeda et al. (2011) found this to cause an increase in the model low cloud cover according to Klein and Hartmann, (1993) with little or no effect on cloud LWP in their global atmospheric model (CAM3) coupled to a slab ocean.

Previous studies on aerosol-cloud interactions in general [*Penner et al.*, 2003; *McFarquhar and Wang*, 2006; *Koch and Del Genio*, 2010] have continually emphasized the crucial role of aerosol vertical distribution in the estimation of aerosol effects on clouds. To this end, recent LES based studies [e.g. *Yamaguchi et al.,* (2015) and *Zhou et al.,* (2017)] have attempted to test the model cloud responses to the variation in location of a fixed aerosol layer from within the MBL to above the MBL. These studies followed the idea of Johnson et al. (2004) but included the simulation of aerosol indirect effects as well. While Yamaguchi et al. (2015) found that the stratocumulus to cumulus transition (SCT) over SE Atlantic was delayed due the effects of an initially overlying layer of absorbing aerosols, Zhou et al. (2017) found that for a similar scenario, SCT was hastened. Although LES models have the advantage of explicitly treating the aerosol and cloud microphysical processes and their interactions, they are limited in their assumptions of idealized aerosol layers for model initial conditions and are unable to account for the changes in MBL properties arising from the aerosol-radiation feedback on large-scale atmospheric motions. Furthermore, since our previous discussions on BB aerosol transport in global models showed that the bulk of the modeled aerosol layers reside about 1-2 km lower than the CALIOP observations over the ocean, the consequent idea was to quantify the impact of such variations in aerosol vertical distribution on the model clouds. Therefore, the objective of this part of our study is to examine the changes in cloud and MBL properties owing to the changes in aerosol vertical distribution from the perspective of a global climate model like GEOS-5.

Some observational studies over SE Atlantic have also found estimates of aerosol indirect effects to be relevant, especially for areas farther downwind of BB sources and closer to equator (north of 5°S) [*Constantino and Bréon* 2013; *Painemal et al.,* 2015]. The current version of our model, however, does not simulate aerosol-cloud microphysical interactions, so we will only focus on the direct and semi-direct effects of aerosols. This part of the thesis is thus organized as follows: section 6.2 provides a description of the aerosol vertical redistribution methodology developed for this study, along with the brief description of the model experimental setup and processing of a newer version of CALIOP data. Section 6.3 discusses the results of the model experiments in the context of cloud responses to changes in aerosol vertical distribution and the estimation of direct radiative forcing of aerosols over SE Atlantic.

6.2 Approach and Methods

6.2.1 CALIOP Data Processing

For this part of the study, we have used the most recent Version 4.10 (V4) of CALIOP Level 2 Aerosol Profile product at 5-km horizontal resolution. Significant code, algorithm and data product changes have been made to V4 compared to the previous versions (V3). These are described in detail in the Data Quality Summary for the CALIPSO Version 4.10 Lidar Level 2 Data Products (available at https://www-calipso.larc.nasa.gov/resources/). The most relevant changes pertinent to our study lie in the improvements of aerosol subtyping for tropospheric aerosols. Mainly, the smoke layer identification and naming of aerosol sub-types have been revised. In short, as in previous versions, non-depolarizing aerosols at elevated levels are assumed to be smoke particles that are usually injected above the planetary boundary layer (PBL) due to combustion-induced buoyancy. The definition for "elevated" is revised in V4 to refer to layers with tops higher than 2.5 km above surface level, which is a simplistic approximation of PBL heights. Thus, the smoke aerosol subtype of V3 is changed to "elevated smoke" in V4. The introduction of a new algorithm in V4 to vertically homogenize aerosol subtyping for weakly scattering fringes detected at the base of extended plumes and the revision of the nomenclature for smoke aerosols is bound to correct the misclassification of elevated smoke aerosols as marine aerosols in previous versions. Within the PBL however, discrimination between smoke due to biomass burning and aerosols arising from anthropogenic pollution is difficult using CALIOP measurements. Therefore, the description of the polluted continental subtype is revised to "polluted continental/smoke" to account for such situations.

Further, the updates to the new aerosol sub-typing scheme claims to have greatly reduced the over-abundance of polluted dust identified in V3 [e.g. *Burton et al.,* 2013; *Das et al.,* 2017] by accounting for the signal attenuation due to overlying aerosol layers. Considering these updates in aerosol sub-typing and the aerosol misclassification bias observed in the CALIOP V3 product used in Chapters 3-5, for this work we decided to use the aerosol sub-types of 'elevated smoke', 'polluted continental/smoke', and 'polluted dust' together while averaging the CALIOP retrieved aerosol extinction profiles over the ocean. Therefore, we obtained a gridded product of CALIOP data by aggregating the 'smoke' aerosol extinction profiles at 532 nm for the peak BB months of August and September from 2006-2015 onto global 2° × 4° latitude-longitude grids. We chose to use only the nighttime retrievals of CALIOP as opposed to using both day and nighttime retrievals as previously.

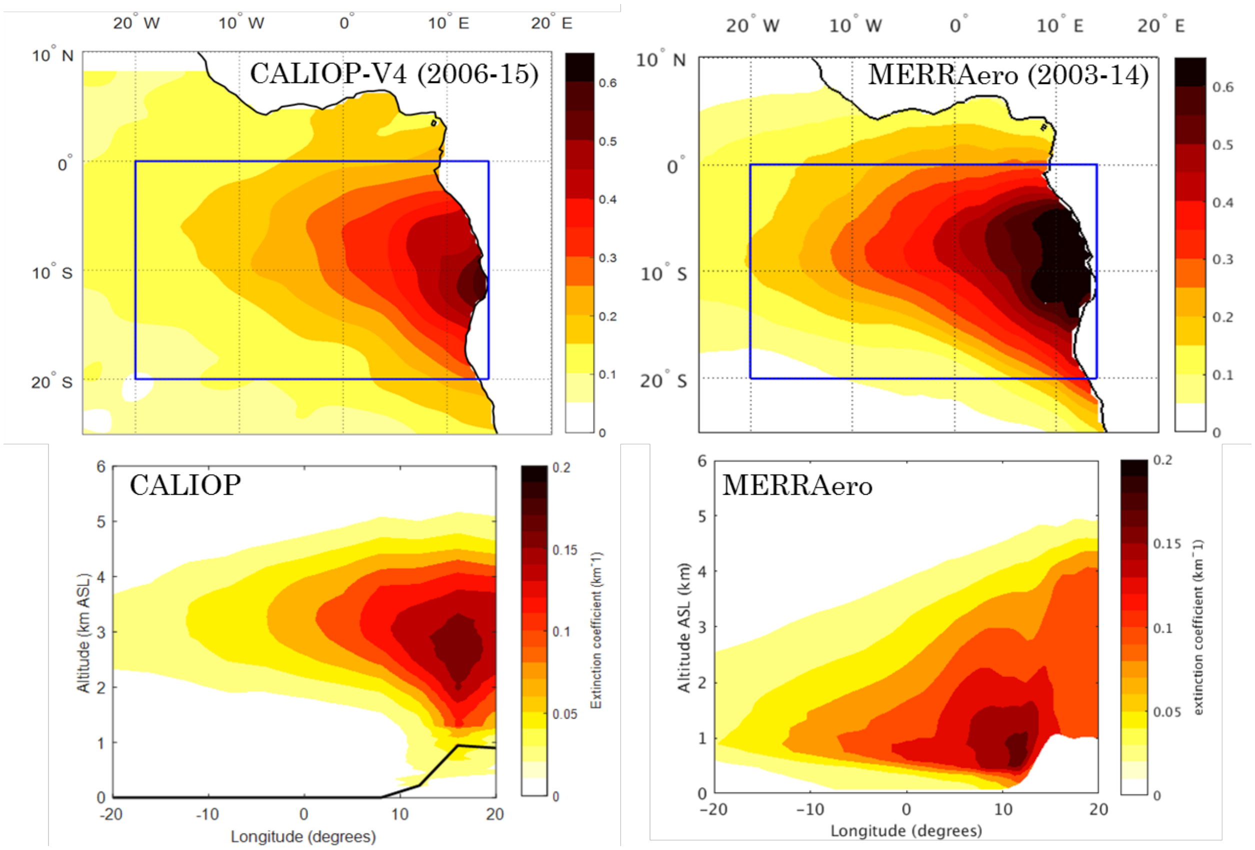

Figure 6.1 Aerosol climatology based on (left) CALIOP 532 nm retrievals of smoke aerosol, which in this study is combination of 'elevated smoke', 'polluted dust' and 'polluted continental' aerosol types. (Right) Aerosol climatology based on MERRAero. Top panels compare the horizontal distribution of smoke AOD, where the blue box depicts the extent of the domain chosen for aerosol redistribution. Bottom panels compare the vertical distribution of smoke aerosol from CALIOP and MERRAero using meridional cross-sections of aerosol extinctions averaged over the domain of interest (blue box).

Figure 6.1 above illustrates the horizontal and vertical distribution of smoke aerosol over our domain, marked by the blue box in the top panels. The climatology was obtained from the ten-year of CALIOP data at 532 nm after applying the data quality screening techniques described in

Chapter 2. For comparison, horizontal and vertical distribution of smoke ($BC+OC+SO_4$) extinctions and AOD from MERRAero are also placed alongside, which is the assimilated product of GEOS-5 model as described in the previous chapter. It is clear from the figure that although spatial distribution of smoke between CALIOP and MERRAero mostly agree in terms of both magnitudes and location, the vertical distribution over the ocean show major differences. The bulk of the MERRAero aerosols lay low compared to CALIOP by about 1-2 km, similar to the model results discussed in the previous chapters.

6.2.2 Aerosol Redistribution Methodology

We developed a methodology to utilize the long-term retrievals of aerosol properties by CALIOP to constrain the representation of aerosol vertical distribution in the model. The major assumption here is that aerosol mass profiles directly correspond to the aerosol extinction profiles in this region. Aerosol extinction is a complex function of aerosol mass and relative humidity (RH) in the model [*Randles et al.,* 2013]. However, since RH above the stratocumulus cloud-tops in the model is almost uniform and low, and the bulk of the aerosol mass lie above the clouds in this region, aerosol extinction can be directly related to aerosol mass as a close approximation to reality. Therefore, to redistribute the simulated aerosol mass profiles from the MERRAero climatology, we used the ten year (2006-2015) mean CALIOP gridded product of aerosol extinction obtained for this study. The redistribution methodology was applied to the grids falling within 0-20^{o}S and 20^{o}W-12^{o}E only because there needs to be substantial AOD in the CALIOP product to begin with for the redistribution of aerosol in the model to take place (Fig. 6.1). Moreover, we would also expect the effects of aerosol redistribution to be most pronounced for regions with substantial AOD. Thus, for each 4^o longitude by 2^o latitude grid of CALIOP product within this domain:

1. Vertically smoothed smoke aerosol extinction profiles from CALIOP were used to obtain the cumulative distribution of AOD, which was further normalized by the total column AOD (Fig. 6.2a, b). The normalized AOD values at each CALIOP vertical level were matched to model horizontal resolution using cubic interpolation method.
2. Simultaneously, model mass for individual smoke aerosol species (BC, OC or SO_4) was calculated at each model vertical level in kg m^{-2}. Cumulative mass distribution profiles were then obtained and normalized by the total column mass of any one of the smoke aerosol species at a time. The normalized cumulative distribution (NCD) of CALIOP AOD and model aerosol mass for a representative model grid are demonstrated in Fig 6.2b. The model NCD values are replaced by values from the CALIOP NCD at each model level.
3. The new model mass fractions (or CALIOP NCD) values obtained at each model vertical level in step 2 are finally used to back calculate the new mass concentrations at those levels, keeping the total column mass constant (Fig. 6.2c).

The steps 1-3 are repeated for each of the smoke aerosol species in the model. The assumption here is that the NCD of individual smoke aerosol species in the model are similar. This appears to be a valid assumption over our domain because we found the shape of the simulated mass profiles of individual smoke species to be similar, with differences only in absolute magnitudes. This is further illustrated in Figure 6.2d, e and f for the same example grid as above. Finally, the hydrophobic and hydrophilic portions of BC and OC are adjusted (not shown here) such that the ratio of their respective contribution to total species mass at each level is conserved even after redistribution.

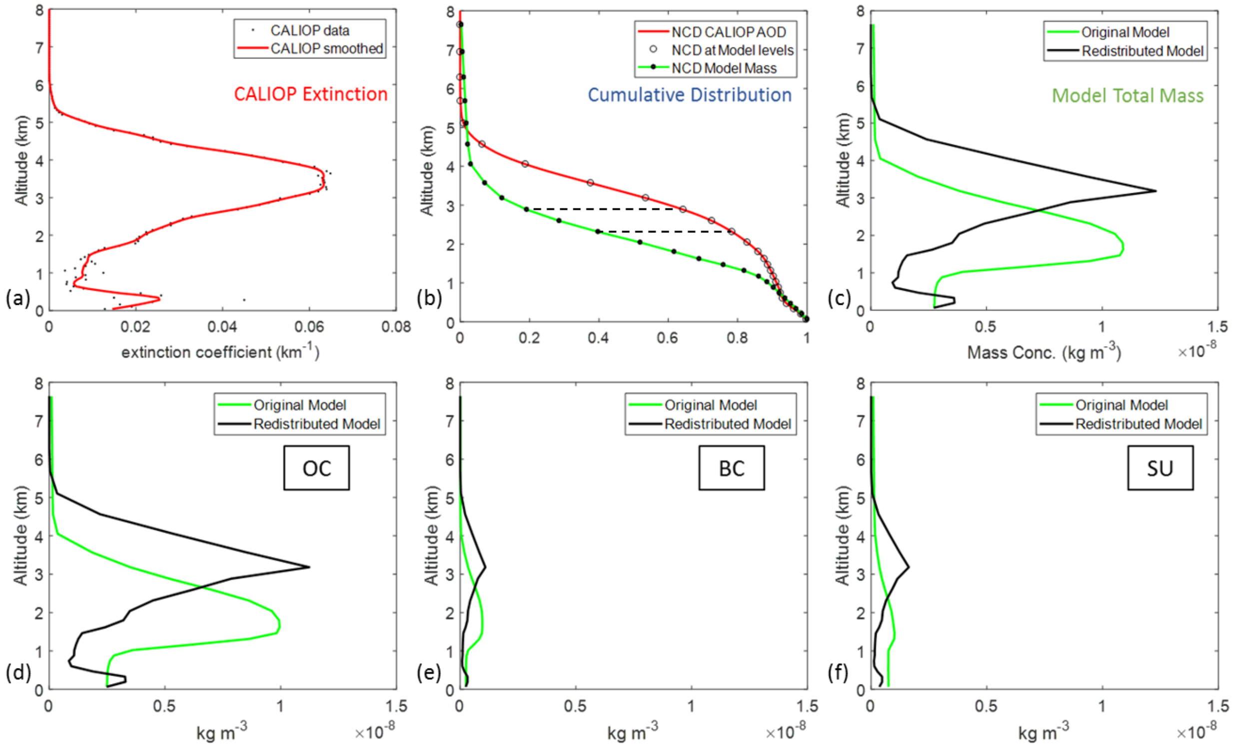

Figure 6.2. Demonstration of the redistribution methodology for one sample model grid and for total and individual smoke aerosol species mass in the model.

6.2.3 Model Configuration and Experimental Setup

The radiative transfer module in GEOS-5 incorporates the radiative forcing introduced by tropospheric aerosols using either the prognostic aerosols from an aerosol module integrated '*on-line'* within the model [*Colarco et al.,* 2010] or aerosols from a climatology based on prognostic aerosols produced by earlier simulations [*Randles et al.,* 2013]. For this study, we use the latter approach so that we can adjust the default aerosol climatology off-line to ensure closer agreement with observations. The default aerosol climatology for our study was obtained from the MERRAero aerosol reanalysis product [*Buchard et al.,* 2015] that covers the time-period from 2003-2014. Please note that the GEOS-5 simulations that produced MERRAero product used GOCART itself as its prognostic aerosol module.

The model (Heracles 5.3 version) was run at c180 cubed-sphere horizontal resolution with 72 hybrid vertical sigma levels extending between the surface and 0.01 hPa (about 85 km). The hybrid coordinate system is terrain following near the surface that gets transformed to pressure coordinates at higher altitudes (near 180 hPa). The model ocean was forced by climatological SSTs [*Reynolds et al.,* 2007]. The model simulations were conducted in the free-running AGCM mode, but the aerosol dry mass mixing ratio distributions were prescribed using a monthly-mean aerosol climatology instead of the prognostic aerosol fields calculated by the aerosol module at each model time-step. The model simulations were run from July-October 2008, but the results are averages over the peak BB months of August and September only. This allows July month to be discarded as the spin-up month, during which model reaches its preferred equilibrium state.

Table 6.1 Design of the Numerical Experiments

Simulations	**Aerosol Source**
Control (CTL)	MERRAero aerosol climatology
Redistributed Aerosol (RED)	MERRAero BC, OC and SO_4 aerosol mass was redistributed based on CALIOP extinction profiles
No Aerosol (NOA)	MERRAero climatology but no smoke aerosols over the ocean

We designed three sets of numerical experiments for GEOS-5 to test the model sensitivity to aerosol vertical distribution in simulating the direct and semi-direct effects of smoke aerosol over our region of interest. These are summarized in Table 1. For all the three cases, the model configuration remains the same, what changes is the aerosol climatological data used for prescribing the vertical distribution of aerosol dry mass mixing ratios in the model. To isolate the significant changes in model cloud responses due to aerosols as opposed to the internal model variability, we adopt 5-member ensembles starting from different initial meteorological conditions. In the control (CTL) case, the default (or MERRAero) aerosol climatology is used. For each model time-step, the aerosol fields are time-interpolated using the monthly-mean values. In the second case, the dry mass of smoke aerosol species (BC, OC and SO_4) are redistributed in vertical only over the ocean (0-20°S; 12°E-20°W) to match the aerosol vertical distribution observed by CALIOP using the methodology described in the previous section. In the third case, smoke aerosols are simply removed over the redistribution domain from the MERRAero aerosol climatology to obtain the baseline simulation for facilitating the estimation the direct and semi-direct effects of smoke aerosol on the radiation budget over our domain. Figure 6.3 below demonstrates the result of applying the redistribution methodology to the default MERRAero aerosol climatology of the model. The contrasts in the vertical distribution of smoke aerosols over the ocean in the CTL and RED case clearly show the effect of constraining the model aerosol mass using the CALIOP extinction data in RED.

To test the statistical significance of the changes in simulated quantities in between the experiments, two-tailed Student's t-test was utilized. The t-statistic was calculated using pooled variances definition given in Wilks (2006) as follows,

$$t = \frac{\overline{x}-\overline{y}}{\sqrt{\left(\frac{1}{n}+\frac{1}{m}\right)\times\left(\frac{(n-1)s_x^2+(m-1)s_y^2}{n+m-2}\right)}} \quad (6.1)$$

Here, the two sample populations (x and y) are the experiment (e.g. RED or NOA) and control (e.g. CTL) respectively. s_x and s_y are the population standard deviations, and n and m are the sample sizes of x and y respectively. The null hypothesis is that the population means are the same. Following the standard procedure of a t-test, the difference between the two means can be considered statistically significant if the null hypothesis can be rejected at a given confidence level. For this study, we have chosen 95% as our confidence level.

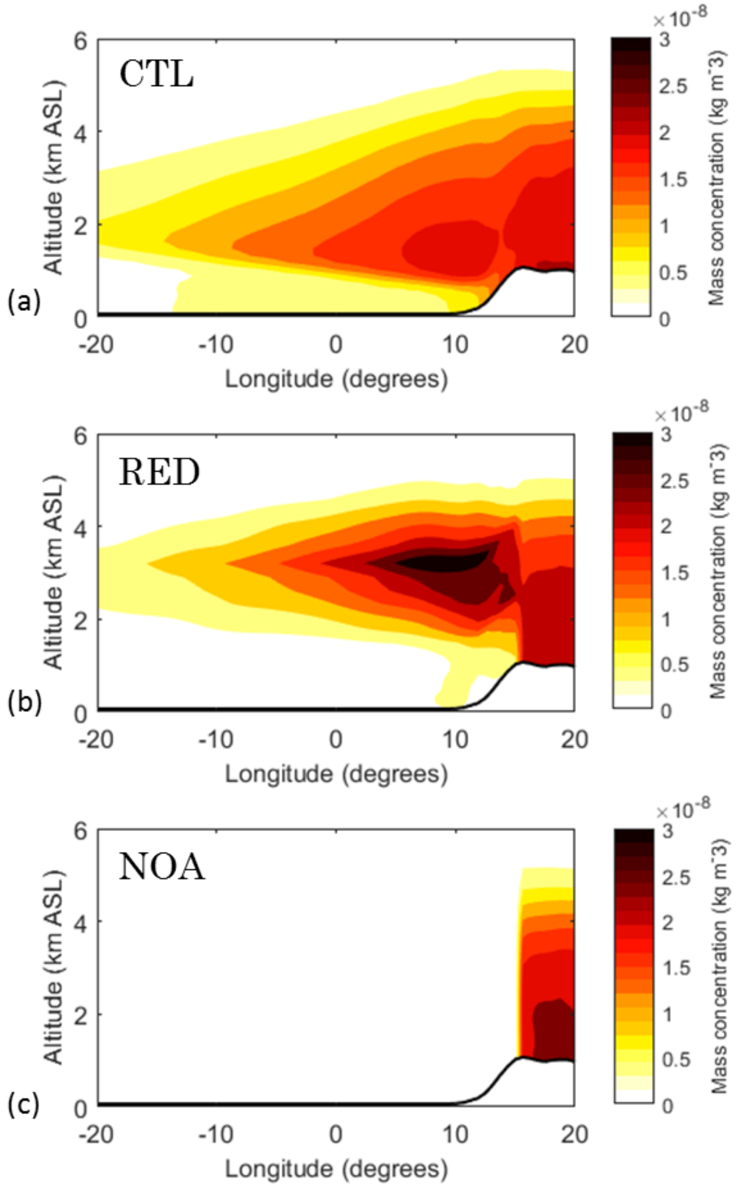

Figure 6.3. Application of the redistribution method and design of the experiments. Meridional cross-sections of smoke aerosol (BC, OC, and SO4) mass in GEOS-5 averaged over the latitudes of interest (0-20S) for (a) default/MERRAero climatology (CTL), (b) after redistribution in vertical according to CALIOP (RED) and removing smoke aerosols over the ocean (NOA).

6.3 Results and Discussions

Differences between the CTL and RED simulations are used to examine the model responses to the changes in aerosol vertical distribution with respect to the underlying cloud properties. At the same time, differences between RED and NOA simulations are used for examine the changes in the same properties caused by the presence of absorbing smoke aerosols in the model at locations observed by satellite instrument. Here, we focus on the months of August and September, which are the peak BB months of the year. So, all the quantities presented hereafter are averages over this period.

6.3.1 Model Cloud Responses to Changes in Aerosol Vertical Distribution

Figure 6.4 shows the horizontal distribution of ensemble mean low-level (up to 700 hPa) clouds in the model from the three sets of experiments along with the cloud fractions retrieved from MODIS. The domain over which we changed or removed the smoke aerosols in the model is depicted using a black line box on the bottom panels. In the panels showing changes in cloud fractions or for other cloud properties, stippling indicates the significant (95% confidence) changes as determined by the t-test. There was an increase in cloud fraction by about 40% for RED compared to NOA at areas of high aerosol loading near the coast. Between RED and CTL, there was an increase in cloud fraction near the coast by ~35% with respect to RED and a decrease in cloud fractions by ~25% for areas away from the coast and warmer sea-surface temperatures. Overall, the absolute magnitudes of changes in cloud fractions are small, but the percentage changes are large because the model simulated cloud fractions for the CTL case are much smaller and spatially displaced compared to the cloud fractions retrieved from MODIS to begin with. This deficiency of GEOS-5 echoes the persistent problem for global models in general to accurately simulate the distribution and amounts of stratocumulus clouds, be it over the Pacific or Atlantic Ocean [*Stier et al*., 2013].

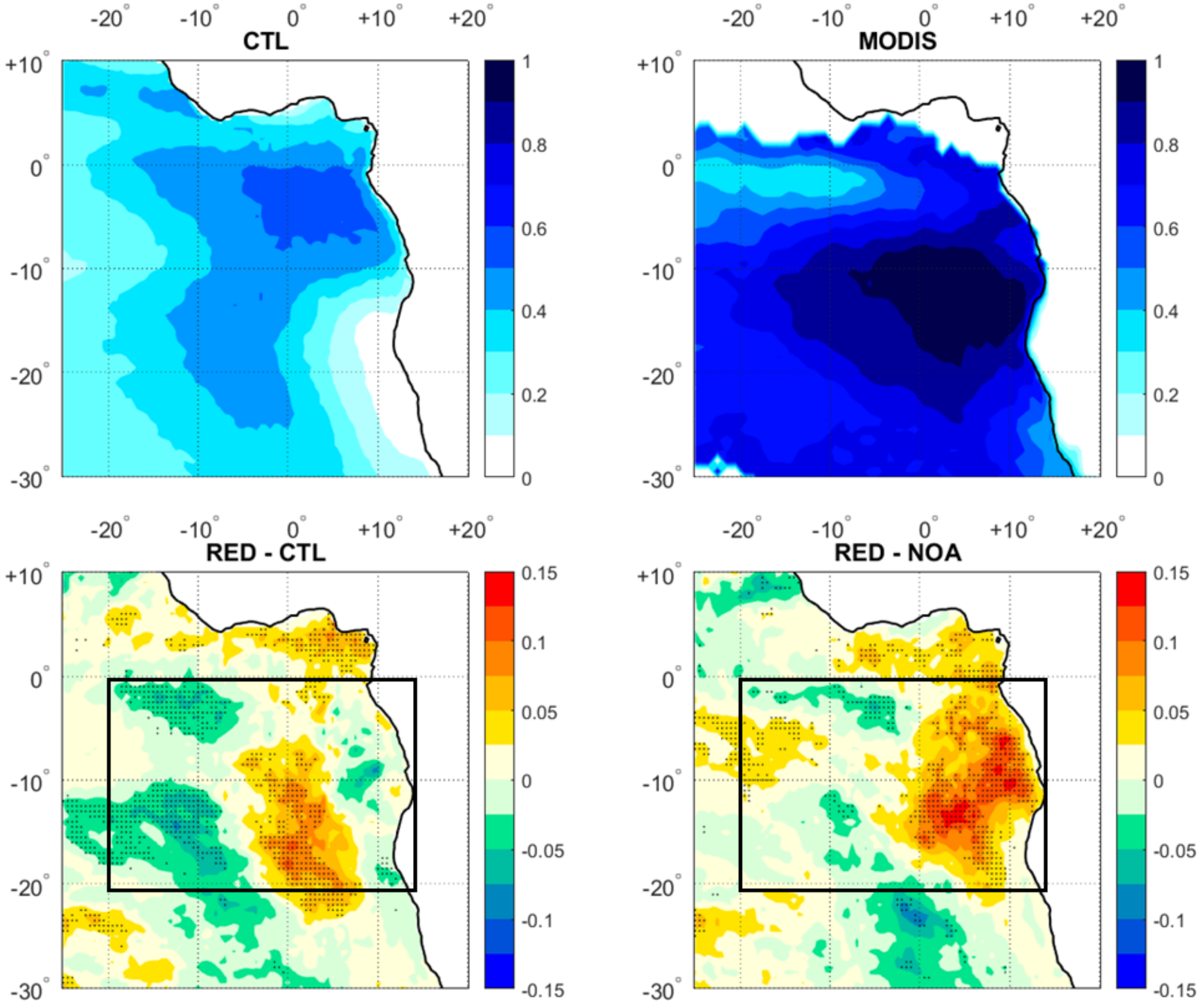

Figure 6.4. (Top-Left) Ensemble mean cloud area fraction for control (CTL) case. (Top-Right) Mean cloud area fraction retrieved from MODIS and averaged over August and September of 2008. (Bottom-Left) Changes in cloud fractions between Redistributed (RED) and control (CTL) simulations. (Bottom-Right) Changes in cloud fractions between Redistributed (RED) and no smoke aerosol (NOA) simulations. The black box in the bottom panels shows the domain over which aerosol aerosols were vertically redistributed. Black stippling on bottom panels indicates the significant (95% confidence) changes following the t-test.

(a) in-Cloud Optical Depth (5-member Ensemble mean)

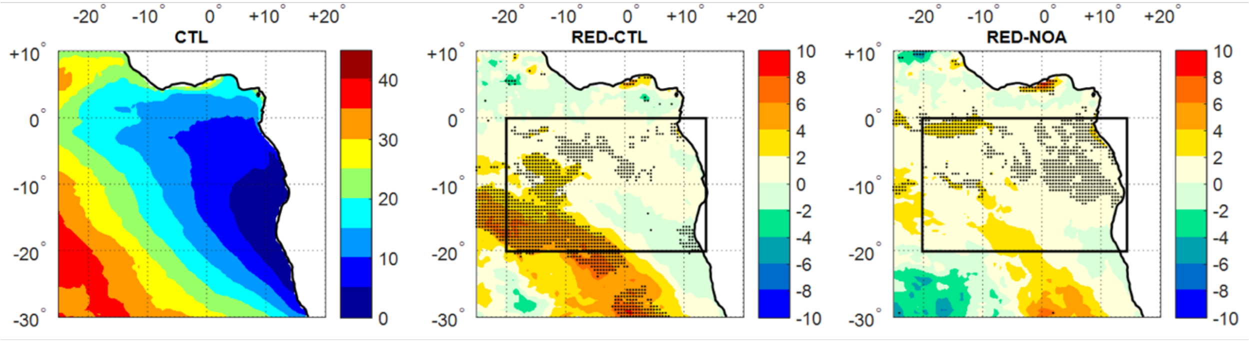

(b) MBL Height in km (5-member Ensemble mean)

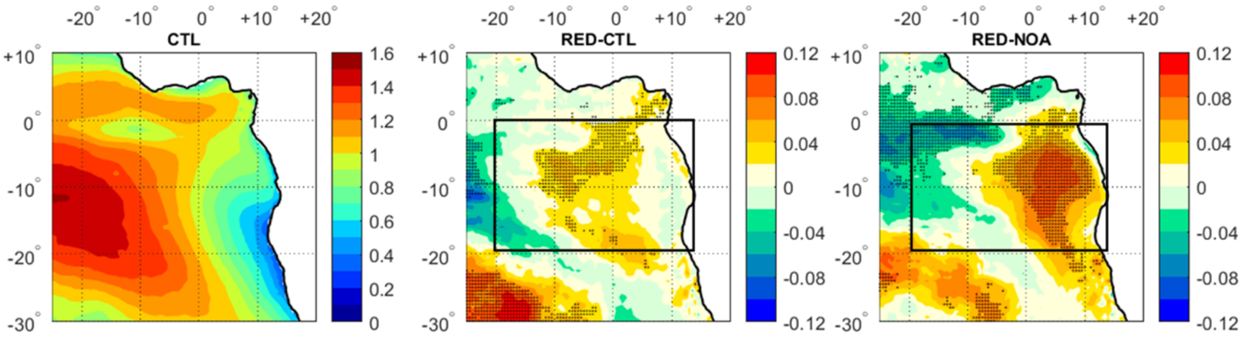

Figure 6.5 Changes in (a) in-cloud optical depth representative of cloud liquid water path and (b) MBL heights in between the experiments.

Changes in other cloud and MBL properties were also investigated. Fig 6.5 below depicts the changes in in-cloud optical depth (OD) and MBL heights in between the experiments. The in-cloud OD is compared here as a proxy to cloud liquid water amounts because it is directly proportional to the cloud LWP for a given cloud top effective radius (see equation 1.8 of chapter1). Since the cloud droplet sizes have most likely not changed in between the experiments, we can infer that cloud LWP shows minimal changes in between the experiments. However, there is a slight increase by about 20-25% of in-cloud ODs in RED compared to CTL at areas away from the coast and south of the redistribution domain. There is also in increase in MBL heights by about 100 m at areas near the coast, coinciding with the increase in cloud area fractions for the elevated smoke aerosols case (RED) compared to the pristine case (NOA).

6.3.2 Explaining the Changes in Cloud Properties

There appears to be two distinct regions where cloud amounts show substantial changes. One is the region near the coast extending up to ~ 5W, where cloud amounts increase for RED compared to both CTL and NOA. We will call this the cloud-increase region. The second region comprises of the areas farther offshore and beyond 5W, where there is a slight decrease in cloud fractions in RED compared to CTL, which interestingly is accompanied by the increase in cloud LWP amounts as well. We will call this the cloud-decrease region. Hence, we will sequentially examine the thermodynamic and radiative quantities over the two regions to understand the reasons for the observed changes in cloud and MBL properties.

Figure 6.6a shows the changes in SW and LW radiative heating rates and Figure 6.6b shows the changes in vertical pressure velocities indicative of the subsidence strength over cloud-increase region. Fig 6.7 shows the changes in temperature profiles over the same region. When dealing with cloud processes, it is often useful to plot the moist-conserved variables such as liquid-water potential temperatures (θ_L) and total water mixing ratio (Q_T) because phase changes of water are involved along with the adiabatic changes. Q_T here is simply the sum of grid-averaged specific humidity (Q_v) and liquid water (Q_L) at each model level, i.e. $Q_T = Q_v + Q_L$, whereas θ_L is defined as follows.

$$\theta_L = \theta \exp\left(\frac{L_v Q_L}{c_p T_{LCL}}\right) \tag{6.2}$$

Here θ is the potential temperature, L_v is the latent heat of vaporization of liquid water, c_p is the specific heat capacity of dry air and T_{LCL} is the temperature of dry air at the Lifted Condensation Level (LCL) or cloud base. Here, we have assumed cloud base to be the model level at which cloud liquid water content first exceeds 10% of its maximum value starting from the surface and below 3 km.

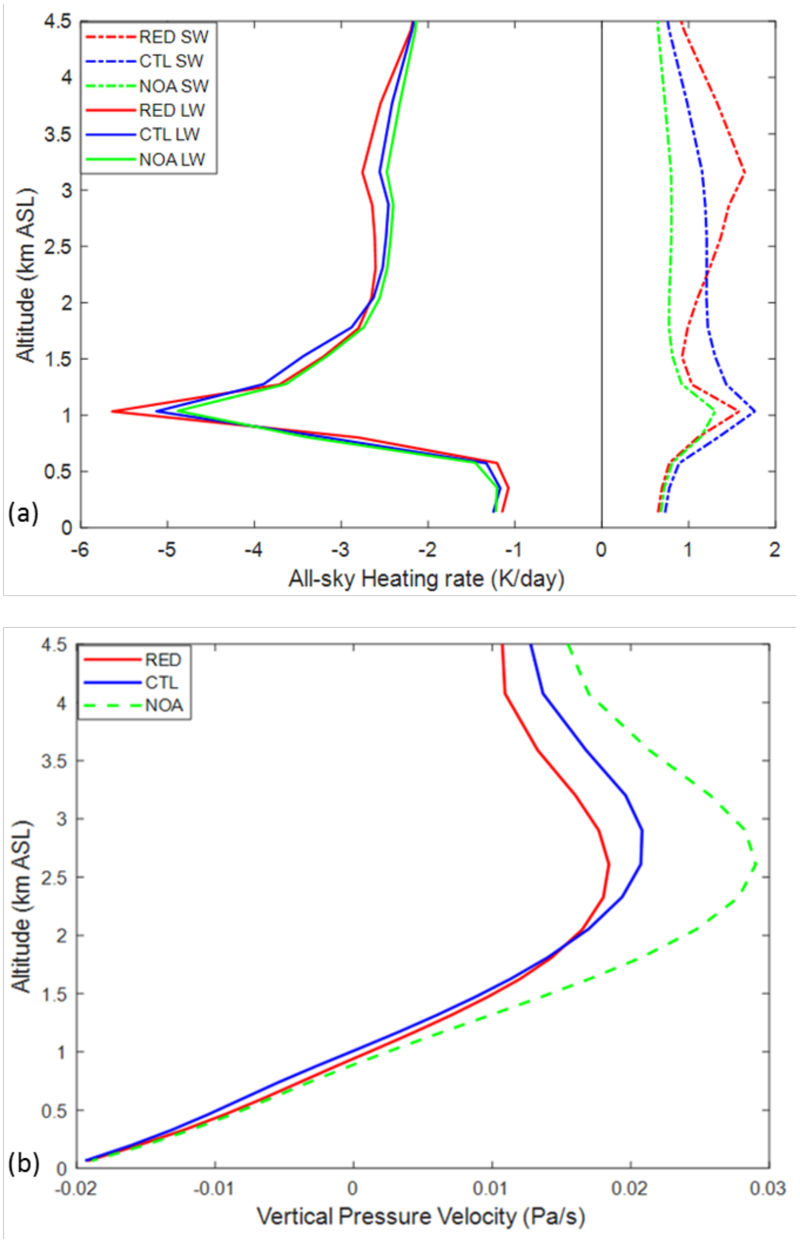

Figure 6.6 (a) All-sky long wave (LW) and short wave (SW) heating rates and (b) vertical pressure velocities are averaged over the areas (12E-5W, 0-20S) that show most differences between the cloud amounts in RED and NOA case. This area also corresponds to the cloud increase region for RED compared to CTL.

The atmospheric constituents that strongly absorb SW radiation in our case are BB aerosols and water vapor. Thus, the differences in heating rates between NOA (green) and aerosol containing RED (red) and CTL (blue) runs in SW profiles corresponds to the effects of aerosol absorption, especially at the levels of low-humidity above the cloud-tops. Aerosols do not respond much to LW radiation, thus LW cooling profiles on the right side of the origin in solid lines show the presence of clouds and the cooling maxima corresponds to the excessive LW cooling at the cloud-tops. It should be noted here that the magnitudes of LW cooling within the clouds are much higher than the SW heating rates within the clouds, meaning that the SW absorption by aerosols within or near the cloud-tops is overpowered by the LW cooling at these levels. At levels above the cloud-tops however, it is clear that elevating the aerosol layer to higher levels causes a decrease in SW heating by about 0.5 K/day between 1-1.5 km ASL in RED compared to CTL.

It is also interesting to note the changes in the subsidence strength is caused by the presence of aerosols in the model and also at what levels the aerosol layer is placed. It is clear from Figure 6.6b that subsidence near the coastal areas is weakened by about 30% when absorbing aerosols are placed as in CTL compared to NOA. The subsidence is further weakened by extra 20% when the aerosol layers are elevated to match the extinction peaks at 3-4 km as in CALIOP observations (RED). As discussed previously, large-scale subsidence at regions of stratocumulus clouds dictates the MBL depths and are also associated with warming at the upper end of the capping inversion. Thus, weakening of subsidence can be inferred as cooling of the inversion temperatures.

Therefore, owing to both aerosol heating effects and changes in subsidence strength, temperatures of the overall inversion layer have reduced by ~2 K (between 1-1.5 km) in RED compared to NOA and by ~1 K compared to CTL. This is reflected in both mean dry-air and liquid water potential temperature profiles over this region (Fig. 6.7). Although not as apparent, there also appears to be a slight weakening of the inversion in RED, especially compared to NOA.

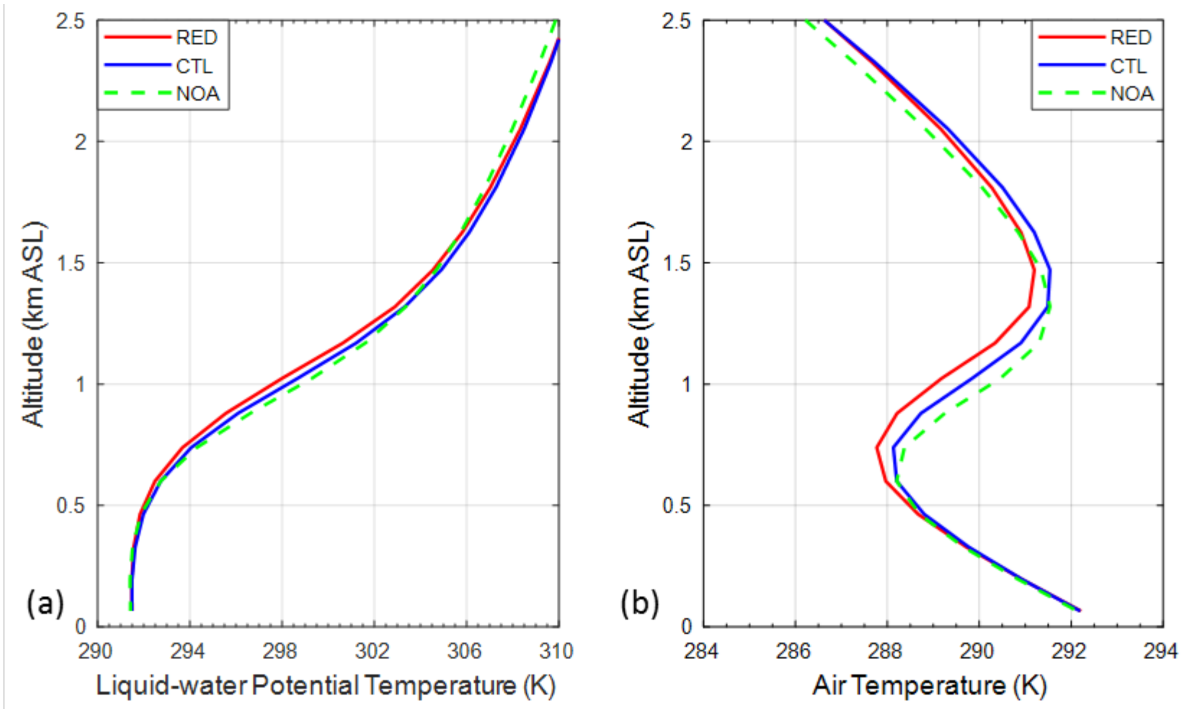

Figure 6.7 (a) Liquid -water Potential temperature and (b) dry-air temperatures profiles averaged over the cloud-increase region for RED, CTL and NOA cases.

Relating these changes in cloud-top inversion layer temperatures to the changes in cloud LWP or cloud fractions in global climate models can be different than the mechanism explained in *Johnson et al.,* (2004) and summarized in section 1 of this chapter. This is because unlike the LES models that explicitly simulate the cloud processes, stratocumulus cloud properties in global models are calculated using a prognostic large-scale cloud scheme and are further dependent on the cloud-top entrainment parameterization included in the model boundary layer mixing scheme. The prognostic cloud cover and cloud water scheme in GEOS-5 for large-scale clouds i.e. stratocumulus clouds here is from Bacmeister et al. (2006). It assumes that the probability distribution function of total water (Q_T) is top-hat shaped [*Smith,* 1990; *Rienecker et al.,* 2008], where the width of the distribution is associated with a grid box critical relative humidity (RH_{crit}). RH_{crit} is the RH at which condensation or deposition begins. RH_{crit} is also a limiting relative humidity for the evaporation and sublimation processes, which are restricted to prevent the gridbox relative humidity from exceeding RH_{crit}. The vertical profiles of RH_{crit} were updated using the Atmospheric Infrared Sounder (AIRS) observations after Molod (2012), which now have a dependence on model horizontal resolution as well. Thus, the following two equations are solved in the model to obtain the large-scale cloud fraction and cloud condensate amount (Q_c) for a given RH_{crit} profile.

$$C_f = \int_{q*}^{q_{max}} P(Q_T)\, dQ_T\,, \qquad where \int_{q_{min}}^{q_{max}} P(Q_T)\, dQ_T = 1 \tag{6.3}$$

and

$$Q_C = \int_{q*}^{q_{max}} (Q_T - q^*)\, P(Q_T)\, dQ_T\ . \tag{6.4}$$

Here, q^* is the saturation specific humidity for the grid box, P (Q_T) is the probability of finding a particular value of Q_T in a grid box, and $q_{max,min} = \overline{Q_T} \pm 0.5\ \Delta q$. Here, Δq is the width of the probability distribution that is associated with the predetermined RH_{crit}, while overbar denotes the grid-box mean value. The equations simply mean that condensation occurs for the values of Q_T that exceed saturation, and that the cloud fraction is the fraction of the grid box where Q_T exceeds saturation. Thus, cloud formation is favored in the model when the box average of specific humidity increases and the corresponding temperature decreases to lower the saturation threshold of specific humidity.

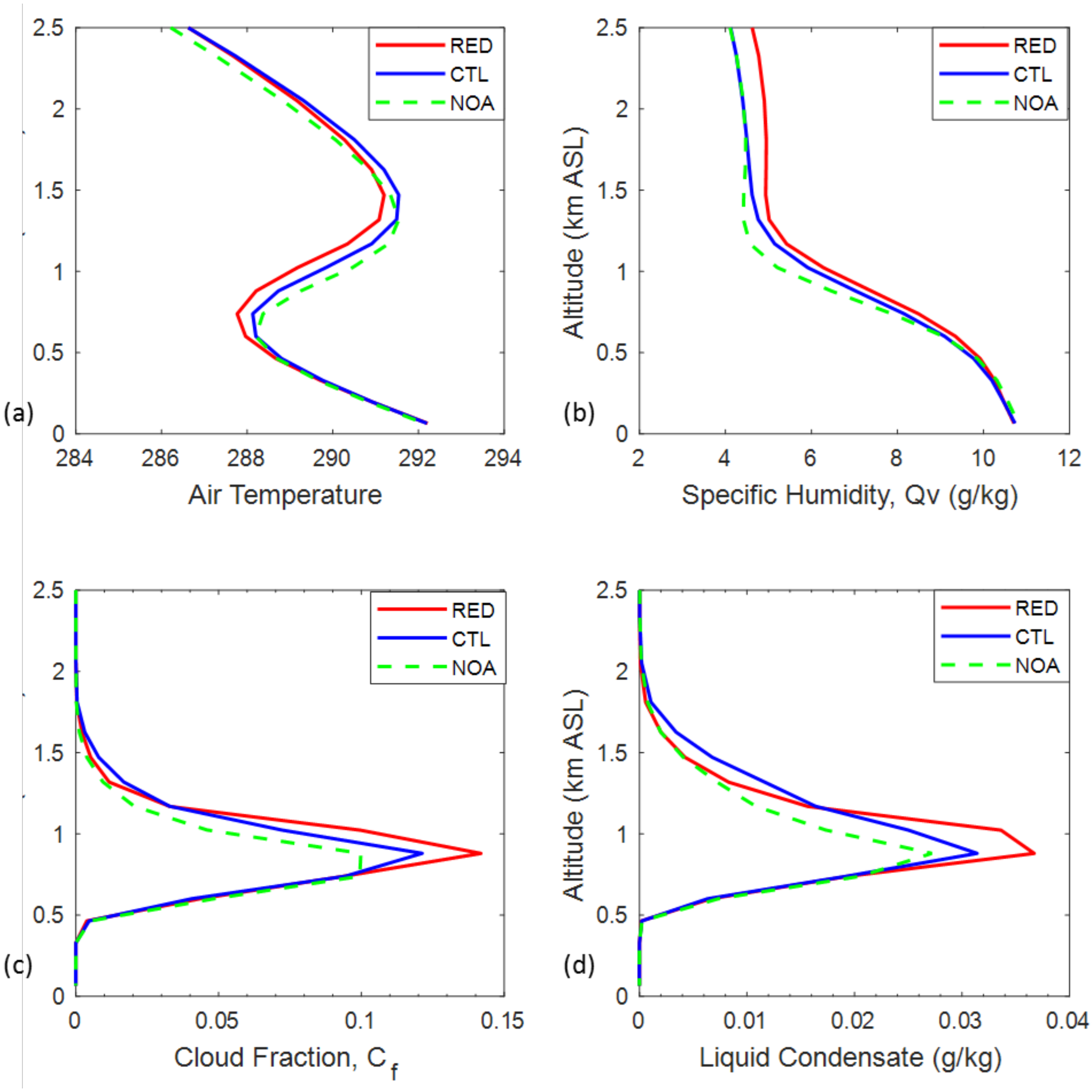

Figure 6.8 Relating temperature and humidity profile changes to cloud fraction and liquid condensate amounts within the clouds. (a) Dry-air temperature, (b) Specific humidity, (c) cloud fractions and (d) liquid condensate amounts averaged over the cloud-increase region.

For weaker inversions, the thermals or turbulent eddies that create or maintain the stratocumulus cloud layer can penetrate deeper in the atmosphere and bring in more moisture to the boundary layer from the ocean surface [*Wood* 2012]. For the cloud-increase region, therefore, the weaker inversion in RED compared to CTL is allowing more moisture from within the MBL to escape above the cloud-tops and the simultaneous decrease in temperatures at the same levels is causing more water to condense out (Fig 6.8). Now, a weaker inversion should also lead to an increase in entrainment rate of the free-tropospheric air from above the cloud-tops, which should further lead to a decrease in the liquid water content within the MBL [*Johnson et al.,* 2004; *Wood* 2012]. Yet again, since the cloud-top entrainment for stratocumulus clouds is parameterized in GEOS-5 using Lock et al., (2000) that was further modified in the more recent versions of the model [*Molod et al.,* 2012; 2015], it is hard to comment on the effectiveness of the entrainment parameterization in simulating the entrainment rates closer to reality or at least LES simulations. Thus, what follows in the model for RED compared to NOA and CTL are two things, one is reduction of RH within the MBL due to entrainment of dry air from above the cloud-tops, thus opposing cloud formation and second is the increase in RH near the cloud-tops following the simultaneous increase in specific humidity and decrease in temperatures at these levels, thus favoring cloud formation. Clearly for RED simulations, effect of increase in large-scale cloud condensation around cloud-tops is dominating the effects of cloud-top entrainment to cause an overall increase in cloud LWP (Fig. 6.8d).

While explaining changes in cloud fractions (C_f), as shown in Figure 6.4, another level of approximation within GEOS-5 needs to be understood. A maximum cloud overlapping scheme is adopted within each cloud super-layer (low, middle or high) to arrive at a single value of C_f required by the radiation scheme. Thus, low-level cloud fraction for each model column is simply the maximum value of the cloud fractions calculated at each model vertical level between 700-1000 hPa [*Chou and Suarez* 1999]. So, the changes in cloud fraction depicted in Fig. 6.4 are changes in the maximum value of C_f in between the three experiments.

Now, to explain the changes in cloud properties over the cloud-decrease region, we first plot the ensemble mean cloud and boundary layer properties for this region (Fig. 6.9). The differences in temperature and humidity profiles in between the three experiments is very small, yet there is about 15-20% change is liquid condensate amounts between RED and CTL, accompanied changes in cloud fractions as well. The interesting thing however are opposing changes in cloud fractions and liquid water amounts. This can be explained by the phenomenon of stratocumulus to cumulus-like transition of the clouds (SCT) that is driven by increase in sea-surface temperatures and weakening of subsidence as one moves away from the coast [*Xiao et al.,* 2010].

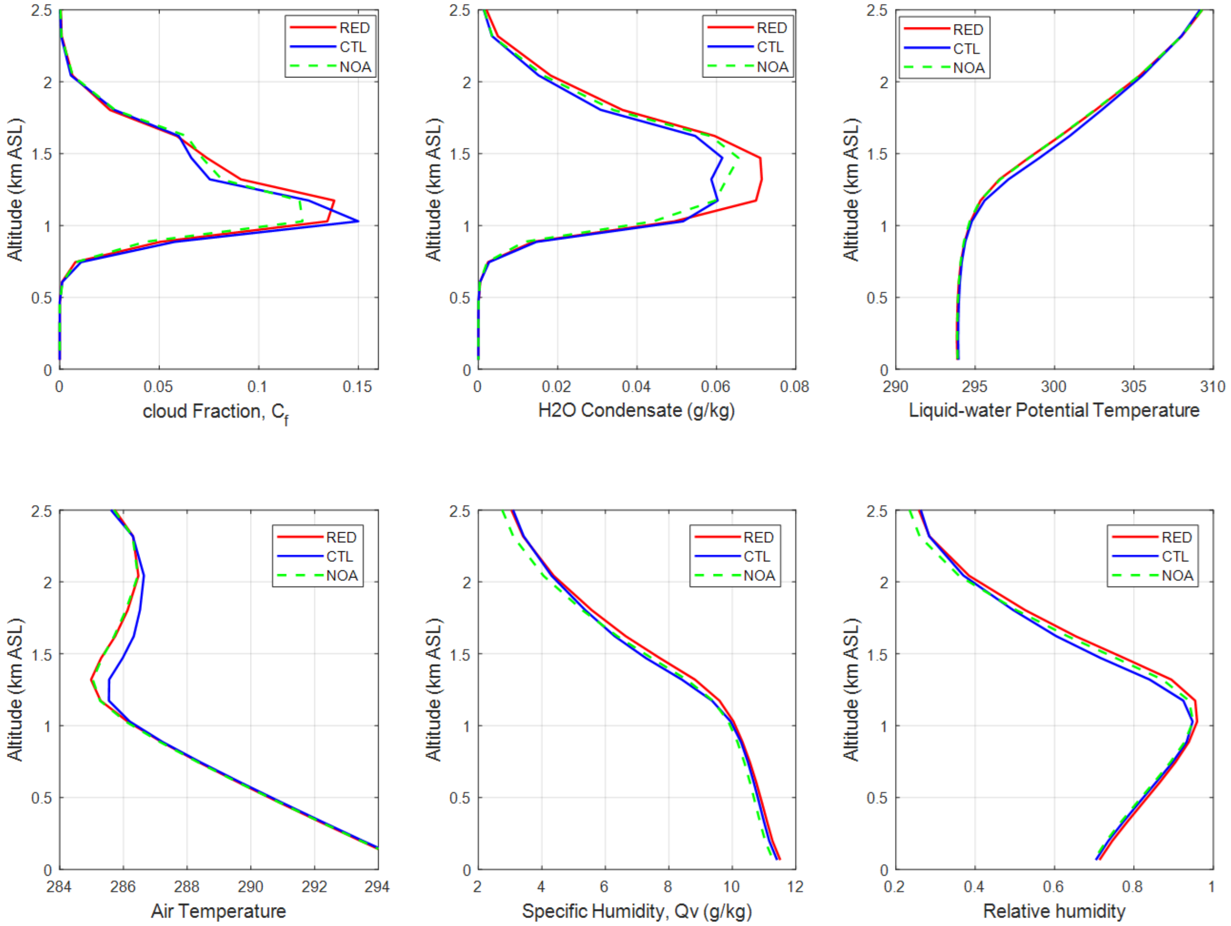

Figure 6.9 Ensemble mean boundary layer and cloud properties for the cloud-decrease region.

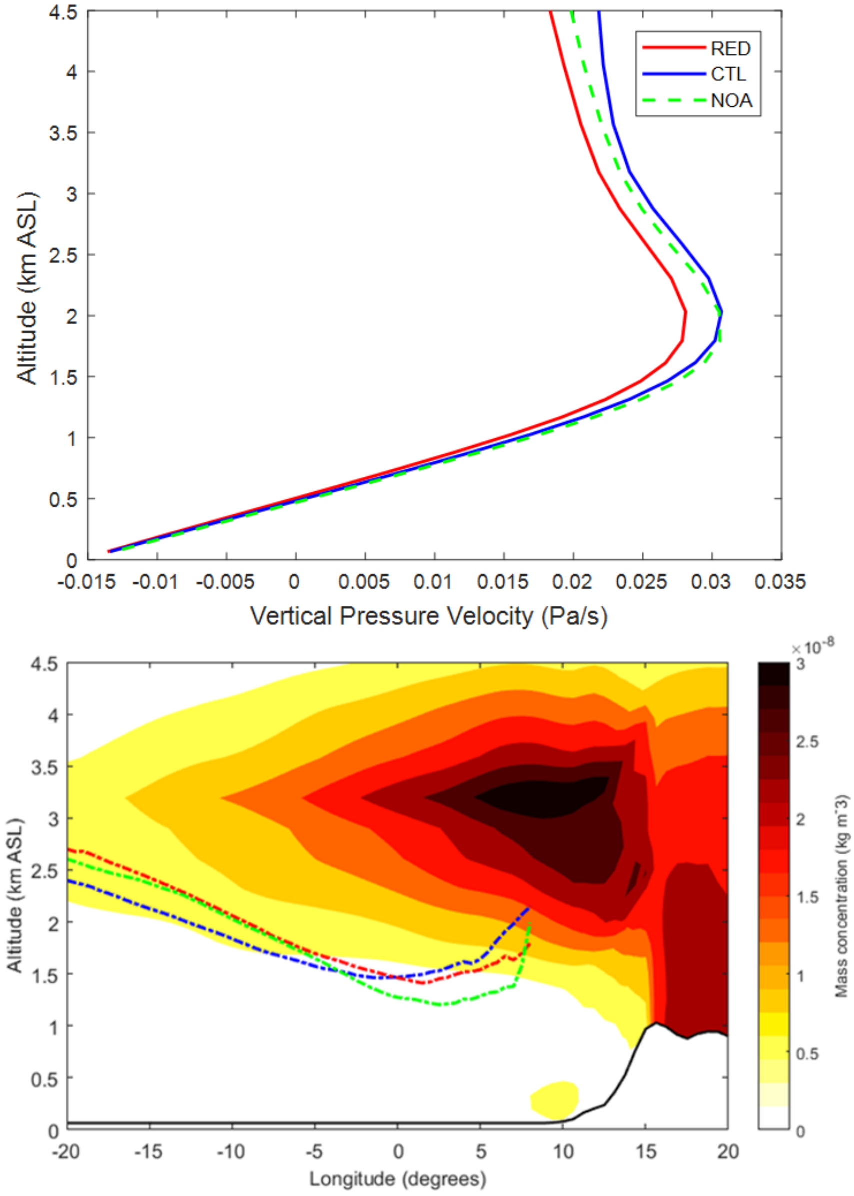

Figure 6.10 (Top) Changes in vertical pressure velocities over cloud-decrease region. (Bottom) Cloud-top heights from the three experiments are overlaid (dotted lines) on the aerosol mass concentration contours for the RED case. The model output of cloud-top pressures in infrared channel (540-980 cm^{-1}) were converted to geopotential heights to obtain the cloud-tops.

Figure 6.10 shows the changes in subsidence strength in the top panel and changes in cloud-top heights in the bottom panel for the three experimental cases. The modeled cloud-top heights corresponding to the model simulated cloud-top pressures are overlaid on the aerosol mass concentration contours for the RED case to understand the shift in the location of the cloud tops for each experiment with respect to the aerosol layer. The GEOS-5 simulated cloud-top pressure here is defined as the pressure at the top of the first cloud detected in the infrared channel (540-980 cm^{-1}) starting from the top of the atmospheric column. Clouds are visible if in-cloud optical thickness in this band exceeds 0.14, independent of their fractional area coverage. To account for the low stratocumulus clouds therefore, instantaneous cloud-top pressure values more than 680 hPa were only considered while averaging over the two months (August-September) following the ISCCP (International Satellite Cloud Climatology Project) convention.

Since the SST distributions are constant in between RED and CTL case, the main driver for SCT between the experiments is the change in subsidence strength. It is clear that RED case over this region shows higher cloud tops owing to the weaker subsidence. SCT region is often characterized by puffy small clouds with low cloud fractions and very active vertical transport of moisture and heat within the MBL [*Xiao et al., 2010*]. This explains the decrease in cloud fraction values and simultaneous increase in LWP values in RED compared to CTL for areas away from the coast. Effectively, the presence of the elevated aerosol layer as opposed to the presence of aerosol layer near the cloud-tops seems to hasten the SCT in GEOS-5. This is similar to the results of Zhou et al., (2017) who used a LES model to study the effects of absorbing aerosol layer on SCT over the same region of SE Atlantic.

6.3.3 Direct and Semi-Direct Effects of Aerosol on Radiative Forcing

As discussed earlier in the introduction section, BB aerosols in this region can disrupt the energy balance between the incoming and outgoing radiation, both at TOA and ocean surface, by directly absorbing the SW radiation and alternately by causing a change in the albedo and coverage of the underlying clouds. Figure 6.11 shows the horizontal distribution of the estimates of aerosol effects on all-sky total (LW and SW) radiative forcing (RF), including the differences caused in these estimates due to aerosol redistribution (right-most panels).

(a) TOA all-sky Radiative Forcing (W/m²)

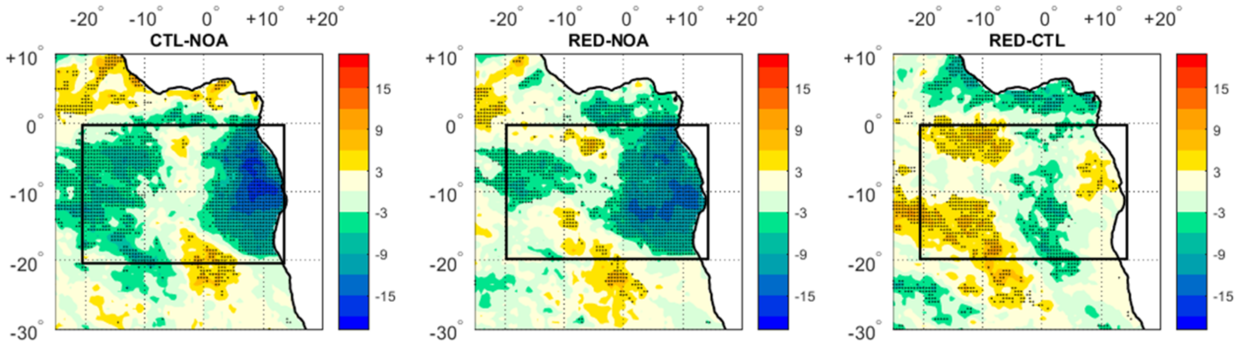

(b) Surface Radiative Forcing (W/m²)

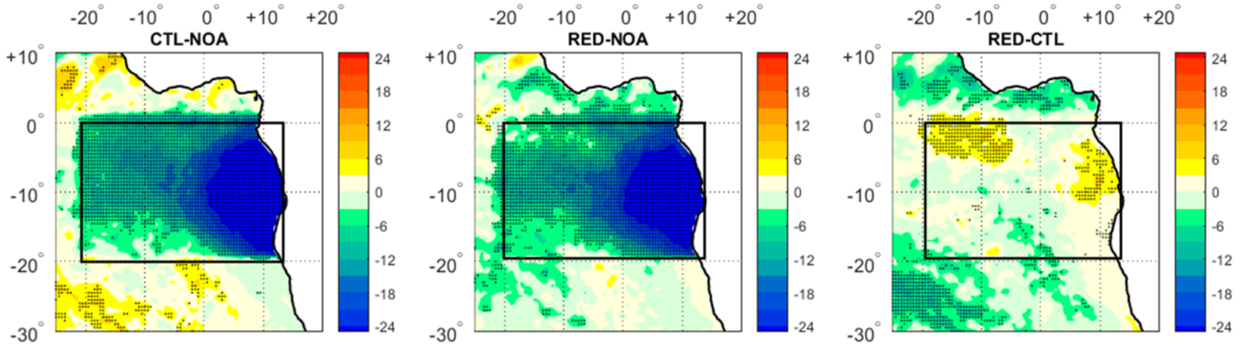

Figure 6.11 Changes in instantaneous RF due to smoke aerosols calculated at (a) the TOA and (b) the surface for all-sky conditions and combining both SW and LW.

The negative values represent cooling, which at TOA should indicate a larger contribution from highly reflecting stratocumulus clouds, while BB aerosol layer by itself causes a warming effect at TOA due to its absorbing nature. At the surface however, both clouds and aerosol have a cooling effect. Increase in cloud LWP or thickness increases cloud albedo and increase in cloud cover (or C_f) also results in an overall increase in the amount of radiation being reflected to the space. Thus, negative semi-direct effects can have a separate contribution from an increase in either of these variables (LWP or C_f). Clearly, the changes in TOA RF due to aerosols or aerosol redistribution closely resembles the pattern of changes in C_f distribution in between the three experiments, as illustrated in Figure 6.4. Thus, at TOA at least, the effects of increase in cloud LWP or the direct effects of increase in aerosol absorption in both RED and CTL compared to NOA appear to have been overpowered by the effects of changes in cloud cover. At surface, increase in clouds as well as aerosol in CTL and RED are causing an increase in ocean surface cooling compared to NOA, indicating that ocean surface cooling is strongly enhanced by the presence of absorbing aerosol layer above the cloud surface, irrespective of the differences in its vertical location in the atmospheric column. Overall, this is a very preliminary discussion based on the total RF values, a further stratification of total DRE into direct and semi-direct effects will need to be conducted to quantify the relative contribution of aerosol absorption, LWP changes and C_f changes towards DRE of BB aerosol over this region.

CHAPTER 7. SUMMARY AND CONCLUSIONS

7.1 Aerosol Plume Transport Evaluation

We evaluated the simulations of long-range transport and vertical distribution of BB aerosol by GEOS-5 and four other AeroCom models over the complete south African-Atlantic region using satellite observations for the peak BB months of August and September. The observations were derived from CALIOP version 3.01 Level 2 nighttime data for smoke extinctions at 1064 nm, which were converted to 550 nm for fair comparisons with the models using an appropriate value of the Ångstrom exponent for the region. The domain of interest was divided into three sub-regions to understand the distinct patterns of aerosol transport or vertical distribution that existed within the domain. Multi-model evaluation highlighted the discrepancies between the observed and simulated aerosol transport that might be common to most of the global models in this important region of BB. Possible causes of these discrepancies in the context of GEOS-5 were investigated to get directions towards improvement of the model performance in the region. The major findings of the study are summarized below.

1. The mean smoke AOD from our CALIOP gridded product was within 10-20% of mean MODIS AOD over both the land and oceanic parts of the domain. The magnitudes of BB AOD from GEOS-5 (with QFED2 emissions) were in good agreement with those from CALIOP over land areas, but the AOD gradient from land to ocean in GEOS-5 (~10% decrease) was found to be much lower than in CALIOP (~50% decrease). Using different BB emission inventories (QFED2 and GFED3), the GEOS-5 AOD could be changed by about a factor of 2. However, the horizontal and vertical distribution of BB aerosol in the model, including the AOD gradient from land to ocean are unaffected by the use of either of the emission inventories.

2. GEOS-5 simulated BB aerosol extinction profiles were consistent with CALIOP observations over the burning source region (over land). However, for areas downwind of the burning sources (over ocean), the peak of the model simulated mean smoke extinction profiles occur at altitudes 1-2 km lower than the peak of CALIOP retrieved extinction profiles. In addition, GEOS-5 simulated clouds over the ocean appear to be more southwards and farther away from the coast compared to MODIS clouds, with maximum cloud fraction values of only ~0.5 compared to 0.9 or higher from MODIS. Both these findings are crucial for studies quantifying the impact of absorbing aerosol on the underlying clouds in this region. The aerosol semi-direct effect can change signs depending on whether the bulk of the absorbing aerosol occur above or within cloud levels. Moreover, for the aerosol effects on clouds to effectively feed back to the model climate, aerosol-cloud overlap and cloud amounts need to be accurately simulated.

3. Multi-model evaluation of BB aerosol plume transport using CALIOP observations showed that models were in general able to capture the aerosol plume top heights over land, irrespective of the differences in emission injection height assumptions. Over the ocean, however, the modeled aerosol plumes quickly descend to lower levels just off the west coast, relative to the heights up to which they were lofted over land. In contrast, CALIOP smoke plumes continue their horizontal transport at elevated levels above the MBL (with extinction peaks between 3-4 km ASL). The levels to which the aerosol plumes get subsided and the steepness of their descent vary amongst the models and also amongst the different sub-regions in the domain. Overall, CAM5 simulated BB aerosol transport over the ocean showed closer agreement with CALIOP observations compared to the other models in this study.

4. Investigations into the possible causes of differences in GEOS-5 and CALIOP smoke transport over the ocean indicated that aerosol removal processes in GEOS-5 play a minor

role in causing the observed differences. Instead, there is most likely an overestimation of subsidence over the ocean in the model-simulated large-scale vertical velocities. Large differences in model simulated off-shore CMFs between GEOS-5 and CAM5 in terms of both intensity and spatial distribution suggest further investigations towards evaluation of GEOS-5 simulated convective transport in this region. At the same time, possible discrepancies in model CMFs cannot solely explain the differences in GEOS-5 and CALIOP smoke transport at altitudes above 2 km over the ocean.

7.2 Sensitivity to Aerosol Vertical Distribution

The differences between the modeled and observed aerosol vertical distribution can be crucial in estimating the radiation budget over this key region of BB because the model cloud responses to aerosol-radiation interactions are strongly dependent on the relative location of the aerosol layer with respect to the clouds. Consequently, we evaluated the GEOS-5 sensitivity to changes in aerosol vertical distribution to this end by constraining the modeled aerosol vertical profiles using CALIOP observations. This was achieved by developing a methodology to redistribute the model simulated column mass according to the mean extinction profiles retrieved from CALIOP over the same column. Three sets of simulations were made, each containing 5-ensemble members. Control case (CTL) results are obtained by prescribing the aerosol dry mass in the model based on the default MERRAero climatology. Second set of experiments are performed by using the vertically redistributed profiles of aerosol mass from MERRAero (RED) and the final set is performed by removing the smoke aerosols over the domain (NOA). Changes in model cloud distributions and properties were analyzed to obtain the following outcomes.

1. There was an increase in cloud fraction by about 40% for RED compared to NOA at areas of high aerosol loading near the coast. Between RED and CTL, there was an increase in cloud fraction near the coast by ~35% with respect to RED and a decrease in cloud fractions by ~25% for areas away from the coast and warmer sea-surface temperatures.

2. Overall, the absolute magnitudes of changes in cloud fractions are small, but the percentage changes are large because the model simulated cloud fractions for the CTL case are much smaller and spatially displaced compared to the cloud fractions retrieved from MODIS to begin with.

3. Aerosol effects on TOA all-sky radiative forcing showed close resemblance to the pattern for cloud fraction change, wherein increase in cloud cover led to enhanced cooling and vice versa. Aerosol impacts on surface radiative forcing however, suggested a strong cooling of the ocean surface irrespective of where the aerosol layer is placed in the atmosphere.

REFERENCES

Abel, S. J., E. J. Highwood, J. M. Haywood, and M. A. Stringer (2005), The direct radiative effect of biomass burning aerosols over southern Africa, *Atmos. Chem. Phys.*, *5*(7), 1999-2018, doi:10.5194/acp-5-1999-2005.

Adebiyi, A. A., P. Zuidema, and S. J. Abel (2015), The convolution of dynamics and moisture with the presence of shortwave absorbing aerosols over the Southeast Atlantic, *J. Clim.*, *28*(5), 1997-2024, doi:10.1175/Jcli-D-14-00352.1.

Allen, R. J., and W. Landuyt (2014), The vertical distribution of black carbon in CMIP5 models: Comparison to observations and the importance of convective transport, *J. Geophys. Res. Atmospheres*, *119*(8), 4808-4835, doi:10.1002/2014jd021595.

Anderson, B. E., W. B. Grant, G. L. Gregory, E. V. Browell, J. E. Collins, G. W. Sachse, D. R. Bagwell, C. H. Hudgins, D. R. Blake, and N. J. Blake (1996), Aerosols from biomass burning over the tropical South Atlantic region: Distributions and impacts, *J. Geophys. Res. Atmospheres*, *101*(D19), 24117-24137, doi:10.1029/96JD00717.

Andreae, M. O., and P. Merlet (2001), Emission of trace gases and aerosols from biomass burning, *Global Biogeochem. Cycles*, *15*(4), 955-966, doi:10.1029/2000GB001382.

Bacmeister, J. T., Suarez, M. J., and Robertson, F. R. (2006), Rain reevaporation, boundary layer-convection interactions, and Pacific rainfall patterns in a AGCM, *J. Atmos. Sci.*, 63, 3383–3403.

Belikov, D. A., et al. (2013), Off-line algorithm for calculation of vertical tracer transport in the troposphere due to deep convection, *Atmos. Chem. Phys.*, *13*(3), 1093-1114, doi:10.5194/acp-13-1093-2013.

Bey, I., D. J. Jacob, R. M. Yantosca, J. A. Logan, B. D. Field, A. M. Fiore, Q. Li, H. Y. Liu, L. J. Mickley, and M. G. Schultz (2001), Global modeling of tropospheric chemistry with assimilated meteorology: Model description and evaluation, *J. Geophys. Res. Atmospheres*, *106*(D19), 23073-23095, doi:10.1029/2001JD000807.

Bian, H., M. Chin, S. R. Kawa, B. Duncan, A. Arellano, and P. Kasibhatla (2007), Sensitivity of global CO simulations to uncertainties in biomass burning sources, *J. Geophys. Res. Atmospheres*, *112*, D23308, doi:10.1029/2006jd008376.

Bian, H., M. Chin, S. R. Kawa, H. Yu, T. Diehl, and T. Kucsera (2010), Multiscale carbon monoxide and aerosol correlations from satellite measurements and the GOCART model: Implication for emissions and atmospheric evolution, *J. Geophys. Res. Atmospheres*, *115*, D07302, doi:10.1029/2009JD012781.

Bian, H., et al. (2013), Source attributions of pollution to the Western Arctic during the NASA ARCTAS field campaign, *Atmos. Chem. Phys.*, *13*(9), 4707-4721, doi:10.5194/acp-13-4707-2013.

Bond, T. C., et al. (2013), Bounding the role of black carbon in the climate system: A scientific assessment, *J. Geophys. Res. Atmospheres*, *118*(11), 5380-5552, doi:10.1002/jgrd.50171.

Boucher, O. et al. (2013), Clouds and Aerosols. In: *Climate Change 2013: The Physical Science Basis*. Contribution of Working Group I to the Fifth Assessment Report of the Intergovernmental Panel on Climate Change [Stocker, T.F., D. Qin, G.-K. Plattner, M. Tignor, S.K. Allen, J. Boschung, A. Nauels, Y. Xia, V. Bex and P.M. Midgley (eds.)]. Cambridge University Press, Cambridge, United Kingdom and New York, NY, USA.

Buchard, V., A. M. da Silva, P. R. Colarco, A. Darmenov, C. A. Randles, R. Govindaraju, O. Torres, J. Campbell, and R. Spurr (2015), Using the OMI aerosol index and absorption aerosol optical depth to evaluate the NASA MERRA Aerosol Reanalysis, *Atmos. Chem. Phys.*, *15*(10), 5743-5760, doi:10.5194/acp-15-5743-2015.

Burton, S. P., R. A. Ferrare, M. A. Vaughan, A. H. Omar, R. R. Rogers, C. A. Hostetler, and J. W. Hair (2013), Aerosol classification from airborne HSRL and comparisons with the CALIPSO vertical feature mask, *Atmos. Meas. Tech.*, *6*(5), 1397-1412, doi:10.5194/amt-6-1397-2013.

Chand, D., R. Wood, T. L. Anderson, S. K. Satheesh, and R. J. Charlson (2009), Satellite-derived direct radiative effect of aerosols dependent on cloud cover, *Nat. Geosci.*, *2*(3), 181-184, doi:10.1038/Ngeo437.

Charlson, R. J., S. E. Schwartz, J. M. Hales, R. D. Cess, J. A. Coakley, Jr., J. E. Hansen, and D. J. Hofmann (1992), Climate forcing by anthropogenic aerosols, *Science*, 255, 423–429.

Chen, W.-T., A. Nenes, H. Liao, P. J. Adams, J.-L. F. Li, and J. H. Seinfeld (2010), Global climate response to anthropogenic aerosol indirect effects: Present day and year 2100, *J. Geophys. Res.*, 115, D12207, doi:10.1029/2008JD011619.

Chin, M., P. Ginoux, S. Kinne, O. Torres, B. N. Holben, B. N. Duncan, R. V. Martin, J. A. Logan, A. Higurashi, and T. Nakajima (2002), Tropospheric aerosol optical thickness from the GOCART model and comparisons with satellite and Sun photometer measurements, *J. Atmos. Sci.*, *59*(3), 461-483, doi:Doi 10.1175/1520-0469(2002)059<0461:Taotft>2.0.Co;2.

Chin, M., A. Chu, R. Levy, L. Remer, Y. Kaufman, B. Holben, T. Eck, P. Ginoux, and Q. Gao (2004), Aerosol distribution in the Northern Hemisphere during ACE-Asia: Results from global model, satellite observations, and Sun photometer measurements, *J. Geophys. Res. Atmospheres*, *109*, D23S90, doi:10.1029/2004JD004829.

Chin, M., T. Diehl, O. Dubovik, T. F. Eck, B. N. Holben, A. Sinyuk, and D. G. Streets (2009), Light absorption by pollution, dust, and biomass burning aerosols: a global model study and evaluation with AERONET measurements, *Ann. Geophys.*, *27*(9), 3439-3464, doi:10.5194/angeo-27-3439-2009.

Chou, M.-D., and M. J. Suarez (2002), A solar radiation parameterization for atmospheric studies,NASA Tech. Memo, TM-104606, vol. 15, 40 pp. Chou, M.-D., M. J. Suarez, X.-A. Liang, and M. M.-H. Yan (2003), A thermal infrared radiation parameterization for atmospheric studies, NASA Tech. Memo, TM-104606, vol. 19, 85 pp.

Chýlek, P. and J. A. Coakley (1974), Aerosols and Climate, *Science*, 183, 75–77.

Colarco, P., A. da Silva, M. Chin, and T. Diehl (2010), Online simulations of global aerosol distributions in the NASA GEOS-4 model and comparisons to satellite and ground-based aerosol optical depth, *J. Geophys. Res. Atmospheres*, *115*, D14207, doi:10.1029/2009JD012820.

Colarco, P., E. P. Nowottnick, C. A. Randles, B. Yi, P. Yang, K.-M. Kim, J. A. Smith, and C. G. Bardeen (2014), Impact of radiatively interactive dust aerosols in the NASA GEOS-5 climate model: Sensitivity to dust particle shape and refractive index, *J. Geophys. Res. Atmospheres*, *119*(2), 753-786, doi:10.1002/2013JD020046.

Cooke, W. F., C. Liousse, H. Cachier, and J. Feichter (1999), Construction of a 1° × 1° fossil fuel emission data set for carbonaceous aerosol and implementation and radiative impact in the ECHAM4 model, *J. Geophys. Res. Atmospheres*, *104*(D18), 22137-22162, doi:10.1029/1999JD900187.

Costantino, L., and F. M. Bréon (2010), Analysis of aerosol-cloud interaction from multi-sensor satellite observations, *Geophys. Res. Lett.*, *37*, L11801, doi:10.1029/2009gl041828.

Costantino, L., and F. M. Bréon (2013), Aerosol indirect effect on warm clouds over South-East Atlantic, from co-located MODIS and CALIPSO observations, *Atmos. Chem. Phys.*, *13*(1), 69-88, doi:10.5194/acp-13-69-2013.

Curci, G., et al. (2014), Uncertainties of simulated aerosol optical properties induced by assumptions on aerosol physical and chemical properties: an AQMEII-2 perspective, *Atmos. Environ., 115*, 541-552, doi:10.1016/j.atmosenv.2014.09.009.

Darmenov, A., and A. da Silva (2015), The Quick Fire Emissions Dataset (QFED):Documentation of versions 2.1, 2.2 and 2.4, *NASA/TM–2015–104606, Vol. 38.*

Derbyshire, S. H., A. V. Maidens, S. F. Milton, R. A. Stratton, and M. R. Willett (2011), Adaptive detrainment in a convective parametrization, *Q. J. R. Meteorol. Soc.*, *137*(660), 1856-1871, doi:10.1002/qj.875.

Eck, T. F., et al. (2013), A seasonal trend of single scattering albedo in southern African biomass-burning particles: Implications for satellite products and estimates of emissions for the world's largest biomass-burning source, *J. Geophys. Res. Atmospheres*, *118*(12), 6414-6432, doi:10.1002/jgrd.50500.

Eck, T. F., B. N. Holben, J. S. Reid, O. Dubovik, A. Smirnov, N. T. O'Neill, I. Slutsker, and S. Kinne (1999), Wavelength dependence of the optical depth of biomass burning, urban, and desert dust aerosols, *J. Geophys. Res.*, 104 (D24), 31333–31349.

Edwards, D. P., et al. (2006), Satellite-observed pollution from Southern Hemisphere biomass burning, *J. Geophys. Res. Atmospheres*, *111*, D14312, doi:10.1029/2005JD006655.

Ford, B., and C. L. Heald (2012), An A-train and model perspective on the vertical distribution of aerosols and CO in the Northern Hemisphere, *J. Geophys. Res. Atmospheres*, *117*, D06211, doi:10.1029/2011JD016977.

Gregory, D., and P. R. Rowntree (1990), A mass flux convection scheme with representation of cloud ensemble characteristics and stability-dependent closure, *Mon. Weather Rev.*, *118*(7), 1483-1506, doi:10.1175/1520-0493(1990)118<1483:AMFCSW>2.0.CO;2.

Hansen, J., M. Sato, and R. Ruedy (1997), Radiative forcing and climate response, *J. Geophys. Res.,* 102, 6831–6864.

Hao, W. M., D. E. Ward, G. Olbu, and S. P. Baker (1996), Emissions of CO2, CO, and hydrocarbons from fires in diverse African savanna ecosystems, *J. Geophys. Res. Atmospheres*, *101*(D19), 23577-23584, doi:10.1029/95JD02198.

Haywood, J. M., S. R. Osborne, and S. J. Abel (2004), The effect of overlying absorbing aerosol layers on remote sensing retrievals of cloud effective radius and cloud optical depth, *Q. J. R. Meteorol. Soc.*, *130* (598), 779-800, doi:10.1256/qj.03.100.

Heintzenberg, J., Charlson, R. J., Clarke, A. D., Liousse, C., Ramanathan, V., Shine, K. P., Wendisch, M., and Helas, G. (1997), Measurements and modelling of aerosol single-scattering albedo: Progress, problems and prospects. *Beitr. Phy. Atmosph*, 70(4), 249–263.

Hess, M., P. Koepke, and I. Schult (1998), Optical Properties of Aerosols and Clouds: The Software Package OPAC, *B. Am. Meteorol. Soc.*, *79*(5), 831-844, doi:10.1175/1520-0477(1998)079<0831:OPOAAC>2.0.CO;2.

Hunt, W. H., D. M. Winker, M. A. Vaughan, K. A. Powell, P. L. Lucker, and C. Weimer (2009), CALIPSO lidar description and performance assessment, *J. Atmos. Oceanic Technol.*, *26*(7), 1214-1228, doi:10.1175/2009JTECHA1223.1.

Jethva, H., O. Torres, F. Waquet, D. Chand, and Y. Hu (2014), How do A-train sensors intercompare in the retrieval of above-cloud aerosol optical depth? A case study-based assessment, *Geophys. Res. Lett.*, *41*(1), 186-192, doi:10.1002/2013GL058405.

Johnson, B. T., K. P. Shine, and P. M. Forster (2004), The semi-direct aerosol effect: Impact of absorbing aerosols on marine stratocumulus, *Q. J. R. Meteorol. Soc.*, *130*(599), 1407-1422, doi:10.1256/qj.03.61.

Johnson, B. T., J. M. Haywood, J. M.Langridge, E. Darbyshire, W. T. Morgan, K.,Szpek, J. Brooke, F. Marenco, H. Coe, P. Artaxo, K. M. Longo, J. Mulcahy, G. Mann, M. Dalvi, and N. Bellouin (2016), Evaluation of biomass burning aerosols in the HadGEM3 climate model with observations from the SAMBBA field campaign, *Atmos. Chem. Phys. Discuss.*, doi:10.5194/acp-2016-442, in review.

Kacenelenbogen, M., J. Redemann, M. A. Vaughan, A. H. Omar, P. B. Russell, S. Burton, R. R. Rogers, R. A. Ferrare, and C. A. Hostetler (2014), An evaluation of CALIOP/CALIPSO's aerosol-above-cloud detection and retrieval capability over North America, *J. Geophys. Res. Atmospheres*, *119*(1), 230-244, doi:10.1002/2013JD020178.

Kaufman, Y. J., J. M. Haywood, P. V. Hobbs, W. Hart, R. Kleidman, and B. Schmid (2003), Remote sensing of vertical distributions of smoke aerosol off the coast of Africa, *Geophys. Res. Lett.*, *30*, 1831, doi:10.1029/2003GL017068.

Keil, A., and J. M. Haywood (2003), Solar radiative forcing by biomass burning aerosol particles during SAFARI 2000: A case study based on measured aerosol and cloud properties, *J. Geophys. Res. Atmospheres*, *108*, 8467, doi:10.1029/2002JD002315.

Kinne, S., et al. (2006), An AeroCom initial assessment – optical properties in aerosol component modules of global models, *Atmos. Chem. Phys.*, *6*(7), 1815-1834, doi:10.5194/acp-6-1815-2006.

Koch, D., and A. D. Del Genio (2010), Black carbon semi-direct effects on cloud cover: review and synthesis, *Atmos. Chem. Phys.*, *10*(16), 7685-7696, doi:10.5194/acp-10-7685-2010.

Koffi, B., et al. (2012), Application of the CALIOP layer product to evaluate the vertical distribution of aerosols estimated by global models: AeroCom phase I results, *J. Geophys. Res. Atmospheres*, *117*, D10201, doi:10.1029/2011JD016858.

Koffi, B., et al. (2016), Evaluation of the aerosol vertical distribution in global aerosol models through comparison against CALIOP measurements: AeroCom phase II results. *J. Geophys. Res. Atmos., 121*(12), 7254-7283, doi:10.1002/2015JD024639.

Koster, R. D., Suarez, M. J., Ducharne, A., Stieglitz, M., and Kumar, P, (2000), A catchment-based approach to modeling land surface processes in a GCM, Part 1, Model structure, *J. Geophys. Res.,* 105, 24809–24822.

Levy, R. C., L.A. Remer, R.G. Kleidman, S. Mattoo, C. Ichoku, R. Kahn, and T.F. Eck (2010), Global evaluation of the Collection 5 MODIS dark-target aerosol products over land, *Atmos. Chem. Phys.*, 10, 10399-10420, doi:10.5194/acp-10-10399-2010.

Li, Z., K.-H. Lee, Y. Wang, J. Xin, and W.-M. Hao, (2010), First observation-based estimates of cloud-free aerosol radiative forcing across China. *J. Geophys. Res.*, 115, D00K18.

Lilly, D. K., (1968), Models of cloud-topped mixed layers under a strong inversion. *Q. J. R. Meteorol. Soc,* 94, 292–309.

Liu, X., et al. (2012), Toward a minimal representation of aerosols in climate models: description and evaluation in the Community Atmosphere Model CAM5, *Geosci. Model Dev.*, *5*(3), 709-739, doi:10.5194/gmd-5-709-2012.

Liu, Z. Y., M. Vaughan, D. Winker, C. Kittaka, B. Getzewich, R. Kuehn, A. Omar, K. Powell, C. Trepte, and C. Hostetler (2009), The CALIPSO lidar cloud and aerosol discrimination: Version 2 algorithm and initial assessment of performance, *J. Atmos. Oceanic Technol.*, *26*(7), 1198-1213, doi:10.1175/2009jtecha1229.1.

Liu, Z. Y., D. Winker, A. Omar, M. Vaughan, J. Kar, C. Trepte, Y. Hu, and G. Schuster (2015), Evaluation of CALIOP 532 nm aerosol optical depth over opaque water clouds, *Atmos. Chem. Phys.*, *15*(3), 1265-1288, doi:10.5194/acp-15-1265-2015.

Lin, S.-J. (2004), A vertically Lagrangian finite-volume dynamical core for global models, *Mon. Weather Rev.*, 132 (10), 2293–2307.

Lock, A. P., A. R. Brown, M. R. Bush, G. M. Martin, and R. N. B. Smith, (2000), A new boundary layer mixing scheme. Part I: Scheme description and single-column model tests, *Mon. Weather Rev.,* 128, 3187–3199.

Louis, J. F. and Geleyn, J, (1982), A short history of the PBL parameterization at ECMWF. Proc. ECMWF Workshop on Planetary Boundary Layer Parameterization, Reading, United Kingdom, ECMWF, 59–80.

Maria, S. F., L. M. Russell, M. K. Gilles, and S. C. B. Myneni (2004), Organic aerosol growth mechanisms and their climate-forcing implications, *Science*, *306*(5703), 1921-1924, doi:10.1126/science.1103491.

McFarquhar, G. M., and H. Wang (2006), Effects of aerosols on trade wind cumuli over the Indian Ocean: Model simulations, *Q. J. R. Meteorol. Soc.*, *132*(616), 821-843, doi:10.1256/qj.04.179.

Mechoso, C. R., et al. (2013), Ocean–cloud–atmosphere–land interactions in the Southeastern Pacific: The VOCALS program, *B. Am. Meteorol. Soc.*, *95*(3), 357-375, doi:10.1175/BAMS-D-11-00246.1.

Meyer, K., S. Platnick, L. Oreopoulos, and D. Lee (2013), Estimating the direct radiative effect of absorbing aerosols overlying marine boundary layer clouds in the southeast Atlantic using MODIS and CALIOP, *J. Geophys. Res. Atmos.*, 118, 4801–4815, doi:10.1002/jgrd.50449.

Mielonen, T., A. Arola, M. Komppula, J. Kukkonen, J. Koskinen, G. de Leeuw, and K. E. J. Lehtinen (2009), Comparison of CALIOP level 2 aerosol subtypes to aerosol types derived from AERONET inversion data, *Geophys. Res. Lett.*, 36, L18804, doi:10.1029/2009GL039609.

Molod, A.: Constraints on the Profiles of Total Water PDF in AGCMs from AIRS and a High-Resolution Model, *J. Climate*, 25, 8341–8352, 2012.

Molod, A., Takacs, L. L., Suarez, M. J., Bacmeister, J. T., Song, I.- S., and Eichmann, A.: The GEOS-5 Atmospheric General Circulation Model: Mean Climate and Development from MERRA to Fortuna. NASA Tech. Memo. 104606, Vol. 28, Tech. Rep. Series on Global Modeling and Data Assimilation, edited by: Suarez, M. J., 117 pp., 2012.

Molod, A., Takacs, L., Suarez, M., and Bacmeister, J, (2015), Development of the GEOS-5 atmospheric general circulation model: evolution from MERRA to MERRA2, *Geosci. Model Dev.,* 8, 1339-1356,

Moorthi, S., and M. J. Suarez (1992), Relaxed Arakawa-Schubert. A parameterization of moist convection for general circulation models, *Mon. Weather Rev.*, *120*(6), 978-1002, doi:10.1175/1520-0493(1992)120<0978:RASAPO>2.0.CO;2.

Myhre, G., et al. (2013), Anthropogenic and Natural Radiative Forcing. In: Climate Change 2013: The Physical Science Basis. Contribution of Working Group I to the Fifth Assessment Report of the Intergovernmental Panel on Climate Change [Stocker, T.F., D. Qin, G.-K. Plattner, M. Tignor, S.K. Allen, J. Boschung, A. Nauels, Y. Xia, V. Bex and P.M. Midgley (eds.)]. Cambridge University Press, Cambridge, United Kingdom and New York, NY, USA.

Myhre, G., et al. (2013), Radiative forcing of the direct aerosol effect from AeroCom Phase II simulations, *Atmos. Chem. Phys.*, *13*(4), 1853-1877, doi:10.5194/acp-13-1853-2013.

Nicholls, S., (1984), The dynamics of stratocumulus: Aircraft observations and comparisons with a mixed layer model. *Q. J. R. Meteorol. Soc.*, 110, 783–820.

Nordeng, T. E. (1994), Extended versions of the convective parametrization scheme at ECMWF and their impact on the mean and transient activity of the model in the tropics, *Tech. Memo., 206*, ECMWF.

Omar, A. H., et al. (2009), The CALIPSO automated aerosol classification and lidar ratio selection algorithm, *J. Atmos. Oceanic Technol.*, *26*(10), 1994-2014, doi:10.1175/2009JTECHA1231.1.

Painemal, D., S. Kato, and P. Minnis (2014), Boundary layer regulation in the southeast Atlantic cloud microphysics during the biomass burning season as seen by the A-train satellite constellation, *J. Geophys. Res. Atmospheres*, *119* (19), 11, 288-211, 302, doi:10.1002/2014JD022182.

Park, S., and C. S. Bretherton (2009), The University of Washington shallow convection and moist turbulence schemes and their impact on climate simulations with the Community Atmosphere Model, *J. Clim.*, *22*(12), 3449-3469, doi:10.1175/2008JCLI2557.1.

Penner, J. E., S. Y. Zhang, and C. C. Chuang (2003), Soot and smoke aerosol may not warm climate, *J. Geophys. Res. Atmospheres*, *108*, 4657, doi:10.1029/2003JD003409.

Protonotariou, A. P., M. Tombrou, C. Giannakopoulos, E. Kostopoulou, and P. Le Sager (2010), Study of CO surface pollution in Europe based on observations and nested-grid applications of GEOS-CHEM global chemical transport model, *Tellus B*, *62*:209–227. doi:10.1111/j.1600-0889.2010.00462.x.

Rajapakshe, C., Z. Zhang, J. E. Yorks, H. Yu, Q. Tan, K. Meyer, S. Platnick, and D. M. Winker (2017), Seasonally transported aerosol layers over southeast Atlantic are closer to underlying clouds than previously reported, *Geophys. Res. Lett.*, 44, 5818–5825,

Ramanathan, V., P. J. Crutzen, J. T. Kiehl, and D. Rosenfeld (2001), Aerosols, climate, and the hydrological cycle, *Science*, *294*(5549), 2119-2124, doi:10.1126/science.1064034.

Ramaswamy, V., et al., (2001), Radiative forcing of climate change. In: Climate Change 2001: The Scientific Basis. Contribution of Working Group I to the Third Assessment Report of the Intergovernmntal Panel on Climate Change [J. T. Houghton, Y. Ding, D. J. Griggs, M. Noquer, P. J. van der Linden, X. Dai, K. Maskell and C. A. Johnson (eds.)]. Cambride University Press, Cambridge, United Kingdom and New York, NY, USA, 349-416.

Randall, D. A., (1984), Stratocumulus cloud deepening through entrainment. *Tellus,* 36A, 446–457.

Randerson, J. T., G. R. van der Werf, L. Giglio, G. J. Collatz, and P. Kasibhatla (2013), Global Fire Emissions Database, Version 3 (GFEDv3.1). Available on-line from *Oak Ridge National Laboratory Distributed Active Archive Center,* Oak Ridge, Tenessee, USA, doi:10.3334/ORNLDAAC/1191.

Randles, C. A., P. R. Colarco, and A. da Silva (2013), Direct and semi-direct aerosol effects in the NASA GEOS-5 AGCM: aerosol-climate interactions due to prognostic versus prescribed aerosols, *J. Geophys. Res. Atmospheres*, *118*(1), 149-169, doi:10.1029/2012JD018388.

Randles, C. A., and V. Ramaswamy (2010), Direct and semi-direct impacts of absorbing biomass burning aerosol on the climate of southern Africa: a Geophysical Fluid Dynamics Laboratory GCM sensitivity study, *Atmos. Chem. Phys.*, *10*(20), 9819-9831, doi:10.5194/acp-10-9819-2010.

Reddy, M. S., O. Boucher, Y. Balkanski, and M. Schulz (2005), Aerosol optical depths and direct radiative perturbations by species and source type. *Geophys. Res. Lett.,* 32, L12803.

Rienecker, M. M., et al. (2011), MERRA: NASA's Modern-Era Retrospective Analysis for Research and Applications, *J. Clim.*, *24*(14), 3624-3648, doi:10.1175/Jcli-D-11-00015.1.

Rienecker, M. M., et al. (2008), The GEOS-5 data assimilation system—Documentation of version 5.0.1, 5.1.0, and 5.2.0, *NASA TM/2008-104606, Vol. 27*, 118 pp.

Roeckner, E., R. Brokopf, M. Esch, M. Giorgetta, S. Hagemann, L. Kornblueh, E. Manzini, U. Schlese, and U. Schulzweida (2006), Sensitivity of simulated climate to horizontal and vertical resolution in the ECHAM5 atmosphere model, *J. Clim.*, *19*(16), 3771-3791, doi:10.1175/JCLI3824.1.

Sakaeda, N., R. Wood, and P. J. Rasch (2011), Direct and semidirect aerosol effects of southern African biomass burning aerosol, *J. Geophys. Res. Atmospheres*, *116*, D12205, doi:10.1029/2010JD015540.

Saleh, R. et al. (2014), Brownness of organics in aerosols from biomass burning linked to their black carbon content. *Nature Geosci.* 7,647–650.

Samset, B. H., et al. (2013), Black carbon vertical profiles strongly affect its radiative forcing uncertainty, *Atmos. Chem. Phys.*, *13*(5), 2423-2434, doi:10.5194/acp-13-2423-2013.

Schulz, M., et al. (2006), Radiative forcing by aerosols as derived from the AeroCom present-day and pre-industrial simulations, *Atmos. Chem. Phys.*, *6*(12), 5225-5246, doi:10.5194/acp-6-5225-2006.

Smith, R. N. B. (1990), A scheme for predicting layer clouds and their water content in general circulation models. *QJRMS,* 116, 435–460.

Stephens, G. L., (1978a), Radiation profiles in extended water clouds: 1. Theory. *J. Atmos. Sci.*, 35, 2111–2122.

Stevens, B., et al. (2013), Atmospheric component of the MPI-M Earth System Model: ECHAM6, *J. Adv. Model Earth Sy.*, *5*(2), 146-172, doi:10.1002/jame.20015.

Stier, P., et al. (2013), Host model uncertainties in aerosol radiative forcing estimates: results from the AeroCom Prescribed intercomparison study, *Atmos. Chem. Phys.*, *13*(6), 3245-3270, doi:10.5194/acp-13-3245-2013.

Streets, D. G., F. Yan, M. Chin, T. Diehl, N. Mahowald, M. Schultz, M. Wild, Y. Wu, and C. Yu (2009), Anthropogenic and natural contributions to regional trends in aerosol optical depth, 1980–2006, *J. Geophys. Res.*, 114, D00D18, doi:10.1029/2008JD011624.

Textor, C., et al. (2006), Analysis and quantification of the diversities of aerosol life cycles within AeroCom, *Atmos. Chem. Phys.*, *6*(7), 1777-1813, doi:10.5194/acp-6-1777-2006.

Tiedtke, M. (1989), A comprehensive mass flux scheme for cumulus parameterization in large-scale models, *Mon. Weather Rev.*, *117*(8), 1779-1800, doi:10.1175/1520-0493(1989)117<1779:ACMFSF>2.0.CO;2.

Torres, O., C. Ahn, and Z. Chen (2013), Improvements to the OMI near-UV aerosol algorithm using A-train CALIOP and AIRS observations, *Atmos. Meas. Tech.*, 6, 3257-3270, doi:10.5194/amt-6-3257-2013.

van der Werf, G. R., J. T. Randerson, L. Giglio, G. J. Collatz, P. S. Kasibhatla, and A. F. Arellano Jr (2006), Interannual variability in global biomass burning emissions from 1997 to 2004, *Atmos. Chem. Phys.*, *6*(11), 3423-3441, doi:10.5194/acp-6-3423-2006.

van der Werf, G. R., J. T. Randerson, L. Giglio, G. J. Collatz, M. Mu, P. S. Kasibhatla, D. C. Morton, R. S. DeFries, Y. Jin, and T. T. van Leeuwen (2010), Global fire emissions and the contribution of deforestation, savanna, forest, agricultural, and peat fires (1997–2009), *Atmos. Chem. Phys.*, *10*(23), 11707-11735, doi:10.5194/acp-10-11707-2010.

Vaughan, M. A., et al. (2009), Fully automated detection of cloud and aerosol layers in the CALIPSO lidar measurements, *J. Atmos. Oceanic Technol.*, *26*(10), 2034-2050, doi:10.1175/2009JTECHA1228.1.

Warren, S. G., C. J. Hahn, J. London, R. M. Chervin, and R. L. Jenne, (1988), Global distribution 238 of total cloud cover and cloud types over ocean. NCAR Tech. Note NCAR/TN-3171STR, 239 National Center for Atmospheric Research, Boulder, CO, 42 pp. 1 170 maps.

Washington, R., M. Todd, N. J. Middleton, and A. S. Goudie (2003), Dust-storm source areas determined by the Total Ozone Monitoring Spectrometer and surface observations, *Ann. Assoc. Am. Geogr.*, *93*(2), 297-313, doi:10.1111/1467-8306.9302003.

Wilcox, E. M. (2010), Stratocumulus cloud thickening beneath layers of absorbing smoke aerosol, *Atmos. Chem. Phys.*, *10*(23), 11769-11777, doi:10.5194/acp-10-11769-2010.

Wilcox, E. M. (2012), Direct and semi-direct radiative forcing of smoke aerosols over clouds, *Atmos. Chem. Phys.*, *12*(1), 139-149, doi:10.5194/acp-12-139-2012.

Wilks, D. S., Statististical Methods in the Atmospheric Sciences, Elsevier Academic Press, Boston, MA, USA, 627 pp.

Winker, D. M., J. L. Tackett, B. J. Getzewich, Z. Liu, M. A. Vaughan, and R. R. Rogers (2013), The global 3-D distribution of tropospheric aerosols as characterized by CALIOP, *Atmos. Chem. Phys.*, *13*(6), 3345-3361, doi:10.5194/acp-13-3345-2013.

Winker, D. M., M. A. Vaughan, A. Omar, Y. X. Hu, K. A. Powell, Z. Y. Liu, W. H. Hunt, and S. A. Young (2009), Overview of the CALIPSO mission and CALIOP data processing algorithms, *J. Atmos. Oceanic Technol.*, *26*(11), 2310-2323, doi:10.1175/2009jtecha1281.1.

Wood, R., 2005a: Drizzle in stratiform boundary layer clouds. Part I: Vertical and horizontal structure. *J. Atmos. Sci.,* 62, 3011–3033.

Wood, R. and D. L. Hartmann, (2006) Spatial variability of liquid water path in marine boundary layer clouds: The importance of mesoscale cellular convection. *J. Climate,* 19, 1748–1764.

Wood, R., (2012), Stratocumulus Clouds. *Mon. Wea. Rev.,* 140, 2373–2423.

Xiao, H., CM. Wu, and C. R. Mechoso, *Clim Dyn* (2011) 37: 971.

Yamaguchi, T., G. Feingold, J. Kazil, and A. McComiskey (2015), Stratocumulus to cumulus transition in the presence of elevated smoke layers, *Geophys. Res. Lett.*, 42, 10,478–10,485, doi:10.1002/2015GL066544.

Young, S. A., and M. A. Vaughan (2009), The Retrieval of profiles of particulate extinction from Cloud-Aerosol Lidar Infrared Pathfinder Satellite Observations (CALIPSO) Data: Algorithm description, *J. Atmos. Oceanic Technol.*, *26*(6), 1105-1119,

Yu, H., M. Chin, D. M. Winker, A. H. Omar, Z. Liu, C. Kittaka, and T. Diehl (2010), Global view of aerosol vertical distributions from CALIPSO lidar measurements and GOCART simulations: Regional and seasonal variations, *J. Geophys. Res. Atmospheres*, *115*, D00H30, doi:10.1029/2009JD013364.

Yu, H., et al., (2006), A review of measurement-based assessments of the aerosol direct radiative effect and forcing. *Atmos. Chem. Phys.,* 6, 613–666.

Zhang, G. J., and N. A. McFarlane (1995), Sensitivity of climate simulations to the parameterization of cumulus convection in the Canadian climate centre general circulation model, *Atmosphere-Ocean*, *33*(3), 407-446, doi:10.1080/07055900.1995.9649539.

Zhang, Z., et al. (2016), Shortwave direct radiative effects of above-cloud aerosols over global oceans derived from 8 years of CALIOP and MODIS observations, *Atmos. Chem. Phys.*, 16, 2877-2900, doi:10.5194/acp-16-2877-2016.

Zhou, X., A. S. Ackerman, A. M. Fridlind, R. Wood, and P. Kollias (2017), Impacts of solar-absorbing aerosol layers on the transition of stratocumulus to trade cumulus clouds, *Atmos. Chem. Phys.,* 17, 12725-12742, https://doi.org/10.5194/acp-17-12725-2017.

Zhu, P., et al., (2005), Inter-comparison and interpretation of single-column model simulations of a nocturnal stratocumulus topped marine boundary layer. *Mon. Wea. Rev.,* 133, 2741–2758.

Zuidema, P., J. Redemann, J. Haywood, R. Wood, S. Piketh, M. Hipondoka, and P. Formenti, (2016), Smoke and Clouds above the Southeast Atlantic: Upcoming Field Campaigns Probe Absorbing Aerosol's Impact on Climate. *Bull. Amer. Meteor. Soc.,* 97, 1131–1135.